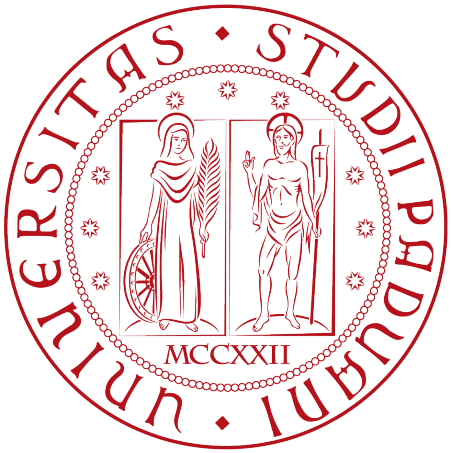

UNIVERSITÀ DEGLI STUDI DI PADOVA
Dipartimento di Scienze Chimiche - DISC
Dipartimento di Fisica e Astronomia "G. Galilei" - DFA

Corso di dottorato in Scienza e Ingegneria dei Materiali e delle Nanostrutture
XXXI CICLO

TESI DI DOTTORATO

LOCAL FLUIDIZATION OF CONCENTRATED EMULSION IN MICROFLUIDIC CHANNELS TEXTURED AT THE DROPLET SCALE

Coordinatore: Ch.mo Prof. Giovanni Mattei
Supervisore: Ch.mo Prof. Matteo Pierno
Co-Supervisore: Ch.mo Prof. Giampaolo Mistura
Co-supervisore: Dott. Ladislav Derzsi

Dottorando: Daniele Filippi

Alla mia famiglia

"Chi più alto sale, più lontano vede;
chi più lontano vede, più a lungo sogna."

Walter Bonatti

Alberto Graia - *Torri del Vajolet*

Riassunto

La reologia dei sistemi soffici, quali emulsioni concentrate, schiume, gel, fanghi, vetri colloidali ha un grande impatto in ambito scientifico e ingegneristico. Gran parte del fascino di questi sistemi deriva dal fatto che essi non si collocano in nessuno dei tre stati base della materia, gas-liquido-solido, ma si posizionano ai limiti di ciascuna di esse. Per comprendere il meccanismo con il quale questi materiali scorrono è necessario osservare la dinamica dei loro costituenti (gocce per le emulsioni, bolle per le schiume, etc.) su scala microscopica. Infatti, il flusso è caratterizzato da una successione di deformazioni elastiche e riarrangiamenti plastici. Questi, creano delle regioni a maggior "fluidità" in cui il materiale scorre. Il processo di fluidizzazione degli *Soft Glassy Materials* (SGMs) è fortemente influenzato dalla presenza di rugosità sulla superficie con cui sono a contatto, tuttavia il ruolo giocato dalla periodicità, l'orientazione e la forma degli elementi che costituiscono questa rugosità non è ancora stato del tutto compreso. Infatti, prevedere e controllare il flusso di questi SGMs è fondamentale in numerose applicazioni tecnologiche che vanno dall'industria alimentare a quella farmaceutica.

In questo lavoro di tesi abbiamo studiato il flusso di emulsioni concentrate in canali microfluidici. Questi ultimi presentavano una rugosità controllata, su scala micrometrica, posizionata sul fondo del canale. Utilizzando come micro-rugosità una sequenza di "grooves" (solchi) posti ortogonalmente al flusso, abbiamo osservato che la fluidizzazione indotta dipende dalla densità e dalla periodicità dei solchi. Ne consegue che, la fluidizzazione può essere controllata e regolata in modo quantitativo agendo sulla spaziatura di questi solchi. Inoltre, abbiamo osservato l'esistenza di due scenari con meccaniche di riarrangiamento differenti. Quando la spaziatura dei solchi è grande, rispetto alla dimensione delle gocce, queste colpiscono gli ostacoli e facilmente riarrangiano andando ad interagire con altre gocce vicine. Al contrario, riducendo lo spazio tra i solchi, le gocce ve ne rimangono intrappolate creando uno strato di "rugosità soffice" creando a loro volta una nuova serie di ostacoli deformabili. Con l'introduzione di rugosità dalla geometria asimmetrica (a spina di pesce) abbiamo osservato che, anche il flusso all'interno del canale presenta un comportamento non simmetrico. L'emulsione, infatti, scorre più velocemente nello stesso verso della spina di pesce, rispetto a quando scorre nel verso opposto.
Le nostre osservazioni sperimentali sono e supportate e confermate da simulazioni lattice Boltzmann. Queste simulazioni, cruciali per evidenziare le variazioni nella distribuzione spaziale dei riarrangiamenti plastici, sono un potente mezzo per studiare e comprendere le micro-dinamiche che portano alla fluidizzazione del materiale.

Parole chiave: microfluidica, microfabbricazione, fluidi complessi, emulsioni concentrate, riarrangiamenti plastici, fluidificazione.

Abstract

The rheology of soft-flowing systems, such as concentrated emulsions, foams, gels, slurries, colloidal glasses and related complex fluids, has a larger and larger impact in modern science and engineering. Much of the fascination of these systems stems from the fact that they do not fall within any of three basic states of matter, gas-liquid-solid, but live rather on a moving border between them. To understand the flow mechanism, it is necessary to have a look at the microscale dynamics of its constituents (i.e, droplets for emulsions, bubbles for foams, blobs for gels, etc.). In fact, in these fluids the flow occurs via successive elastic deformations and plastic rearrangements, which create fragile regions enhancing the "fluidization" of the material. Despite the fluidization of Soft Glassy Materials (SGMs) is strongly affected by the surface roughness, the role played by the density, the orientation and the periodicity of rough elements has not been quantitatively addressed so far. In fact, predict and control the flow of SGMs is particularly important for an ample variety of technological applications from food to pharmaceutical industries.

In this work, we study the flow of concentrated emulsions in microfluidic channels, one wall of which is patterned with micron-size grooves with different patterns. Using equally spaced grooves, we find a scaling law describing the roughness-induced fluidization as a function of the density of the grooves, thus fluidization can be predicted and quantitatively regulated. Furthermore we quantitatively report the existence of two physically different scenarios. When the gap is large, compared to the droplets in the emulsion, the droplets hit the solid obstacles and easily escape scrambling with their neighbors. Conversely, as the gap spacing is reduced, droplets get trapped inside, creating a "soft roughness" layer, i.e., a complementary series of deformable posts. Introducing an asymmetrical micro-roughness (herringbone pattern), the flow presents, in turn an asymmetric behavior. The emulsion flows faster in the same direction of the herringbone groove respect when it flows in the opposite direction.
Our experimental observations are suitably complemented and confirmed by lattice Boltzmann simulations. These numerical simulations are key to highlight the change in the spatial distribution of the plastic rearrangements caused by surface roughness and to elucidate the micromechanics of the roughness induced fluidization.

Keywords: microfluidics, microfabrication, complex fluids, soft-glassy materials, yield stress fluids, concentrated emulsion, plastic rearrangements, fluidization.

Contents

Riassunto **i**

Abstract **iii**

Introduction **1**

1 Complex fluids rheology **5**
1.1 Newtonian liquids 6
1.2 Non-Newtonian fluids 8
1.3 Time-independent fluids 11
1.3.1 Shear thinning models 11
1.3.2 Shear thickening models 13
1.3.3 Viscoplastic models 14
1.4 Origins of Non-Newtonian Behavior 16

2 Physics of fluids at the microscale **19**
2.1 Introduction 20
2.2 Hydrodynamics of the microfluidic system 20
2.2.1 Reynolds number 21
2.3 Parallel plates flow 22
2.3.1 Newtonian fluid flow 23
2.3.2 non-Newtonian fluid flow 24
2.4 Slip velocity 25
2.4.1 Slip Factors 26
2.4.2 Wall slip in complex fluids 27
2.5 Wetting 28
2.5.1 Surface tension 28
2.5.2 Wetting and Contact angle 29
2.5.3 Wetting on rough surfaces 30

3 Soft Glassy Materials **33**
3.1 Introduction 34
3.2 Dense Emulsion 34
3.2.1 Emulsion stability 35
3.2.2 Emulsion preparation 37
3.3 Soft Glassy Rheology 38

3.3.1 Shear banding . . . 40
3.3.2 Dense emulsion flow . . . 41
3.4 Models of Soft Glassy Rheology . . . 43
3.4.1 The Soft Glassy Rheology Model . . . 44
3.4.2 KEP model . . . 45

4 Microfabrication **47**
4.1 Microfabrication techniques . . . 49
4.1.1 Soft-lithography . . . 49
4.1.2 Micro-milling . . . 50
4.1.3 Additive Manufacturing . . . 51
4.2 Photolithography . . . 51
4.3 Multilayer photolithography . . . 55
4.4 Liquid photoresist: SU-8 . . . 56
4.5 Dry Film Photoresist . . . 57
4.6 Cleanroom . . . 58

5 Flow Visualization **59**
5.1 Flow visualization techniques . . . 61
5.2 Tracers Methods . . . 64
5.2.1 Particle Image Velocimetry and Particle Tracking Velocimetry . . . 64
5.2.2 Tracer Particles . . . 65
5.2.3 μ-PTV System Components . . . 66
5.2.4 Depth of field . . . 67
5.3 Particle tracking theory . . . 68

6 Materials and methods **71**
6.1 Dense Emulsion . . . 73
6.1.1 Emulsion preparation . . . 73
6.1.2 Concentrated Emulsion Characterization . . . 74
6.2 Microfluidic channel . . . 76
6.2.1 Fabrication details . . . 76
6.2.2 Roughness topologies . . . 79
6.2.3 Channel Characterization . . . 80
6.2.4 Surface modification . . . 80
6.3 Micro-PTV experimental setup . . . 82
6.3.1 Experimental procedure for data acquisition . . . 83
6.4 Image Analysis - Particle Tracking Velocimetry . . . 84

7 Results **87**
7.1 Smooth Channel . . . 88
7.1.1 Newtonian fluid's flow profiles . . . 88

7.1.2 Dense Emulsion's flow profiles . . . 89
7.2 Smooth-Rough channel . . . 91
7.2.1 Numerical model . . . 91
7.2.2 Dependence on periodicity . . . 93
7.3 Gaps effect: from stiff to soft roughness . . . 100
7.3.1 Dependence of volume fraction . . . 102
7.3.2 Displacement analysis . . . 104
7.4 Herringbone pattern . . . 106
7.4.1 Forward vs. Backward . . . 107
7.4.2 Effect of the grooves' periodicity . . . 110
7.4.3 Effect of the pressure drop . . . 111
7.4.4 Effect of the angle . . . 112

Conclusions **115**

A Tracking program: python code **119**

Bibliography **123**

List of Figures

1 Picture of oil-in-water emulsion 1

1.1 Schematic representation of an unidirectional shearing flow 7
1.2 Rheological curves for Newtonian fluids 7
1.3 Mechanical model for viscoelastic materials 9
1.4 Weissember effect 10
1.5 Rheological curves of time dependent fluids 10
1.6 Rheological curves for generalized Newtonian fluids 11
1.7 Experimental data for shear thinning fluids 12
1.8 Schematic representation of macromolecules under the influence of shear 12
1.9 Rheological curvers for TiO_2 suspension 14
1.10 Rheological curves for viscoplastic and Bingham plastic fluids. 15
1.11 Scheme of structures in non-Newtonian dispersion at rest and under shear 17

2.1 Continuum assumption in fluids 20
2.2 Transition from laminar to turbulent flow 22
2.3 Schematic representation of infinite plates geometry. 22
2.4 Velocity and shear stress distribution of a Newtonian fluid in parallel plates geometry 24
2.5 Velocity and shear stress distribution of a non-Newtonian fluid in parallel plates geometry 25
2.6 Schematic representations of different wall slip conditions 26
2.7 Schematic representations of true slip and apparent slip 28
2.8 The origin of surface tension for a liquid/gas interface 29
2.9 Young's contact angle 30
2.10 Wenzel and Cassie-Baxter models 31

3.1 Phase diagram of jammed state 34
3.2 Representation of direct and inverse emulsion 35
3.3 Schematic representation of various breakdown processes in emulsion 36
3.4 Morphology of monodispersed emulsion as a function of the volume fraction . . . 38
3.5 Emulsion hexagonal model 39
3.6 Rheology curves (τ, δ, G' and G") of concentrated emulsion 40
3.7 Schematic representation of solid-liquid discontinuous transition in shear banding flow 41
3.8 Flow curve of an emulsion at different volume fractions 42
3.10 Velocity profile for various roughness sizes 44

3.11 Schematic representation of plastic event is KEP model 45

4.1 Soft lithographic techniques 50
4.2 Photolithograpy steps 52
4.3 Positive and negative tone photoresist 54
4.4 Multilayer photolithography 55
4.5 Multilayer photolithography alignment sequence 56
4.6 Liquid photoresist: SU8 57
4.7 Dry photoresist lamination 58

5.1 Reynolds's handmade flow representation 61
5.2 Shadowgraph flow visualization 62
5.3 Surface flow visualization 63
5.4 Tracers flow visualization 64
5.5 PIV and PTV 65
5.6 Fluorescence emission 66
5.7 Tipical micro-PTV experimental system 67
5.8 Linear motion tracker 69

6.1 Homemade spatula mixer 73
6.2 Refractive index of the glycerol-water mixture 74
6.3 Size distribution analysis 75
6.4 Schematic draw of the cone-plate rheometer 75
6.5 Bulk rheological curve for dense emulsion 76
6.6 Channels fabrication steps 78
6.7 Characteristic dimensions of patterned grooves 79
6.8 Profilometer scan and extracted profile 80
6.9 Apparatus for the measurements of the contact angle 82
6.10 Schematic draw of the experimental set-up. 83
6.11 Excitation and emission spectra of fluorescent tracers 84
6.12 Flowchart of image analysis 84

7.1 Microfluidic channel with both smooth surfaces. 88
7.2 Experimental flow profiles and rheological curves for glycerol 89
7.3 Experimental velocity profiles for dense emulsion in smooth-smooth channel . . . 90
7.4 Scheme of th experimental set-up 92
7.5 Sketch of Delaunay triangulation 93
7.6 Experimental flow profile for a smooth-rough channel 94
7.7 Numerical flow profile and rate of plastic rearrangements 95
7.8 Spatial distribution of plastic rearrangements 96
7.9 Stress profile for smooth-smooth and smooth-rough channel 96
7.10 Velocity and fluidity profiles for a Couette geometry 97
7.11 Difference of the slip velocities as a function of the roughness periodicity 98

7.12 Lattice Boltzmann simulation results for the scaling law 99
7.13 Scaling law for two scenarios 100
7.14 "Get-in-get-out" and "trapping" scenario 101
7.15 Numerical fluidity field 102
7.16 Scaling law for the two scenarios: "wide gaps" and "narrow gaps" 103
7.17 Displacement field in proximity of a groove 105
7.18 Pictures of the microfluidic channel presenting herringbone pattern 106
7.19 Top view representation of V-grooves roughness 107
7.20 Velocity profiles $v_{flow}(z)$ measured in microfluidic channel with V-grooves pattern 108
7.21 V-grooves effect in central region of the channel 108
7.22 V-grooves effect in lateral region of the channel 109
7.23 Glycerol velocity profile $v_{flow}(z)$ flowing in herringbone patterned channel 110
7.24 Velocity profiles $v_{flow}(z)$ for different V-grooves roughness widths-gaps combinations 111
7.25 Velocity profiles $v_{flow}(z)$ for different pressure drop 112
7.26 Velocity profiles $v_{flow}(z)$ for different V-grooves roughness angle α 113

Introduction

How materials respond to external forces? Answer to this question may result a twisting conundrum. In fact, in everyday life we deal with a large number of materials that respond to an external stress in very different ways. Most solids initially deform elastically; that is to say, they return to their original shape when the external force is removed. Liquids constantly change their shapes and, when an external force is applied the flow. However, for some classes of materials it is a tricky task to discriminate between the two. A toothpaste flows like a liquid through the squeezed tube and spreads over the toothbrush where it will remain at rest while the brush is brought up to the mouth. Mayonnaise, that is prepared by strong mixing of two immiscible fluids, it can be dispersed over a food surface and it will remain at rest there. Toothpaste and mayonnaise are just two examples of substances thus present intermediate behavior between solid and liquid state; others examples include: emulsions, gels, creams, pastes, foams and muds.

To understand whether a (soft) material can flow as a viscous liquid or stay ad rest as an amorphous solid, it is necessary to have a look at the dynamics of its constituents (i.e, droplets for emulsions, bubbles for foams, blobs for gels, etc.). At the micro-scale these materials are in jammed state [1, 2]: meaning that the constitutive particles are caged by their neighbors. So that, at rest, their dynamics is so limited that the whole system can be considered "dynamic arrested" which is characteristic of many glasses materials, either soft or hard.

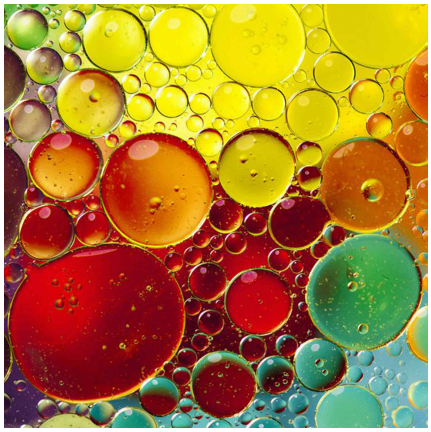

Figure 1: Picture of oil-in-water micro-emulsion.

Applying an external force it is possible to "move" these material outside this blocked state. At the microscale, the response of these materials to an external stress can be described by successive steps of elastic deformation and plastic rearrangements. During the elastic deformation, the particles remain trapped in a deformed cage. If the deformation is large enough, the particles will escape from the cage, and the stress due to the deformation will be relaxed. This relaxation is also called local rearrangement. When rearrangement occurs, other rearrangements will occur in the neighborhood; such cooperation between rearrangements produces a non-local behavior.

Materials that respond with this non-linear rheological behavior are called Yield stress fluids. They respond elastically to an external stress, unless a threshold value, called Yield stress, is reached. Above yield, the material starts to flow. The characteristic rheological relationship stress vs. shear rate, is given by the Herschel-Bulkley model [3–5]. This solid-to-liquid transition

and the corresponding flowing properties have been widely studied [6–10]. However, controlling their dynamics at different scales remains a great challenge for many industrial and technological applications.

This challenge can be tracked by studying the flow of soft glassy materials (SGMs) at the micro-scale focusing on the cooperativity and non-local effects. By studying the flow of a concentrated emulsion in a rectangular microchannel, Goyon *et al.* [11] show that the viscosity is not controlled by the bulk rheology but depends on the neighborhood. The fluidity, defined as the inverse of the dynamic viscosity of a given material, obeys a non-local law characterize by the presence of a characteristic cooperativity length, which is on the order of the droplets size. Theoretical models have been put forward to account for these non-local effects [12–15]. One of them, the kinetic elastoplastic (KEP) relates the fluidity field to the rate of plastic rearrangements showing that a higher rate is associated with a more fluid system.
Other studies have reported that SGM fluidization can be induced by surface roughness textured on the scale of single constituents can trigger and promote rearrangements [16–20]. However, only few studies provided quantitative insights into how a systematic change of the roughness affects it. For micro-channels having rough walls patterned with pillars [19], only when their height is beyond a threshold value there is the "activation" of plastic rearrangements; moreover, an optimal height at which the wall fluidity reaches its maximum has been identified depending on the droplet diameter [21]. In cases where the wettability of the channel walls favors the adhesion of droplets, these can produce a "self-generated roughness" with enhanced boundary fluidity [20]. However, a direct analysis of the rate of plastic rearrangements and their spatial distribution is still lacking.

This thesis. In this work we report an extensive study on the effect of micro-grooves roughness in the microfluidic flow of dense emulsions. Only one face of the microchannel presented the micro-roughness, other was been left flat. In this way it was possible to compare the behavior of the emulsion in proximity of the two different walls under the same flow conditions. The fundamental questions that will be addressed in the course of this Thesis will be:

(i) What are the effects of controlled micro-roughness (transversal grooves) in the flow of dense emulsion? Is there a relation between the wall slip velocity and plastic rearrangements induced by the roughness?

(ii) Can we find a direct link between fluidization and the spatial distribution of plastic rearrangements?

(iii) Changing the rough elements' geometry is it possible to control and tune the emulsion flow?

(iv) How an asymmetric roughness can influence the velocity profile?

To properly address this questions, this manuscript is designed as follows:

In the first Chapter we introduce the fundamental concepts about rheology. Starting with the description of Newtonian behavior we then illustrate the main properties of non-Newtonian fluids. We describe the most common non-Newtonian behavior: shear-thinning, shear-thickening and viscoplasticity. At the end, we briefly discuss the origins of non-Newtonian behavior looking at the microscopic behavior of materials' constituents.

The second Chapter illustrates basic concepts about the physics of fluids at the microscale. In particular, we focus the description to the hydrodynamic equations that the behavior of Newtonian and non-Newtonian fluid in a parallel plane configuration. Then, we introduce the concept of slip velocity and discuss its role in the flow of complex fluids. Finally, we briefly illustrate the most important concepts regarding interfacial phenomena and wetting.

The third Chapter is devoted to the presentation of soft glassy materials (SGMs). These materials, characterized by an extremely slow internal dynamics, show peculiar and unique rheological properties halfway between liquids and solids. Emphasis is given to the description of concentrated emulsion, the model of SGM studied in this work.

In the fourth and fifth Chapter are illustrated some concepts of microfabrication and flow visualization. These two, are fundamental for the understanding of the experimental work presented in this Thesis.

The sixth Chapter describes the experimental details of this work. The first section describes the emulsion preparation and its characterization performed by optical imaging and rheological measurements.The second part deals with the fabrication of microfluidic channel. We realized the samples at the Institute of Physical Chemistry, Polish Academy of Science in Warsaw in the group of Prof. Piotr Garstecki. The last section describes the the μ-Particle Tracking Velocimetry apparatus and analysis software used to study the flow in microfluidic channels.

Seventh Chapter presents the results regarding the wall roughness effects on the flow of a dense emulsion. In this study we systematically investigate the effect of controlled roughness providing the first direct evidence that plastic rearrangements of droplets are all coordinated around rough elements. Experimental results are suitably complemented and confirmed by lattice Boltzmann numerical simulation. These numerical simulations are key to highlight the change in the spatial distribution of plastic rearrangements caused by the surface roughness and to elucidates the micro-mechanics behavior.

The eighth and last Chapter is dedicated to the conclusions of this PhD Thesis.

1. Complex fluids rheology

Rheology is the study of flow and deformation of materials under applied external forces. The measurement of rheological properties is applicable to substances which have a complex microstructure, such as muds, sludges, suspensions, polymers and other glass formers (e.g., silicates), as well as many foods and additives, bodily fluids (e.g., blood), or other materials which belong to the class of soft matter. According to how soft materials respond to the applied stress they can be divided into two large category labeled as Newtonian and non-Newtonian. This chapter deals with the description of the main properties of these two classes of fluids. Section 1.1 introduces Newtonian fluid behavior; section 1.2 deals with the description of non-Newtonian fluids. In this section different types of non-Newtonian properties are briefly described (e.g. shear-thinning, shear-thickening, viscoplastic). Section 1.3 collects representative examples of materials which, under appropriate circumstance, exhibit non-Newtonian behaviors. Finally section 1.4 briefly describes the origins of non-Newtonian behavior considering the influence of the externally applied stress on the material structure.

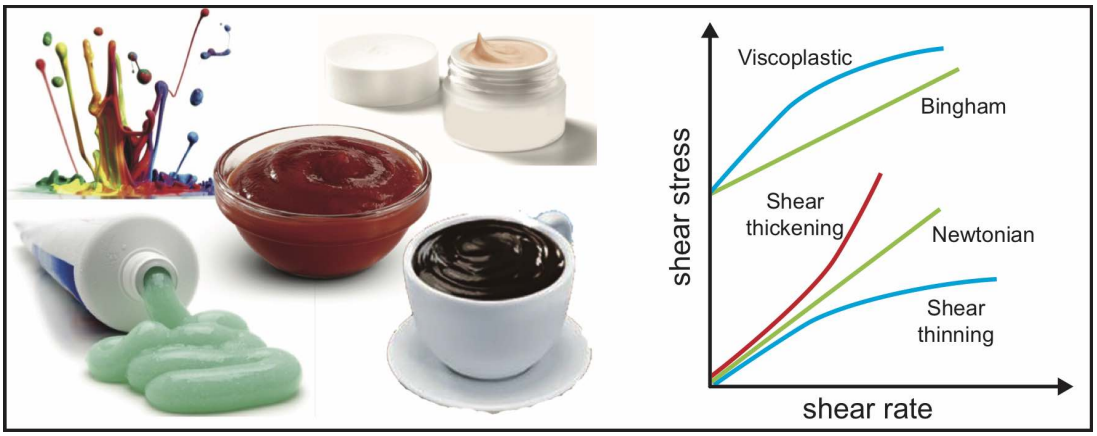

Introduction

Most of organic and inorganic liquids, solution of low molecular weight inorganic salts, molten metals and gases exhibit Newtonian flow characteristic. At constant temperature and pressure in simple shear system, the stress (σ) is proportional to the rate of shear ($\dot{\gamma}$) and the constant of proportionality is called the dynamic viscosity η. Such fluids are known as Newtonian fluids. During the past 50 years, in many industrial applications, materials have been introduced that do not conform the linear relation between σ and $\dot{\gamma}$. These fluids are known as non-Newtonian or complex fluids. In this category we can find: multi-phase fluids (foams, emulsions, dispersion and suspension), polymeric melts, or polymeric solutions. Table 1.1 are reported some example of substances exhibiting Newtonian or non-Newtonian behavior.

Table 1.1: Examples of materials exhibiting Newtonian (left) and non Newtonian (right) fluid behavior. For Newtonian fluids, the values of viscosity are indicated in brackets [22].

Newtonian Fluids	η **(Pa s)**	**non-Newtonian Fluids**
Air	10^{-5}	Cosmetics (creams, shampoos, toothpaste)
Water	10^{-3}	Biological fluids (blood, saliva, synovial fluids)
Glycerol	1.5	Dairy products (cheese, butter, yogurt)
Honey	10	Food (mayonnaise, ice-cream, jams)
Mercury	1.5×10^3	Adhesive (wall paper paste, glue)
Molten glass	10×12	Cement paste and slurries

§ 1.1. Newtonian liquids

To better understand the behavior of non-Newtonian fluids it is useful to begin with the description of Newtonian fluid. In simple shear configuration, as depicted in fig. 1.1a, a material of thickness h is confined between two parallel plates. The bottom plate is held fix and the upper plate is pulled with a velocity V in the x direction. The plate applies a shear stress to the material and causes a deformation from the equilibrium shape. For a Newtonian fluid the response is characterized by a linear relationship between the applied shear stress (σ) and the shear rate ($\dot{\gamma}$):

$$\sigma_{xy} = \eta \frac{V(y)}{h} = \eta \frac{du}{dy} = \eta \dot{\gamma}_{xy} \tag{1.1}$$

where η is defined as the dynamic viscosity (expressed in Pa s). For a Newtonian fluid the viscosity is a constant value depending on temperature, pressure; commonly the viscosity decreases with the temperature and increase with pressure [22, 23]. Moreover the viscosity depends on the inner structure of the fluids, i. e. the molecules weight, the strength of links and the interactions between neighboring molecules [23, 24]. Eq. 1.1 represents the simplest case where the shear component is only in the x direction. For the case of three dimensional flow, there are six shearing components and three normal components of the stress tensor see fig. 1.1b. Each element $\sigma_{i,j}$ represents the stress (force per unit area) acting in the i-direction on the plane

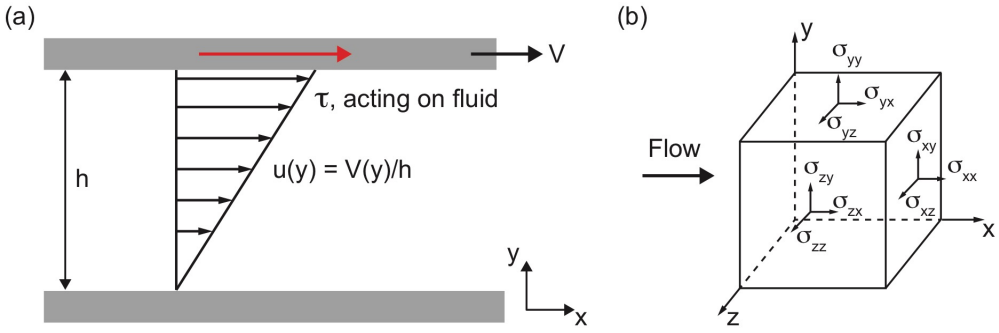

Figure 1.1: (a) Schematic representation of an unidirectional shearing flow. (b) Stress component in three dimensional flow.

with a normal oriented in the j-direction. The tensor $\overline{\overline{\sigma}}$ is symmetric and traceless [25], thus only three shear stresses σ_{xy}, σ_{xz}, σ_{yz} and two normal stress differences $N_1 = \sigma_{xx} - \sigma_{yy}$ and $N_1 = \sigma_{yy} - \sigma_{zz}$ must be specified. The quantities N_1 and N_2 are called, respectively, first normal stress difference and second normal stress difference. For a Newtonian liquid all the diagonal elements are equal: $\sigma_{xx} = \sigma_{yy} = \sigma_{zz}$. In fig. 1.2 are reported two typical shear stress-shear rate curves for Newtonian fluids.

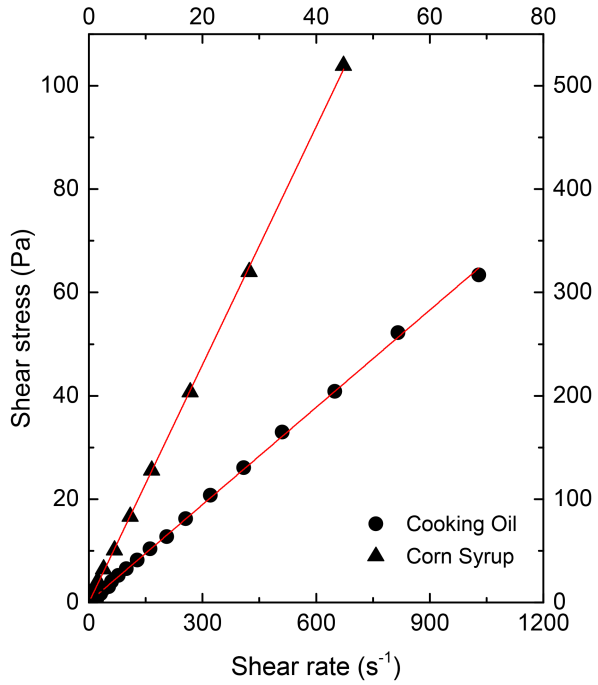

Figure 1.2: Typical shear stress-shear rate data for two Newtonian fluids. Data are reproduced from [22].

§ 1.2. Non-Newtonian fluids

The definition of non-Newtonian fluids is quite generic. In fact, in this category are included all those materials in which does not result a linear relationship between σ and $\dot{\gamma}$. The simplest possible deviation from the Newtonian behavior occurs when the simple shear curve stress vs. shear rate does not pass through the origin. Conventionally these fluids are grouped into three categories: 1) *Viscoelastic fluids*, 2) *Time-dependent fluids* and 3) *Time-independent fluids*. Of course, it is not always easy to follow this classification scheme because real materials often display a combination of these features. However, it is possible to identify the dominant non-Newtonian aspect and use it for subsequent process description.
In the following part we describe the main characteristics of time-dependent and viscoelastic fluids. Properties of the time-independent, instead, are describe in the section 1.3.

1. **Viscoelastic fluids**
   Viscoelastic fluids exhibit a behavior between an elastic Hookean solid and a purely viscous fluid. In a purely elastic situation the stress σ is a function of the strain ϵ (i.e., the displacement):
   $$\sigma = -G\frac{dx}{dy} = G\epsilon \tag{1.2}$$
   where G is the Young's modulus. In a purely viscous fluid, instead, the stress vs. strain relation is described by eq. (1.1). A viscoelastic behavior would thus be described by a combination of the two. The simplest model is the Maxwell fluid, which is equivalent to a spring connected in series with a dash pot as sketched in fig. 1.3a. Its constitutive law has the form:
   $$\sigma + \frac{\eta}{G}\dot{\sigma} = \eta\dot{\epsilon} \tag{1.3}$$
   This fluid behaves like a solid at short times scales with respect to the relaxation time $\lambda = \eta/G$ while it behaves as a viscous fluid at longer time scales. The total deformation ϵ of the fluid is given by the sum of elastic (ϵ_S) and viscous (ϵ_D) contribution:
   $$\epsilon = \epsilon_S + \epsilon_D = \sigma\left[\frac{1}{G} + \frac{t}{\eta}\right] \tag{1.4}$$
   Many materials (in particular polymeric melts and solutions, soap solutions, gels, emulsions or foams) exhibits viscoelastic behavior. One consequence of this type of fluid behavior is that shearing motion gives rise to stress (the so-called normal stress) in the direction normal to that of shear. The resulting normal stress differences N_1 and N_2, with $\sigma(\dot{\gamma})$ are normally used to characterize the viscoelastic fluids: a fluid is inelastic if ($N_1 \ll \sigma$) or viscoelastic with ($N_1 \gg \sigma$).
   The existence of such normal stress difference in a shear flow implies that curved streamlines exert a force in the radial direction, normal to the flow. This gives raise to phenomena like the Weissenberg effect, as shown in fig. 1.4, in which a viscoelastic fluid raises a vertical spinning rod because the centrifugal force is overcome by the normal stress difference of the fluid. Only viscoelastic fluids exhibit simultaneously properties of elastic solid and viscous

liquid, and therefore a characteristic relaxation time λ is introduced to describe this complex behavior. The characteristic relaxation times is responsible for the definition of the two most representative dimensionless number in rheology [26]: the Deborah number, defined as the relationship between the relaxation time and the duration of the deformation ($De = \frac{\lambda}{T}$); and the Weissenberg number, defined as the relaxation time multiply by the rate of deformation ($Wi = \frac{\lambda U}{L}$). While the Deborah number allows to distinguishing between solid-like ($De \uparrow$) and liquid-like ($De \downarrow$) behaviors of a particular material experiencing a deformation over a given time-frame, the Weissenberg number represents the ratio of elastic to viscous forces when a viscoelastic fluid is under flow. In general, Deborah and Weissenberg number are not equivalent and the latter is the one representing the non-linearity of the rheological response of a viscoelastic material [24].

2. **Time-dependent fluids**
   Many substances in food or pharmaceutical manufacturing sectors display a characteristic behavior that does not depend only from the applied shear stress or shear rate, but also of the duration for which the fluids has been subjected to shearing. Depending upon the response of a material to shear over a period of time, we can sub-divide time-dependent fluid behavior into two types, namely, thixotropy and rheopexy (or negative thixotropy) fluids.
   A material is classified as being thixotropic, if it is sheared at a constant rate, its apparent viscosity $\eta = \sigma/\dot{\gamma}$ (or the corresponding shear stress) decreases with the duration of shearing, as shown in fig. 1.5a. This decrease of the viscosity is visible in materials such as coal-in-water suspension, cement past or waxy crude oil. and it can be explained by the breakdown of the material structural linkage [27]. As opposite of thixotropic materials, there are a few systems [29] in which the imposition of external shear increases their apparent viscosities with the duration of shearing (fig. 1.5b). These materials are labeled as rheopectic material. The external shear fosters the build up of structure increasing the viscosity of the fluid.

3. **Time-independent fluids**
   In this sub-set of fluids, (also known as generalized Newtonian fluid) the shear rate is an only function of the shear stress in that point $\dot{\gamma} = f(\sigma)$. More specifically, in a generalized Newtonian fluid, the flow can instantaneously affect only the local viscosity, but not the

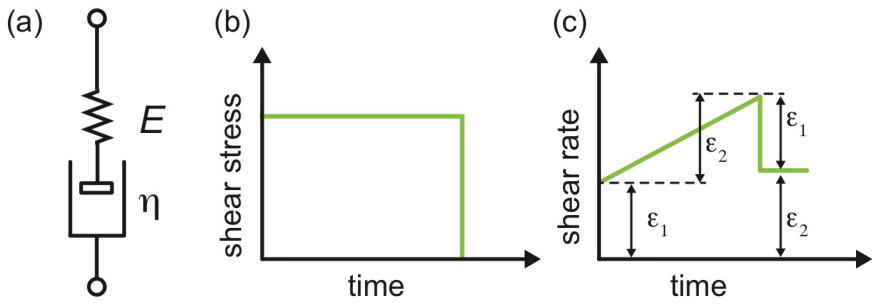

Figure 1.3: (a) Maxwell model for viscoelastic materials. Sketches of rheological curves for the Maxwell model: (b) shear stress vs time and (c) shear rate vs time.

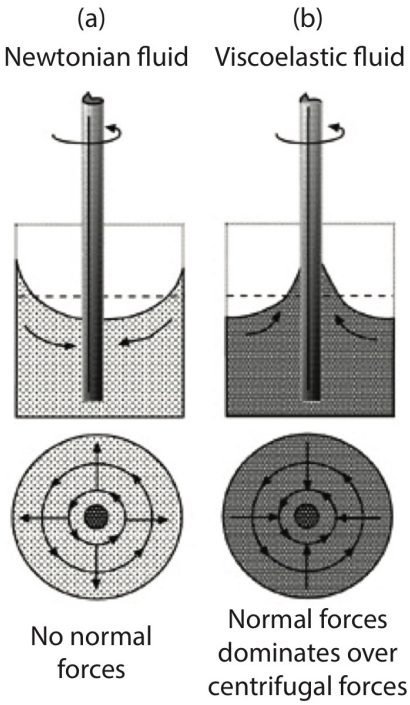

Figure 1.4: Rod climbing (Weissenberg effect). (a) In Newtonian fluids, centrifugal forces generated by the rotation push the fluid away from the rod. (b) In non-Newtonian fluids, normal forces are stronger than centrifugal forces and drive the fluid inward toward the rod.

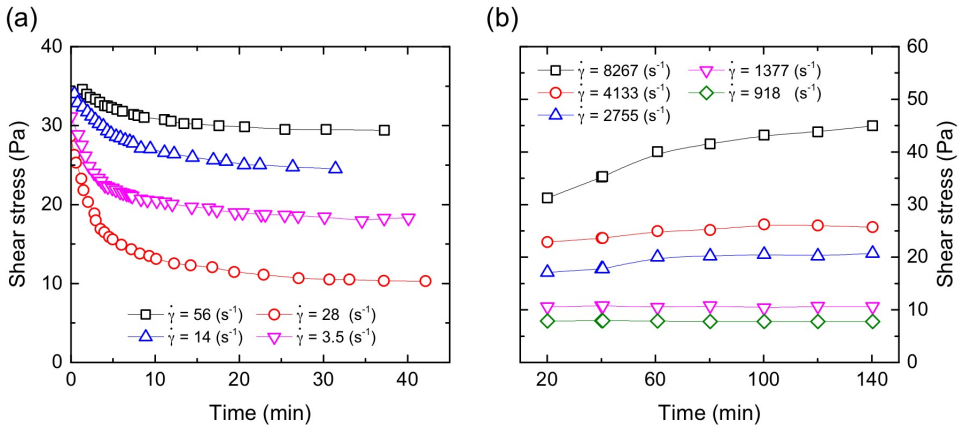

Figure 1.5: (a) Typical experimental data showing thixotropic behavior in red mud suspension. (b) Rheopectic behavior in a saturates polyester. Data are reproduced from [28] and [29].

structure of the stress tensor:

$$\sigma = \eta(\dot{\gamma})\dot{\epsilon} \tag{1.5}$$

Due to the importance and the large diffusion in the soft matter field, generalized Newtonian fluids properties are described in more details in the next section.

§ 1.3. Time-independent fluids

Depending upon the form of eq. (1.5), three possibilities exists:

- Shear thinning (or pseudoplastic behavior);
- Shear thickening (or dilatant behavior);
- Viscoplastic behavior (with or without shear thinning behavior);

In fig. 1.6 qualitative flow curves (also called rheograms) on linear coordinates for the above noted three categories of fluid behavior are reported; the linear relation typical of Newtonian fluids is also included. In the following part of the section we present in detail the properties, the models and the materials that characterize each of these categories.

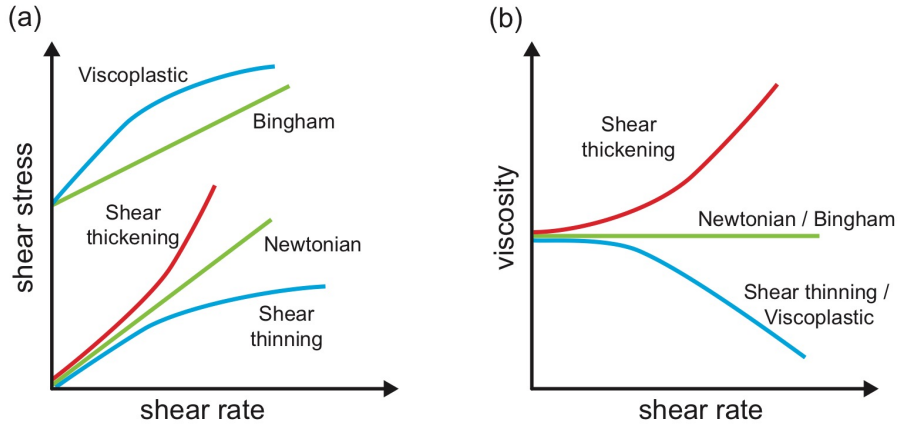

Figure 1.6: Sketch of rheological curves for Newtonian and generalized Newtonian fluids: (a) shear stress vs shear rate dependence and (b) corresponding viscosity trend as a function of shear rate. A Newtonian fluid has a constant viscosity, while for a generalized Newtonian fluid the viscosity varies with the shear rate.

§ 1.3.1. Shear thinning models

Shear thinning is the most widely encountered type of time-independent non-Newtonian fluid behavior. It is characterized by an apparent viscosity η (defined as $\sigma/\dot{\gamma}$) which decreases with the increasing of the shear rate.

In these systems, at low shear rates, the apparent viscosity (η_0) is independent of the shear rate like a Newtonian fluid. At high shear rates the fluids exhibits a similar plateau with the viscosity that reach a limit value η_∞. In most cases, the value of η_∞ is only slightly higher than the solvent viscosity η_S. This behavior is present for polymer solution as reported in fig. 1.7a. The graph shows the viscosity full spectrum of values going from η_0 to η_∞ for a solution of polyacrylamide (PAA) [30]. The infinite-shear limit is not present in polymer melts, foams or emulsions.

Thus, the apparent viscosity of a pseudoplastic substance decreases with the increasing shear rate, as are seen shown in fig. 1.7b for three polymer solutions where the rate of decrease of

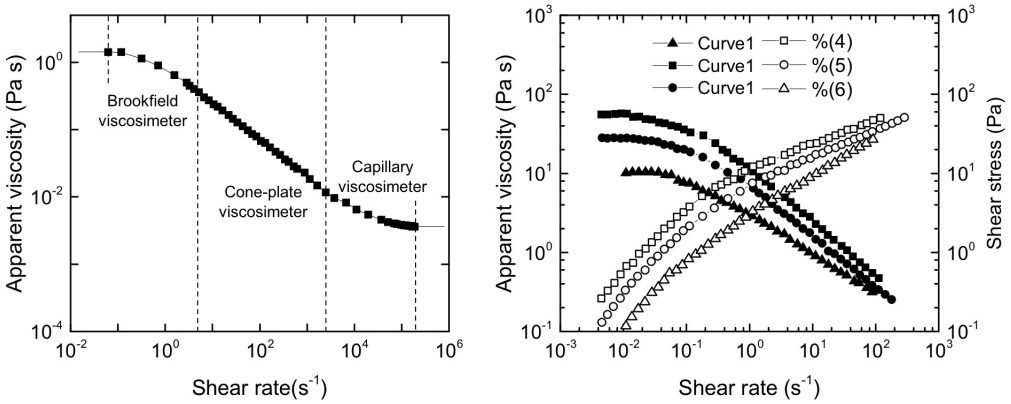

Figure 1.7: Characteristics rheograms for shear thinning system. (a) Demonstration of zero shear and infinite shear viscosities for a polyacrylamide solution. (b) Experimental data for three pseudoplastic polymer solutions [31].

viscosity is different from one system to another. The value of shear rate marking the onset of shear-thinning is influenced by several factors such as the type and concentration of polymer, the nature of solvent. For emulsion and suspensions other factors are: the concentration and the particle size or shape [31]. At the microscale the shear thinning effect can be explained as follow; polymer molecules which are coiled and entangled at low shear rates gradually become disentangled, and finally fully straighten out (fig. 1.8). All these changes in micro-structures facilitate flow, i.e., these lead to the lowering of their apparent viscosity with shear [23].

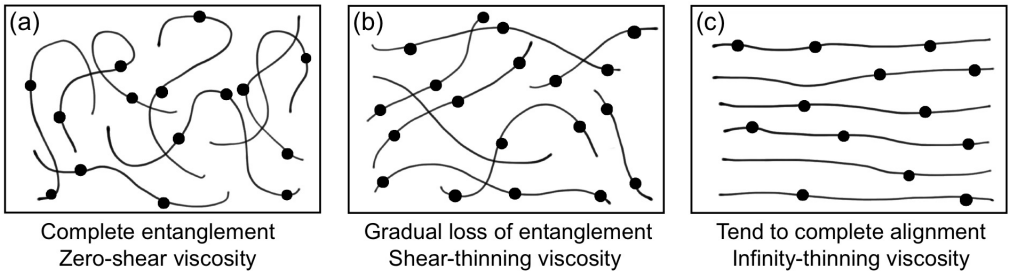

Figure 1.8: Schematic representation of macromolecules under the influence of shear.

Finding a relationship to describe shear thinning fluids it is not easy. Over the past years, several numeric or empirical models have been reported in literature [30, 32, 33]. A representative selection of commonly used expressions is given here. Often the relationship between shear stress-shear rate are plotted on log-log coordinates. The simplest approach to characterize a stress-dependent non-Newtonian fluid (both shear thickening or shear thinning) is to use a power law model

$$\sigma = m(\dot{\gamma})^n \tag{1.6}$$

in terms of the apparent viscosity

$$\eta = m(\dot{\gamma})^{n-1} \tag{1.7}$$

The exponent n is called *flow behavior index*, while m is called *flow consistency index*. For a shear-thinning fluid $n < 1$ while for shear thickening fluids $n > 1$. Many polymer melts and solutions exhibit the value of n in the range 0.3-0.7 depending upon the concentration and molecular weight of the polymer. Naturally, smaller is the value of n more shear thinning is the material. Although, eq. (1.6) and eq. (1.7) offers the simplest approximation of shear-thinning behavior, it predicts neither the upper nor the lower Newtonian plateaus in the limits of $\dot{\gamma} \to 0$ or $\dot{\gamma} \to \infty$.
In order to correct some of the weakness of the power law, Cross [34] presented the following empirical model. In simple shear is written as

$$\frac{\eta - \eta_\infty}{\eta_0 - \eta_\infty} = \frac{1}{1 + m(\dot{\gamma})^n} \tag{1.8}$$

This model predicts the shear thinning behavior for $n < 1$. Initially Cross proposed that $n = 2/3$ was correct for a large number of substances. Now it is used as an adjustable parameter which offers significant improvement in term of the degree of fit [34]. Another widely used model, which capture the shear thinning behavior, is given by the Carreau-Yasuda model

$$\eta(\dot{\gamma}) = \eta_\infty + (\eta_0 - \eta_\infty)(1 + (\lambda\,\dot{\gamma})^a)^{\frac{n-1}{a}} \tag{1.9}$$

where η_0 and η_∞ are the already introduced low shear rate and high shear rate limit viscosities, λ is a relaxation time, and a is a parameter affecting the shape of the curve. In this model, for high shear rates $\dot{\gamma}$ is practically equivalent (neglecting η_∞) to that of eq. (1.6).

§ 1.3.2. Shear thickening models

This class of fluids behaves in an opposite way respect to shear thinning system. In these systems, in fact, the apparent viscosity increases with increasing shear rate. The first quantitative study of shear thickening appears to have been in 1958 by Metzner and Whitlock [35], who studied the viscosity of suspensions of titanium dioxide TiO_2 in water and in sucrose solutions. Some of the results are reported in fig. 1.9. Other examples of fluids showing shear thickening behavior include SiO_2 colloidal suspensions, pastes of kaolin, corn flour in water, and polymer solutions. The origins for the large high-shear-rate viscosity has been argued to be due to an order–disorder

transition [36], hydrodynamically induced clustering [37, 38] surface coating interactions [39], and, most recently, friction [40–42]. Generally there must be a balance between shear forces and some force between particles at the point of close approach of the surfaces in order to exhibit the large transition in properties over a narrow range of stress or shear rate. Considering a concentrated suspension of solid particles, the origin of shear thickening behavior can be explained in term of friction: at rest, the liquid in the sample is sufficient to wet all the solid particles. At low shearing, the liquids lubricates the motion of each particle minimizing solid-solid friction. Consequently, the resulting stresses are small. At high shear rates, the mixture dilates (from here the name dilatant fluids) so that the liquid is no longer sufficient to prevent the direct solid-solid contact and friction. This leads to the development of a much larger shear stress.
To model this behavior it is possible to approximate σ - $\dot{\gamma}$ data by the power law model, eq. (1.6), with the power law index (n) taking values greater than unity.

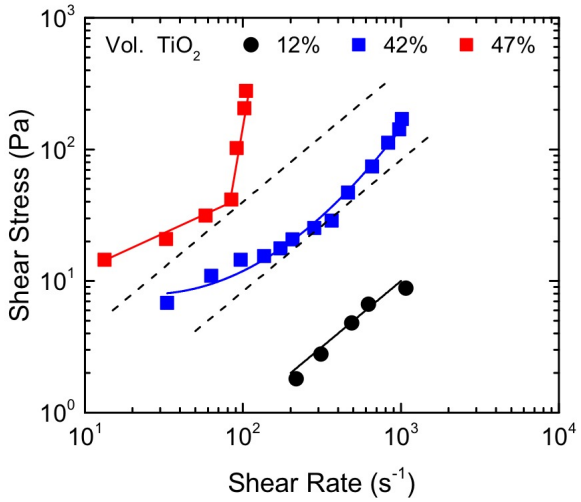

Figure 1.9: Typical shear stress vs shear rate data for TiO_2 suspension displaying shear thickening behavior. Dashed lines represents the Newtonian behavior. Data are reproduced from [35].

§ 1.3.3. Viscoplastic models

This type of non-Newtonian fluid behavior is characterized by the existence of a threshold stress, called yield stress σ_0, which must be exceeded for the fluid to deform (shear) or flow. Conversely, when the external applied stress is below σ_0 the material deforms like an elastic solid (Hookean behavior). Above this threshold value the fluid may exhibits Newtonian (constant viscosity) or shear thinning behavior.
It is possible to describe the internal dynamic as follow: at rest the material structures has a sufficient rigidity to resist any external stress less than σ_0 and there is an enormous resistance to flow. The material might deforms elastically, but for a stress levels above σ_0, the structure breaks down and the substance behaves like a viscous material. The built-up and the breakdown

of structure is reversible for a large number of material such us foams, emulsion or gels [43, 44]. In literature there are several models to describe this kind of fluids. A fluid with linear flow curve for $|\sigma| > \left|\sigma_0^B\right|$ is described by the Bingham model and it is characterized by a constant viscosity η_B. Thus in one dimension shear, the model is written as:

$$\sigma = \sigma_0^B + \eta_B \dot{\gamma} \qquad |\sigma| > \left|\sigma_0^B\right| \tag{1.10a}$$

$$\dot{\gamma} = 0 \qquad |\sigma| < |\sigma_0^B| \tag{1.10b}$$

On the other hand, a viscoplastic material showing shear thinning behavior above the yield stress value, σ_0, is known as a yield pseudoplastic fluid and it is described by the Herschel-Bulkley model:

$$\sigma = \sigma_0^H + m(\dot{\gamma})^n \qquad |\sigma| > \left|\sigma_0^H\right| \tag{1.11a}$$

$$\dot{\gamma} = 0 \qquad |\sigma| < |\sigma_0^H| \tag{1.11b}$$

Another used viscosity model for this viscoplastic fluids is the Casson model. This model has been introduced to describe the flow of blood, but it has been found a good approximation for many other substance [44, 45]. It is written as:

$$\sqrt{|\sigma|} = \sqrt{\sigma_0^C|} + \sqrt{\eta_C\ |\dot{\gamma}|} \qquad |\sigma| > \left|\sigma_0^C\right| \tag{1.12a}$$

$$\dot{\gamma} = 0 \qquad |\sigma| < |\sigma_0^C| \tag{1.12b}$$

Typical examples of yield-stress fluids include mayonnaise, yogurt, molten chocolate, gels, cosmetics, foams, suspensions, etc. Thorough reviews on the rheology and fluid mechanics of viscoplastic fluids are available in the literature [43, 44]. In fig. 1.10 are reported experimental data for a Bingham and for a yield pseudoplastic fluid.

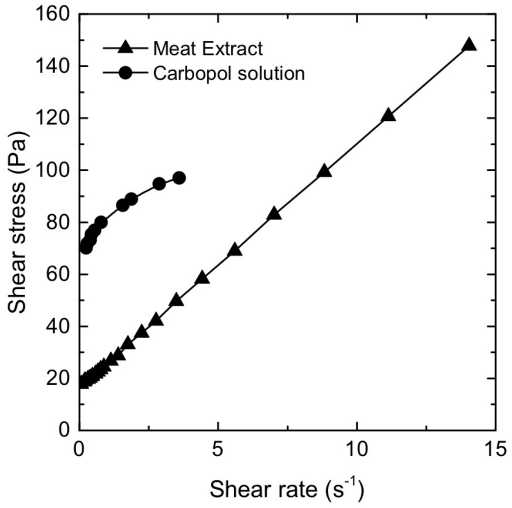

Figure 1.10: Shear stress-shear rate data for a meat extract and for a carbopol solution displaying Bingham plastic and viscoplastic behaviors respectively. Data are reproduced by [43, 44]

§ 1.4. Origins of Non-Newtonian Behavior

The foregoing discussion clearly established that there is a direct link between the type of non-Newtonian fluid behavior and the influence of the externally applied stress on the state of the structure. Thus, the measurements of rheological properties are frequently used to ascertain the state of the structure of a non-Newtonian fluid. Conversely, it is possible to design the structure of a substance to give the desires rheological properties. Before examining the role of the structure it is useful to introduce two key concepts used to describe the mechanics of fluids and and its properties like: η, σ_0, N_1, N_2, G.

1. *Continuum hypothesis*: while in general matter is made up of atoms, in some cases it is more convenient to disregard the molecular nature of a substance and view it as a continuous homogeneous matter with no vacancies, which is called a continuum. This assumption will be applicable only when the system is large in comparison to the distance between molecules.

2. *Spatial homogeneity*: the continuum allows to treat the properties of the system as point functions without any discontinuities. This leads to a homogeneous system which has the same properties at every point, without irregularities.

In fig. 1.11 we show various models of microstructures commonly found in complex fluids and their responses to applied shear. The most common systems contain particles with irregular shapes, with a size distribution (drop or bubbles in emulsion and foams), or branched molecules in the case of polymeric systems. When no shear is applied, microstructured units are oriented randomly corresponding to their minimum energy state. At low level of shearing, the system exhibits high resistance towards deformation showing a very high value of viscosity or a yield stress. Increasing the external shear stress, the structural units respond by aligning themselves with the direction of the flow (fig. 1.11a and b), or by deforming to orient along streamlines (fig. 1.11c), or by way of disintegration into small flow units or into primary particles (fig. 1.11d). Many other possibilities exist which contribute to micro-structural changes depending upon the relative magnitudes of various forces at play. For suspensions or multiphase systems it is possible to modify the components interaction working on surfactants or phases concentrations [46, 47]. For polymers instead, it is possible to change the polymerization rate or including different functional groups [48, 49].

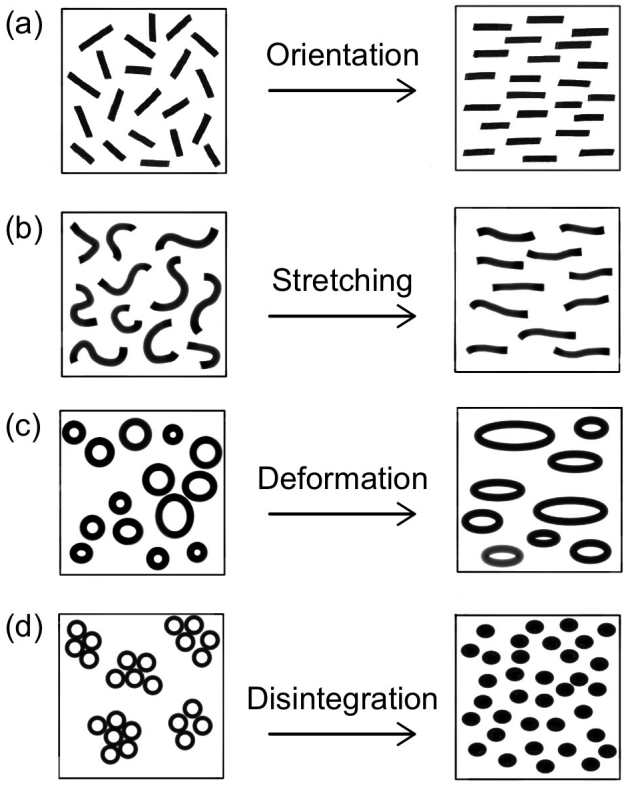

Figure 1.11: Schematics of structures in non-Newtonian dispersion at rest and under shear. (a) Orientation, (b) stretching, (c) deformation and (d) disintegration.

2. Physics of fluids at the microscale

Microfluidics is the science and technology of systems that process or manipulate small amounts of fluid (10^{-9}-10^{-18} liters), using channels with dimensions of tens to hundreds of micrometers. In fact, the behavior of fluids at the microscale can differ from "macrofluidic" behavior in that factors as surface tension, energy dissipation, and hydrodynamic resistance. In this chapter we introduce the basic concepts for describing the properties of fluids confined in microfluidic channel. At first, we introduce fundamentals hydrodynamic equations and review the concept of laminar flow, which dominates the flow in microfluidic devices. Then, we illustrate the constitutive equations that describe the flow of Newtonian and non-Newtonian fluid in a parallel plates configuration, focusing on the velocity and stress profiles. In section 2.4 we introduce the concept of slip velocity and discuss its features in the flow of complex fluids. Finally, we briefly illustrate the most important concepts regarding interfacial phenomena and wetting.

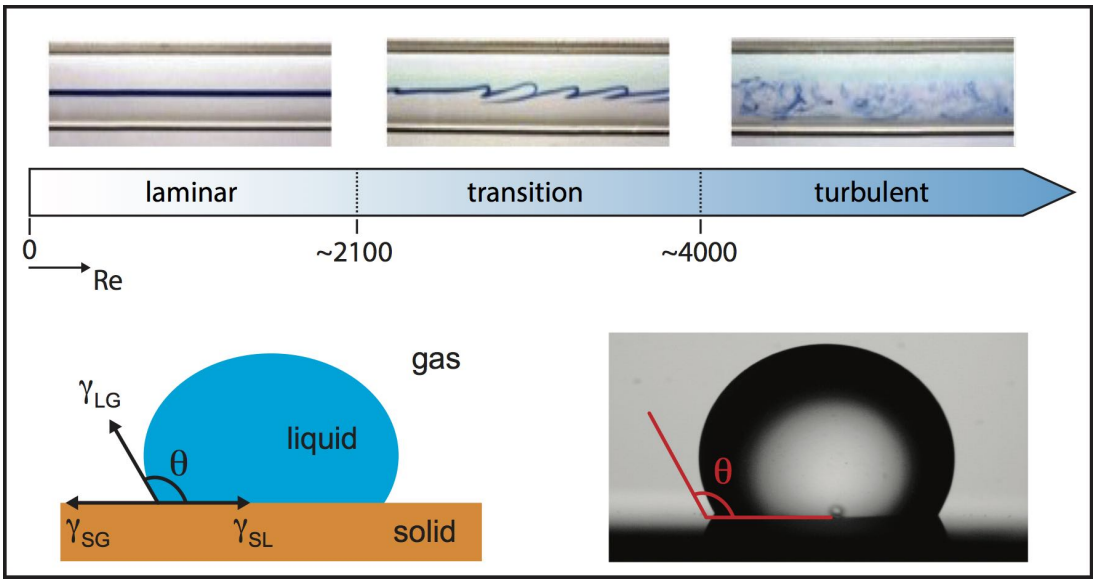

§ 2.1. Introduction

At the microscale the flow behavior differs from their macroscopic counterparts for two reasons: the small scale makes molecular effects more important, and it amplifies the magnitudes of certain ordinary continuum effects to extreme levels. For these reasons the flow inside a microfluidic channel is unique and presents properties that are not visible in the macroscopic world. One of the most famous of these properties is the laminar flow. This allows a very good control of the fluid transport, a low mixing rate and a probe for the local properties of the fluid [50–52]. The hydrodynamic of microfluidic channel can be numerically derived from classical mechanics. In the following section, these and other base concepts to explained the behavior of flow in confined system are reviewed.

§ 2.2. Hydrodynamics of the microfluidic system

Hydrodynamics is governed by two differential equations, which can describe most of the commonly occurring fluid flow. In the following treatment we neglect the molecular nature of the fluid and treat the liquid as a continuum (see section 1.4). Considering the plot in fig. 2.1, the continuum assumption holds whether the fluidic system presents a "fluid particle" (a volume containing a sufficiently number of particle, much smaller than the size of the system) which can be located on the density plateau [53].

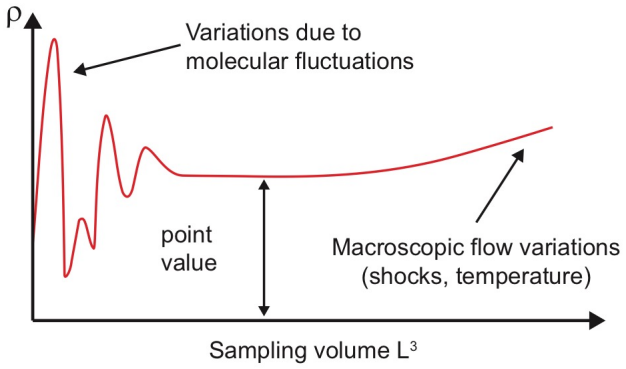

Figure 2.1: Continuum assumption in fluids illustrated by a thought experiment that consists in measuring the density of a fluid sample of volume L^3.

Furthermore, we assume that the liquid is incompressible, which is a good approximation for all aqueous solutions [25]. The incompressibility criterion together with the principle of mass conservation leads to the fist of the two equations: the so called continuity equation. Which in vectorial form is:

$$\frac{\partial \rho}{\partial t} + \nabla \cdot (\rho \mathbf{u}) = 0 \tag{2.1}$$

where ρ is the density and $\mathbf{u}$ is the velocity vector. The equation means that the mass of a liquid flowing into any volume V over a period of time must be balanced by the amount flowing out. The second equation describes the velocity field applying the Newton's second law of motion to

a small block of fluid

$$\rho\left(\frac{\partial \mathbf{u}}{\partial t} + \mathbf{u}\cdot\nabla(\mathbf{u})\right) = \mathbf{F}_{ext} + \nabla\cdot\overline{\overline{\sigma}} \tag{2.2}$$

In this equation $\mathbf{F}_{ext}$ is an external force (i.e., gravitational force $F = \rho g$) and $\overline{\overline{\sigma}}$ is the stress tensor. It's now necessary to write a constitutive law between the stress and the velocity gradient. Considering a Newtonian fluid, for whom, the stress tensor is linearly related to the deformation tensor we obtain the Navier-Stokes equation

$$\rho\left(\frac{\partial \mathbf{u}}{\partial t} + \mathbf{u}\cdot\nabla(\mathbf{u})\right) = -\nabla p + \eta\nabla^2\mathbf{u} + \mathbf{F}_{ext} \tag{2.3}$$

where ∇p is the pressure (p) gradient and $\eta\nabla^2\mathbf{u}$ is the viscous force. The term on the right of the equal sign represent the total force per volume unit acting on the block of fluid. The term on the left refers to the inertial contribution.
The unknowns in eq. (2.3) are the velocity and the pressure field, which can be determined by solving the Navier-Stokes equations subject to a specific boundary conditions (BCs).

§ 2.2.1. Reynolds number

The Reynolds number (Re) is an important dimensionless quantity in fluid mechanics used to help predict flow patterns in different fluid flow situations. Re is defined as the ratio of inertial forces to viscous forces within a fluid, which is subjected to relative internal movement due to different fluid velocities. For a stationary incompressible flows, characterized by one single spatial scale l, the Reynolds number is expressed by

$$\mathrm{Re} = \frac{\rho\, u\, L}{\eta} = \frac{[inertia\, forces]}{[viscous\, forces]} \tag{2.4}$$

where ρ is the fluid density, η is the dynamic viscosity, and u is the velocity of the fluid in a channel with a characteristic length L (e.g. the channel diameter). Reynolds number allows to evaluate if the flow of a fluid is in a laminar regime or in a turbulent regime; however care must be taken as there are other factors which may influence the flow regime of a fluid. In the case of a straight pipe the flow regimes and the corresponding Reynolds Number are:

- Laminar flow: $\mathrm{Re} \lesssim 2100$
- Transition flow: $2100 \lesssim \mathrm{Re} \lesssim 4000$
- Turbulent flow: $\mathrm{Re} \gtrsim 4000$

In microfluidics, a typical channel has a diameter of about 100 μm; filled with water (ρ=1000 Kg/m^3, η=10^{-3} Pa s) which moves at velocity of a few mm/s, shows a Re $\sim$ 0,1. The laminar flow in microfluidic system, allows to control in a very precise way the fluids inside the channel. Moreover, when Re is very small the non linear term in the Navier-Stokes equation for momentum

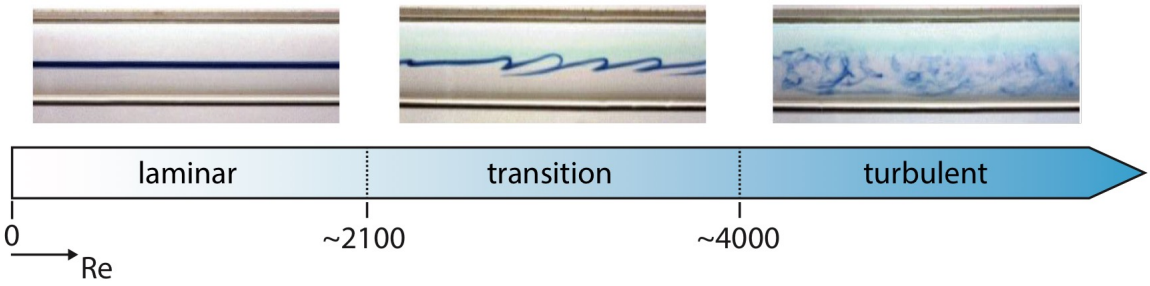

Figure 2.2: Transition from laminar (Re $\lesssim$ 2100) to turbulent flow (Re $\gtrsim$ 4000).

conservation disappear, resulting in the Stokes flow equation

$$\mathbf{F}_{ext} - \nabla p + \eta \nabla^2 \mathbf{u} = 0 \tag{2.5}$$

In the absence of free surfaces or interfaces, the flows governed by the Stokes equation posses remarkable properties: linearity in velocity, reversibility, uniqueness of solution, reciprocity, and the existence of a minimum of kinetic energy dissipation [25, 50].

§ 2.3. Parallel plates flow

The Navier-Stokes equation contains the non linear term of inertial forces. Hence, it is difficult to obtain, both analytically and numerically, a solution for general flow. The strict solutions are obtained only for some special geometries. One of these is the flow between two infinite parallel planes (see fig. 2.3). In this section we describes the flow of incompressible fluid in this simple configuration that is a good approximation of a common microfluidic channel [25].

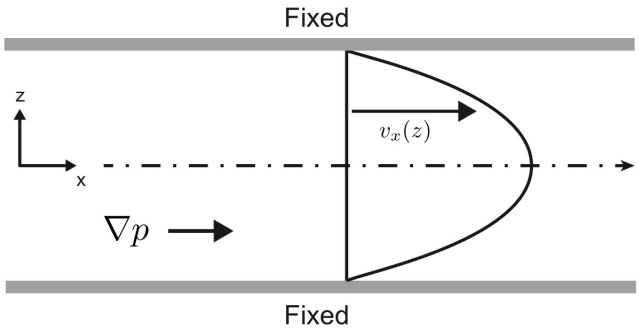

Figure 2.3: Schematic representation of infinite plates geometry.

For the case of a parallel flow, the Navier-Stokes equation is extremely simple and the velocity vector has only one non zero components

$$\mathbf{u} = (u(z), 0, 0) \tag{2.6}$$

where z is the traverse direction normal to the flow. Since the flow is steady and fully developed

there are no variation in time and in x, y directions

$$\frac{\partial}{\partial t} = \frac{\partial}{\partial x} = \frac{\partial}{\partial y} = 0 \tag{2.7}$$

Since the flow is completely independent of y, momentum equation yields

$$\frac{\partial p}{\partial y} = \sigma_{xy} = \sigma_{yy} = \sigma_{zy} = 0 \tag{2.8}$$

Combining these equations the Navier-Stokes can be greatly simplified

$$u = u(z) \tag{2.9}$$

$$\frac{\partial p}{\partial x} = \frac{d\sigma_{xz}}{dz} \tag{2.10}$$

$$\frac{\partial p}{\partial z} = \frac{d\sigma_{xz}}{dz} \tag{2.11}$$

let

$$P = p - \sigma_{zz} \tag{2.12}$$

Since P is independent of z eq. (2.10) becomes

$$\frac{\partial P}{\partial x} = \frac{d\sigma_{xz}}{dz} = C \tag{2.13}$$

where C is a constant. This equation hold for both Newtonian and non-Newtonian fluids.

§ 2.3.1. Newtonian fluid flow

As described in the constitutive equation for Newtonian fluid is linear relation between the stress $\overline{\overline{\sigma}}$ and the shear rate $\dot{\gamma}$:

$$\overline{\overline{\sigma}} = \eta\overline{\overline{\dot{\gamma}}} \tag{2.14}$$

For the parallel flow we can write the stress tensor as

$$\overline{\overline{\sigma}} = \begin{pmatrix} 0 & 0 & \eta\frac{du}{dz} \\ 0 & 0 & 0 \\ \eta\frac{du}{dz} & 0 & 0 \end{pmatrix} \tag{2.15}$$

so, substituting

$$\frac{dP}{dx} = \frac{dp}{dx} = C = \eta\frac{d^2u}{dz2} \tag{2.16}$$

With non-slip conditions applied to both walls

$$u\left(z = \pm\frac{h}{2}\right) = 0 \tag{2.17}$$

the solution of eq. (2.16) is

$$u = \frac{1}{2\eta}\frac{dp}{dx}\left(z^2 - \frac{h^2}{4}\right) \tag{2.18}$$

This is the velocity distribution along the z direction. It is clear that u has a parabola shape and the maximum occurs at mid-channel. It is also possible to calculate the shearing stress due to the viscosity of the fluid

$$\sigma = \eta\frac{du}{dz} = \frac{1}{2}\frac{dp}{dx}z \tag{2.19}$$

The velocity distribution and stress profile along the z direction are reported in fig. 2.4.

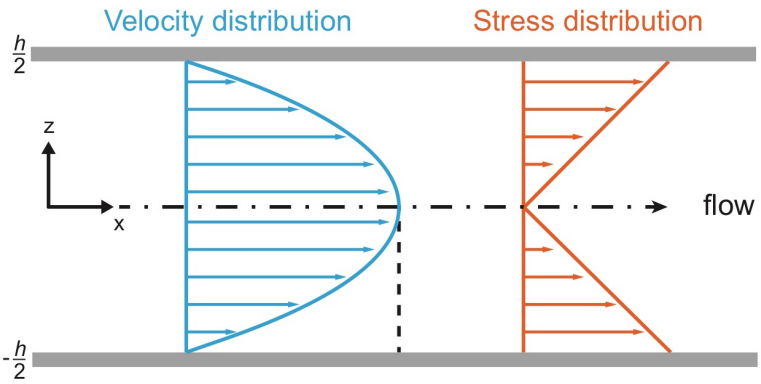

Figure 2.4: Schematic representation of velocity (blue) and shear stress distribution (orange) in fully developed laminar flow of Newtonian fluid in parallel plane geometry.

§ 2.3.2. non-Newtonian fluid flow

Let us consider the case of a non-Newtonian fluids. In particular we focus our description on Bingham viscoplastic fluid. These fluids do not deform unless the magnitude of the applied shear stress exceeds the yield stress. As introduced in Chapter 1 the constitutive equations for this class of fluid are:

$$\begin{aligned} \dot{\gamma} &= 0 && \sigma < \sigma_Y \\ \dot{\gamma} &= \frac{\sigma - \sigma_0}{\eta} && \sigma > \sigma \end{aligned}$$

where σ is the yield stress. As for the Newtonian case the flow is parallel between the two planes and the only non-vanishing component of σ is σ_{xz}. Due to the channel symmetry, only the upper half channel will be considered where $0 < z < \frac{h}{2}$. Substituting previous equations we obtain:

$$\begin{aligned} \frac{du}{dz} &= 0 && \sigma < \sigma_0 \\ \frac{du}{dz} &= \frac{\sigma_{xz} - \sigma_0}{\eta} && \sigma > \sigma_0 \end{aligned} \tag{2.20}$$

Below the yield stress exists a plug region where the velocity profile is flat. The size of this plug region (z_p) can be calculated from

$$z_p = \left(\frac{\Delta P}{L}\right)^{-1} \sigma_0 \tag{2.21}$$

Due to this considerations we can write the conditions of eq. (2.20) as a function of the size of the channel

$$\begin{aligned} \frac{du}{dz} &= 0 && , z < z_P \\ \frac{du}{dz} &= \frac{\Delta P}{L}\left(\frac{z - z_P}{\eta}\right) && , 0 < z < \frac{h}{2} \end{aligned} \tag{2.22}$$

Solving the two equations with the same boundary conditions of section 2.3.1 we obtain the velocity profile that is described by

$$\begin{aligned} u_p &= \frac{1}{2\eta}\frac{\Delta P}{L}\left(\frac{h}{2} - z_p\right) && 0 < z < z_0 \\ u &= \frac{1}{2\eta}\frac{\Delta P}{L}\left(z^2 - \frac{h^2}{4}\right) + \frac{\sigma_Y}{\eta}\left(z - \frac{h}{2}\right) \end{aligned}$$

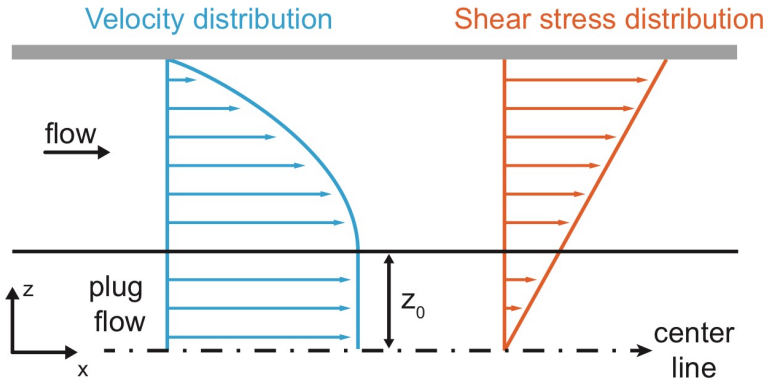

Figure 2.5: Schematic representation of velocity (blue) and shear stress distribution (orange) in fully developed laminar flow of Bingham plastic fluid in parallel plane geometry.

§ 2.4. Slip velocity

The solutions presented in section 2.3 were calculated under the no-slip BC, following the derivation presented in most textbooks of continuum fluid dynamics [25, 50]. This condition is illustrated in fig. 2.6a, where the velocity of a moving liquid is shown to decrease as the vertical distance to the lower static wall decreases until, at contact with the solid surface, the liquid velocity is zero. The absence of slip at the surface creates a boundary layer in the flow field where the viscous effects and velocity gradients are substantial.

Several explanations for its physical foundation have been proposed and the most common factor is the presence of forces, which could be described generically as frictional or viscous, that inhibit the movement of the fluid particles over the solid surface. Forces that influence the adherence of fluids to solid surfaces, and hence determine the effect of stick and slip, include viscous, elastic, inertial, hydrodynamic, electrostatic, magnetic, gravitational, and van der Waals [54]. These forces could play various roles in different flow systems under different circumstances and flow regimes. The no-slip condition is experimentally verified in numerous cases by direct observation

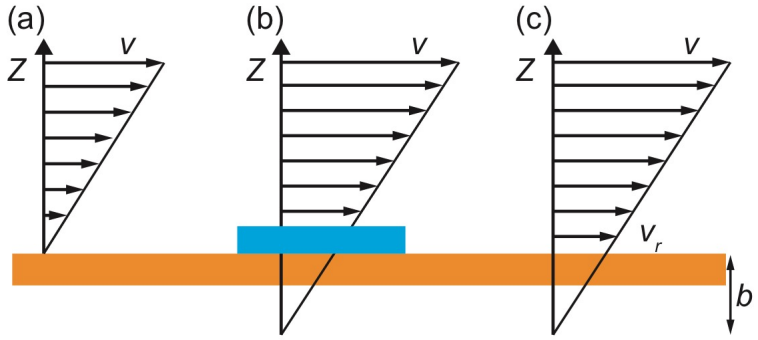

Figure 2.6: Schematic representations of (a) the no-slip BC, (b) the stagnant layer BC and (c) the partial slip BC. The length of the arrows is proportional to the velocity of the liquid. Under no-slip and stagnant layer BC the relative velocity, v, between the fluid and the solid wall is zero at the wall. In the slip BC, slip occurs at the wall, where $v = v_r > 0$. The extent of slip is characterized by the slip length b.

especially considering Newtonian fluid at low Reynolds regime [55–57]. Similarly, a non zero slip velocity at wall is confirmed in a large number of experimental studies for a range of fluids and flow geometries [54, 58–61]. In this case it is useful to introduce the concept of slip length, which is a simple measure of slip magnitude. It can be interpreted as the extrapolation distance inside the solid at which the fluid velocity relative to the wall vanishes as depicted in fig. 2.6c [59, 62–64]. The slip length is generally positive, it may also be negative when there is a stagnant layer at the interface and the nonslip discontinuity lies inside the fluid rather than inside the solid as depicted in fig. 2.6b [65]. The existence of such stagnant layer may be explained by the presence of a stronger fluid-solid interaction than the interaction within the fluid itself.

§ 2.4.1. Slip Factors

Direct experimental evidence supported by computer simulations indicate strong correlation between wall slip and fluid-surface interaction. However, it is virtually impossible to quantify this correlation analytically or empirically or even computationally due to the involvement of many delicate and interacting aspects. Nonetheless, some general parameters, such as contact angle and surface tension, have been used as approximate indicators to quantify the strength of the fluid-solid interaction [66]. There are several factors that control the fluid-solid interaction. One of these factors is the type of fluid and its properties such as viscosity, yield-stress, elastic modulus and density [56, 67–69]. In the case of multi-component fluids, such as emulsions,

slip can depend on the concentration, particle size (absolute and relative to the size of flow duct), particle shape and molecular weight. The slip length in multi-component fluid systems is generally larger than that in single-component fluid systems [70]. Another factor is the physical and chemical properties of the surface [63]. Hence, the material and composition of the surface, as well as the presence of surface active impurities, can have a strong influence on the onset and magnitude of slip. The deposition of a very thin film or particles from another phase, can change the surface properties, such as wettability and roughness, and hence affect wall slip [56, 63, 68, 71].
A third factor that affects slip is the flow regime, as measured by the Reynolds number of the flow system [72]. Slip therefore depends on the rate of deformation and laminar/turbulent flow conditions. And finally, the ambient conditions, such as temperature and pressure [73, 74], also have an impact on the onset and magnitude of slip either through a change in the properties of fluid and/or surface, or through a change in the nature of fluid-solid interaction [75].

§ 2.4.2. Wall slip in complex fluids

Wall slip occurs in Newtonian as well as non-Newtonian fluid systems [59, 63, 76, 77], although its occurrence in non-Newtonian is more common than in Newtonian [78, 79]. The reason is that the complexity of non-Newtonian fluids, especially multi-component fluids, allows the introduction of many factors that promote this phenomenon.
Experimental observations indicate that the slip contribution to the flow rate increases with increasing wall shear stress in the shear-thickening fluids, while it decreases in the shear-thinning fluids [75, 80, 81]. Similar behavior is observed in the case of yield-stress fluids. Moreover there is normally an apparent yield due to slip at lower stress than the bulk yield-stress. This could obscure the viscoplastic nature of the material because the apparent flow due to slip hides the yield-stress behavior [82, 83]. Because the local stress is below the yield value except possibly at the boundary region, no yielding occurs except at a very thin layer adjacent to the surface, which serves as a lubricating slip film. There is also the possibility that the sliding occurs through a depleted inhomogeneous layer from the continuum phase, or through a film from another phase which exists on the surface prior to the contact or is deposited on the surface from the bulk phase [9, 22, 84].
In an experimental study on the flow of highly concentrated suspensions of soft particles, it has been reported [85–87] that depending on the value of the applied stress three regimes of slip have been detected: at low stress (at and below yield stress) the flow is entirely due to wall slip, slightly above the yield-stress both bulk flow and slip have significant contribution to the fluid motion, and well above yield stress the slip is negligible and the flow is almost entirely due to bulk deformation.
Bécu and coworkers suggest that the origin of the wall slip can be described by the existence of a lubricant layer located near the walls and composed of continuous phase dragged from the bulk emulsion [85]. These thin film are far less viscous than the bulk material and thus likely to experience a stronger shear. A simple picture can be draw that could explain this phenomenon, introducing the model of apparent slip [80, 85, 86]. In this model the slip occurs

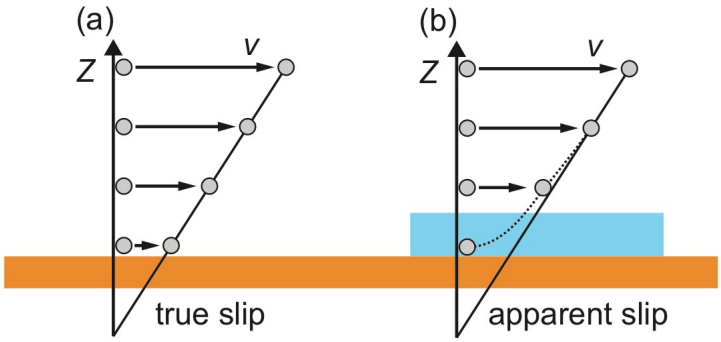

Figure 2.7: Schematic representation of true slip (a) and apparent slip (b) . The length of the arrows is proportional to the velocity of the liquid and the circles indicate molecules in the liquid before and after flow has occurred. The light blue shaded region indicates a thin layer of liquid attached to the solid wall.

not at the solid/fluid interface but at the fluid/fluid interface. This happens if a thin layer of liquid molecules is tightly bound to the solid surface, but the velocity gradient close to the solid is so high that the molecules beyond this layer appear to slide on the surface. This picture can be applied in the situation described above where soft particles slide on top of a static layer of solvent.

§ 2.5. Wetting

In the micro-world interfaces play a crucial role with respect to the "bulk" system, also referred as systems of "ordinary" size. In fact, in micro-systems the surface-to-volume ratio in much higher (by several order of magnitude) rather than in macro-systems. In this section are described some quantities and phenomena occurring at the interface like the surface tension and the wetting properties of a surface. These are crucial for the analysis and the understanding of some experimental situations in this Thesis.

§ 2.5.1. Surface tension

It is well known that to create a new surface is necessary to supply energy. Suppose one wants to distort a liquid to increase its surface area by an amount dA. The required work is proportional to the number of molecules that must be moved to the surface. We can write

$$\delta W = \gamma \cdot dA \tag{2.23}$$

where γ is the surface tension. Dimensionally, $[\gamma] = EL^{-2}$. The surface tension is thus expressed in units of J/m^2 or N/m.
Thermodynamically it can be defined as the increase in internal energy U or in free energy F that accompanies an increase in surface area

$$\gamma = \left[\frac{\partial F}{\partial A}\right]_{T,V,n} \tag{2.24}$$

where T is the temperature, V in the total volume and n is the number of molecules.
The physical origin of γ is related to the intermolecular interaction existing between surfaces: to detach them it is necessary to apply an energy $E = 2\,\gamma$. A microscopic model for surface tension between liquid and a gas is sketched in fig. 2.8. A molecule in the bulk forms chemical bonds with the neighboring molecules. A molecule at the surface cannot form as many bonds since there are almost no molecules in the gas. This lack of chemical bonds results in higher energy for the surface molecules. This is exactly the surface tension: it cost energy to form a surface. The order of magnitudes of the surface energy for water/air interface at 20°C is about $72.9\,\mathrm{mJ/m^2}$, while for an ethanol/air interfaces, the surface energy is on the order on $23\,\mathrm{mJ/m^2}$.

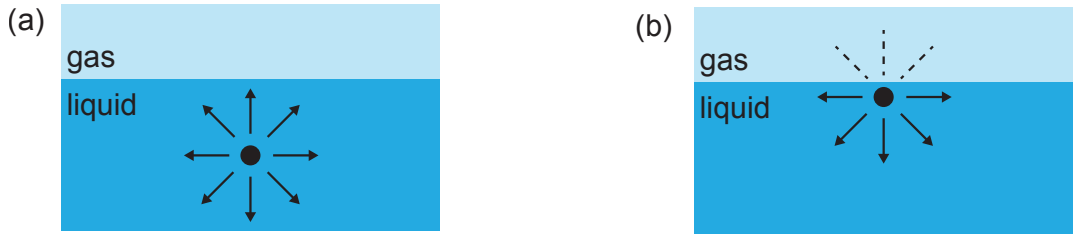

Figure 2.8: The origin of surface tension for a liquid/gas interface. (a) A molecule in the bulk of the liquid forms (non-permanent) chemical bonds (arrows) with the neighboring molecules surrounding it. (b) A molecule at the surface of the liquid misses the chemical bonds in the direction of the surface (dashed lines).

§ 2.5.2. Wetting and Contact angle

In microfluidics a fundamental concept in the theory of surface effect is the contact angle that appears at the contact line between three different phases, typically a solid surface a liquid and a gas. Thus, we have three interfaces: solid/gas, liquid/solid and liquid/gas. Between each of these interfaces there is an associated surface energy γ_{SG}, γ_{SL}, γ_{LG} respectively. A fundamental parameter is the spreading coefficient S, which is defined by

$$S = \gamma_{SG} - \gamma_{SL} - \gamma_{LG} \tag{2.25}$$

The system is in mechanical equilibrium when the resultant of the forces, at the contact line, is zero. This condition is satisfy when

$$\gamma_{SG} - \gamma_{SL} = \gamma_{LG} \cos\theta \tag{2.26}$$

or

$$\cos\theta = \frac{S}{\gamma_{LG}} + 1 \tag{2.27}$$

Equation (2.26) is known as the Young's equation. There are three different situations according to the value of the spreading coefficient S:

1. $S \geq 0$. Total wetting. Mechanic equilibrium cannot be reached. A small drop of the liquid on the solid surface spreads out to form a uniform layer. The contact angle θ is zero.

2. $S \leq \gamma_{LG}$. No wetting. Mechanic equilibrium cannot be reached. The liquid adopts a shape that minimizes the contact area with the solid.

3. $\gamma_{LG} < S < 0$. Partial wetting. Mechanic equilibrium is reached for a contact angle defined by the Young's relation [88].

Figure 2.9: (a) Sketch of droplet on a flat surface with a static contact angle θ resulting from the balance between γ_{SG}, γ_{SL} and γ_{LG}. The contact angle θ is defined as the angle between the solid/liquid and the liquid/gas interfaces at the contact line. (b) Picture taken from a measurement of the contact angle of a water drop on hydrophobic surface.

A surface that a liquid can partially wet is said to be "hydrophilic" when the contact angle is smaller then 90°, and a surface is called "hydrophobic" when the contact angle is higher then 90°. If the contact angle is above 150° the surface is "superhydrophobic".

§ 2.5.3. Wetting on rough surfaces

The wetting properties of a solid surfaces are affected by two main factor: the surface energy and the surface geometry. As described in the previous section, the surface energy is an intrinsic property of a material and it can be controlled by chemical modification [89, 90]. For example the surface roughness of a hydrophobic solid can be tuned in order to increment its hydrophobicity and obtain a superhydrophobic solid surface [91]. Basically, there are two distinct theories to describe and model the apparent contact angle on a rough surface: the Wenzel [92] and Cassie-Baxter [93] models.

Wenzel model. It is used to describe the effect of a physical roughness on surface, when it is completely wetted as shown in fig. 2.10a. The apparent contact angle θ^* is

$$\cos\theta^* = r\cos\theta^Y \tag{2.28}$$

where θ^Y is the Young contact angle and r is the roughness of the surface, defined as the ration of the actual over the apparent surface area of the substrate ($r > 1$). The roughness parameter always increase the original wetting properties

- Hydrophilic surface ($\theta_Y < 90°$), $\theta^* < \theta_Y$
- Hydrophobic surface ($\theta_Y > 90°$), $\theta^* > \theta_Y$

Cassie-Baxter model. It can be used for describe both rough or flat bu chemically heterogeneous surface. Considering a surface composed by two different species, each characterized by its own contact angles θ_1 and θ_2. The fraction occupied by the two are define respectively f_1 and f_2, therefore $(f_1 + f_2) = 1$ as depicted in fig. 2.10b. The apparent contact angle θ^* can be described as

$$\cos\theta^* = f_1 \cos\theta_1 + f_2 \cos\theta_2 \tag{2.29}$$

A particular case is when one of the two species is air. This is quite common working with rough surfaces, where a small quantity of air can be trapped between the surface and the liquid (see fig. 2.10c). In this case the Cassie-Baxter equation for the apparent contact angle is

$$\cos\theta^* = r_f \cos\theta_Y + f - 1 \tag{2.30}$$

where r_f is the roughness ratio of wetted area and f is the fraction of the drop base touching the solid surface. This is the case of superhydrophobic surfaces, where the liquid droplets are not able to wet the surface. In nature the most common example of superhydrophobic surface is the lotus leaf, famous for the self-cleaning property [94]. In this condition the droplet shows a very weak adhesive force on the surface and it is free to move.

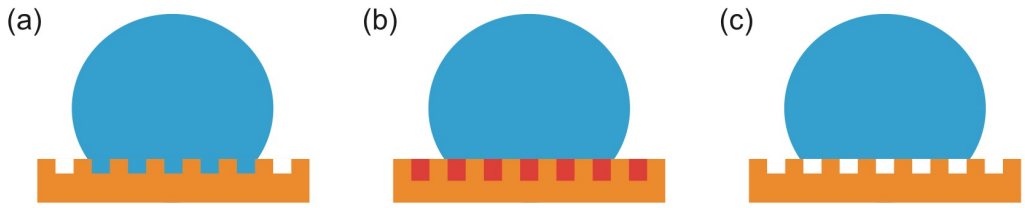

Figure 2.10: Scheme of Wenzel and Cassie-Baxter models: (a) Scheme of roughness surface related to Wenzel state. (b) Cassie-Baxter state in the case of flat, but chemically patterned surface and (c) roughness surface. This last particular case is used to describe the superhydrophobicity.

3. Soft Glassy Materials

"Soft Matter" is a widely diffuse term for materials that easily deformed by external forces and by thermal fluctuations. This category includes a large variety of materials, typically composed of polymers, colloids, liquid crystals, surfactants, and other mesoscopic constituents. All of these have a similar dynamics described by timescale of seconds rather than hugely longer or shorter times. A particular branch of these materials are Soft Glassy Materials (SGMs). They are amorphous materials characterized by an extremely slow internal dynamics. As a result, SGMs show peculiar and unique rheological properties halfway between liquids and solids. In the first section of this chapter SGMs are introduced focusing on the general properties of these material. Section 3.2 describes the properties and the main characteristics of dense emulsion, the SGM used in during this thesis. The third section describes the main rheological properties of SGMs focusing on flow mechanisms and recent development regarding the cooperativity and fluidity concept. In the last section of the chapter (section 3.4) two models, used to describe the flow of SGMs are presented.

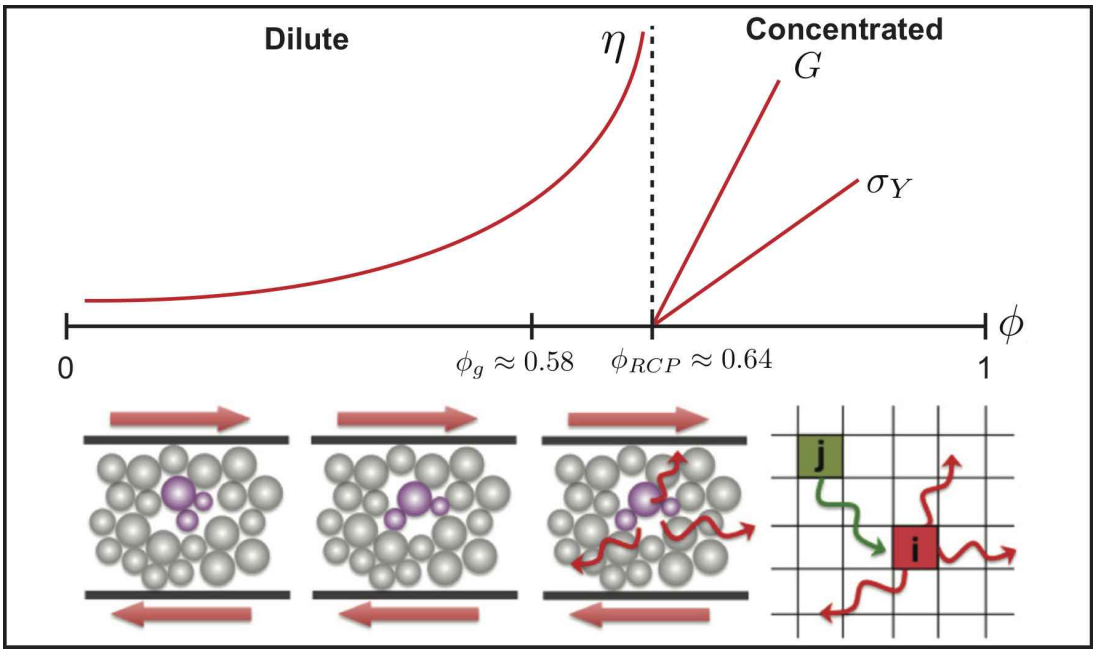

§ 3.1. Introduction

Soft glassy materials such as gels, foams, pastes, concentrated suspensions and emulsions have a remarkable number of rheological properties in common. They mostly exhibit a yield stress, i.e., they will not flow until a certain critical stress is exceeded. On the other hand, when exceeding this stress, all these systems show a strong shear thinning. This behavior, described by the Herschel-Bulkley model (introduced in section 1.3.3), shows strong similarities with glassy materials. The analogy between these soft materials and glassy materials is not limited to the rheological behavior. Concepts as: aging and shear rejuvenation are strongly shared within these two categories. Because of this deep analogies, one classifies all the above systems as "Soft Glassy Materials".
Another properties that characterized SGMs is the "jammed" configurations of the constituting elements. This corresponds to states below the glass transition temperature for glassy systems. The concept of jamming is widely used to describe blocked system from traffic to cells. Liu and coworkers [95] proposed a speculative phase diagram for jammed soft material. This diagram is dependent on three variable: temperature, density and load. As reported in fig. 3.1 the system is considered blocked if density is high enough. On the contrary, the passage form blocked system to a "fluid state" can be obtained either by and increasing the temperature or the applied stress.

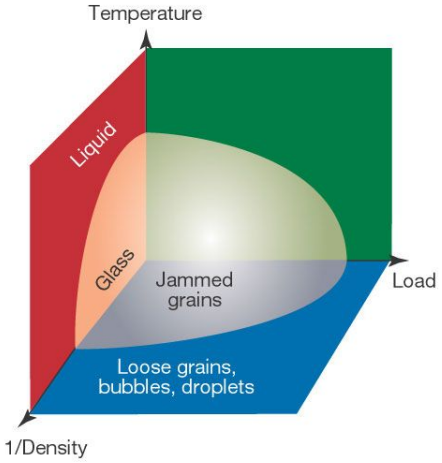

Figure 3.1: Phase diagram proposed by Liu *et al.* accordingly to reference [95]. The jammed state, located close to the origin, is represent by curved surface.

§ 3.2. Dense Emulsion

In this work we used a dense emulsion as model of Soft Glassy Material. An emulsions is defined as a mixture of two immiscible liquids. They are involved with many engineering operations and form many useful products. This includes emulsion-based food products, such as homogenized milk, sauces (mayonnaise, vinaigrette), dressings, beverages, butter, pharmaceutical products

in the form of creams and balms. Emulsions are also used in cosmetics, personal hygiene products, fire-fighting agents, agricultural industry products, paints and inks. Simple emulsions are categorized by the nature of the suspended phase to the continuous (see fig. 3.2); oil-in-water (O/W) emulsions are *direct*, while water-in-oil (W/O) are commonly described as *invert* [96].

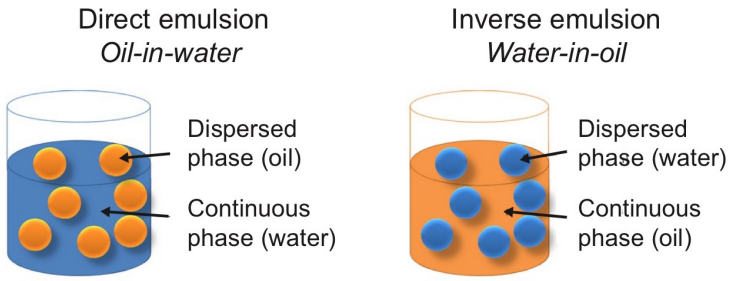

Figure 3.2: Representation of a *direct* oil-in-water and *inverse* water-in-oil emulsions.

Emulsion preparation requires a substantial input of energy and aims to create surface between the two fluids. The results is a metastable system which tends to return to its thermodynamically stable state with the two liquids unmixed. The emulsion instability can be mitigated with the use of amphiphilic molecules called surfactants or emulsifier. They play two crucial roles: first they lower surface tension γ between the two fluids reducing the work necessary to create droplets. Second, they coat the outside of the droplets. Once the droplets have formed, the surfactant acts as a physical barrier between the different phases of the system. The surfactant isolates individual droplets from the continuous phase and from each other. For this barrier to be effective, a minimal amount of surfactant, enough to coat every particle in the systems, needs to be on available. The stabilization induced by surfactant allows to increase the emulsion lifetime of a few day to a few year. One must choose a surfactant that is more soluble in the continuous phase than in the dispersed one to obtain a stable emulsion [97]. The continuous phase is not always the phase that has the highest volume. In contrast to granular matter, very high volume fractions of particles (more than 99,95%) may be reached in emulsion systems because the droplets are soft and may be deformed. Emulsions are characterized by the size distribution and volume fraction of the droplets of the dispersed phase. The volume fraction is given by the ratio of the volume of the dispersed phase to the volume of the entire emulsion. Typical values for the droplet size range between 500 nm and a few hundreds of microns [98–100].

§ 3.2.1. Emulsion stability

As introduced in section 3.2, surfactants play an important role in the rheological behavior of emulsions at any concentration. Aggregation stability of droplets is determined mainly by the nature and concentration of a surfactant in the system creating and stabilizing the emulsion. Thermodynamically, a surfactant is adsorbed at internal interfaces and decreases the interfacial tension. In some cases, it can result even in the formation of equilibrium colloid systems. Besides, the impact of stabilizing internal surfactant layers consists in providing repulsive forces (energetic

barrier) between droplets [96, 101]. The increase of the surfactant concentration up to a certain limit is favorable for the stability of an emulsion providing constancy of its properties with time. The specific nature of surfactants helps in deciding stability of emulsion; depending on their chemistry we can distinguish non-ionic, anionic, cationic or zwitterionic surfactants [96]. There are various processes that can break an emulsion: these are illustrated in fig. 3.3. The physical phenomena involved in each breakdown process are not simple, and they require detailed analysis of the various forces involved. In addition, these processes may take place simultaneously rather than consecutively and this complicates the evolution of the system. Let's briefly describe the principal breakdown processes.

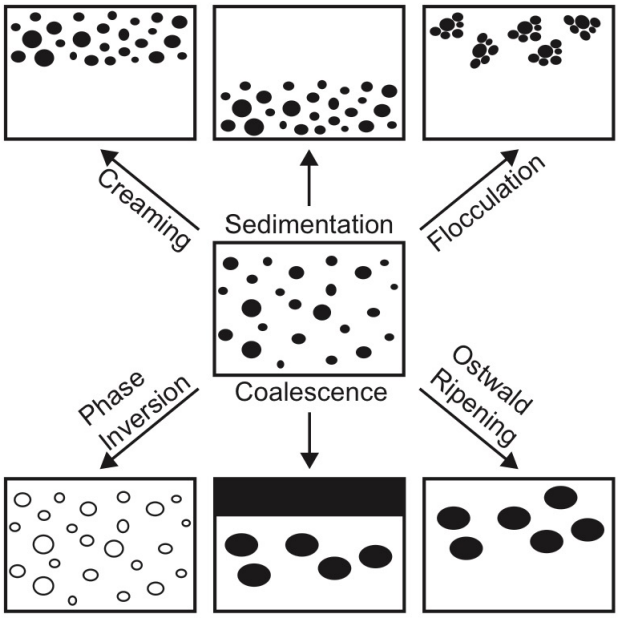

Figure 3.3: Schematic representation of possible breakdown processes in emulsion.

- *Creaming and Sedimentation.* This process results from the presence of external forces typically gravitational or centrifugal. When such forces exceed the thermal motion of the droplets (Brownian motion), a concentration gradient builds up in the system with the larger droplets moving faster to the top (if their density is lower than that of the medium) or to the bottom (if their density is larger than that of the medium) of the container.

- *Flocculation.* This process refers to aggregation of the droplets (without any change in primary droplet size) into larger units (cluster or aggregates). It is the result of the van der Waals attraction affecting all the dispersed systems. Flocculation occurs when there is not sufficient repulsion to keep the droplets apart to distances where the van der Waals attraction is weak enough to be neglected.

- *Ostwald Ripening.* This results from the finite solubility of the liquid phases. Liquids that are referred to as being immiscible often have mutual solubilities that are not negligible.

With emulsions, which are usually polydisperse, the smaller droplets will have larger solubility when compared with the larger ones (due to curvature effects). With time, the smaller droplets disappear and their molecules diffuse to the bulk and become deposited on the larger droplets. With time, the droplet size distribution shifts to larger values.

- *Coalescence.* This refers to the process of thinning and disruption of the liquid film between the droplets with the result of fusion of two or more droplets into larger ones. The limiting case for coalescence is the complete separation of the emulsion in two distinct liquid phases. The driving force for coalescence is the high surface energy due to the curvature of the drops.

- *Phase Inversion.* This refers to the process whereby an exchange between the disperse phase and the medium take places. Thus occurs when the volume fraction of the dispersed phase becomes higher than the continuous phase. For example, an O/W emulsion may with time or change of conditions invert to a W/O emulsion.

§ 3.2.2. Emulsion preparation

Depending on the properties of the emulsion (i.e., direct/inverse, droplets dimension, droplets size dispersion) and on the final application there are a large number of preparation methods. They can follow different approaches, but all of them have the same aim: create a stable surface between two components. A common way to distinguish the various preparation methods is to compare them on the base of the droplets size distribution.

- *Conventional equipment:* with conventional equipment it is possible to obtain emulsion with a size distribution generally higher than 30%. These process are based on the mechanical mixing of the components such as: colloidal mill, high speed blender or high pressure homogenizer [102, 103]. They can be used to prepare both direct or inverted emulsion with droplets size ranging from 0,1 to 50 μm. These processes are widely used in food or pharmaceutical industries because they are very efficient, stable, with a high throughput.

- *Membrane emulsificator (ME):* in this process, the dispersed phase is forced through the pores of a microporous membrane directly into the continuous phase. Emulsified droplets are formed and detached at the end of the pores with a drop-by-drop mechanism [104]. The advantages of ME are that it enables one to obtain very fine emulsions of controlled droplet sizes and narrow droplet size distributions around 10%. In the last years many industries started to use ME due to its operational flexibility, reproducibility, straightforward upscaling and low costs [105].

- *Microchannel Emulsificators (MCE):* In this process uniform droplets are generated by a microfluidic channel. Several configuration are suitable for this method: from the simple T-junction [106] to the more complex step emulsificator [107]. Major advantages of MCE include the generation of uniform emulsion droplets with highly narrow size distribution typically less than 5% and with a precise control of droplet size from 1 to 200 μm. MCE

are novel, versatile and very powerful techniques[105, 108]. Moreover, the scale-up these process can increase the productivity of monodispersed droplets (<100 L/h) and makes it a promising tool at industrial level.

§ 3.3. Soft Glassy Rheology

Emulsions exhibit highly varied rheological behavior that is useful and fascinating. An emulsion's macroscopic constitutive relationships between the stress and strain depend strongly on its composition, microscopic droplet structure, and interfacial interactions. By controlling the droplet volume fraction, an emulsion can be changed from a simple viscous liquid at low volume fraction ϕ to an elastic solid having a substantial shear modulus at high ϕ, as shown schematically in fig. 3.4. In the dilute regime at low ϕ, the droplets are spherical in the absence of shear. As ϕ is raised near the hard sphere glass transition volume fraction, $\phi_g = 0.58$, the droplets become transiently caged by their neighbors. As ϕ is further increased into the concentrated regime, the droplets randomly close pack at $\phi_{RCP} = 0.64$, and become compressed with deformed interfaces for larger ϕ. As $\phi \to 1$, the droplets become nearly polyhedral in shape and form a bi-liquid foam. Dilute emulsions behave as viscous liquids, whereas concentrated emulsions exhibit solid-like elasticity [6].

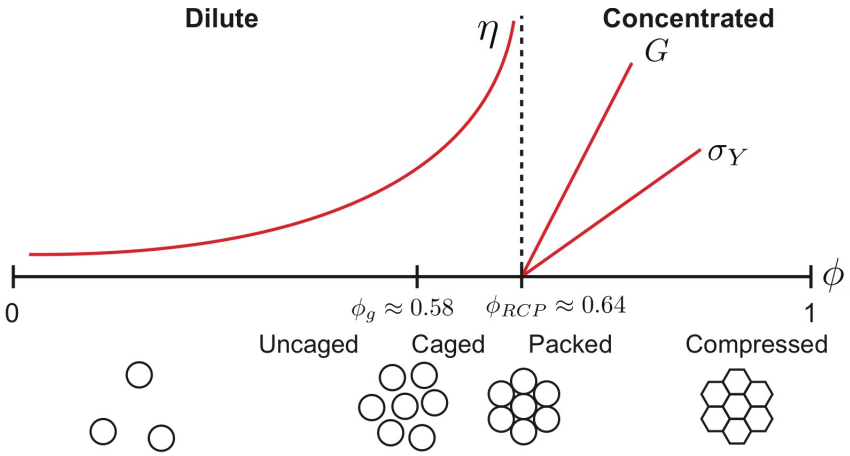

Figure 3.4: Schematic diagram of droplet positional structure and interfacial morphology for disordered monodisperse emulsions of repulsive droplets as a function of the volume fraction. The bottom part represents general peculiarities of rheological properties of emulsions for different volume fraction ϕ.

Figure 3.4 shows a scheme with the evolution of rheological properties of emulsions in the transition from dilute (at $\phi \ll 1$) to highly concentrated emulsions (in the domain $\phi > \phi_{RCP}$). Dilute emulsions behave like a Newtonian liquids with $\eta \sim$ const. In the second domain of intermediate concentrations, emulsions are liquids with weakly pronounced non-Newtonian behavior. Increasing ϕ in the domain of relatively high concentrations, non-Newtonian effect is strongly expressed and thixotropic and viscoelastic effects may be present. Above ϕ_{RCP} the emulsion behave like a viscoplastic materials with obvious yield behavior and wide frequency range of elasticity with constant shear modulus.

In a pioneeristic work, Princen studied the properties of concentrated emulsion flow with a two-dimensional hexagonal model [109]. He proposed a very simplified model which has been used as a stating point for more realistic description of these systems which are, generally, three dimensional and disordered. When the volume fraction of the emulsion (ϕ) increases, so that

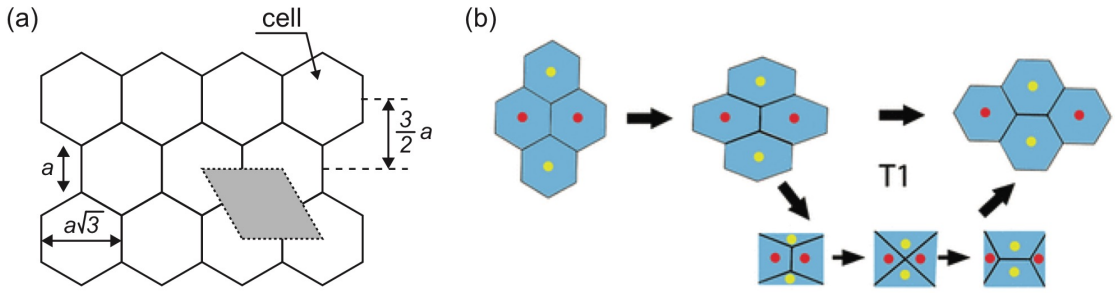

Figure 3.5: Diagram showing a hexagonal 2D lattice proposed by Princen to describe a concentrated emulsion [109]. Visualization of a plastic rearrangements T1.

$\phi > \phi_{RCP}$, the droplets are in contact one each other and start to deform their interfaces. The shape of the droplets is no longer spherical, as it was in the case of diluted emulsion. Therefore, their surfaces areas increase moving the system in a higher energy state. Applying an external deformation additional energy is stored and the interfaces between droplets. When the applied deformation is released, the stored energy is released an the droplets resume their initial form: the sample exhibited a classical elastic response. When the applied strain is sufficiently high, droplets change their neighbors with a structure rearrangements. The stored energy is dissipated and the results is the fluid flow. This example illustrates one of the main characteristic of emulsions: the existence of a yield stress. Above this threshold the emulsion flow like a liquid; the flow is characterized by a successions of reversible elastic deformation and irreversible plastic rearrangements associate with the yield stress. This mechanism was confirmed by Hébraud et al. [110], measuring the movements of the droplets in a concentrated emulsion using Dynamic Light Scattering (DLS) technique. He shown that for small deformation, some of the constituent particles moved with reversible events, while other rearranged irreversibly.
Rheological measurements can provide more information about this mechanism. In fact, the anomalous rheological behavior of the elastic modulus in non linear domain can be described by the presence of inhomogeneous distribution of rearrangements. From the rheological curves of storage modulus G' and loss modulus G" as a function of the applied stress is easy to estimate the Yield stress of an emulsion. An example of rheological curves, obtained by Mason *et al.*, are presented in fig. 3.6. At low shear rate, G' is grater than G" and they are both independent of the applied stress, and thy show a linear regime. When the applied shear increases G' remains constant, while G" increases its value. In this range of $\dot{\gamma}$ the emulsion droplets start to rearrange, causing an increase in the viscous dissipation of the system. These rearrangements are localized in few points of the emulsion and they are not sufficient to allow the emulsion to flow and the response of the system remains essentially elastic. At this stage, the number of droplets involved are less than 4% [110]. At higher shear rate, both storage and loss modulus decreases, with the

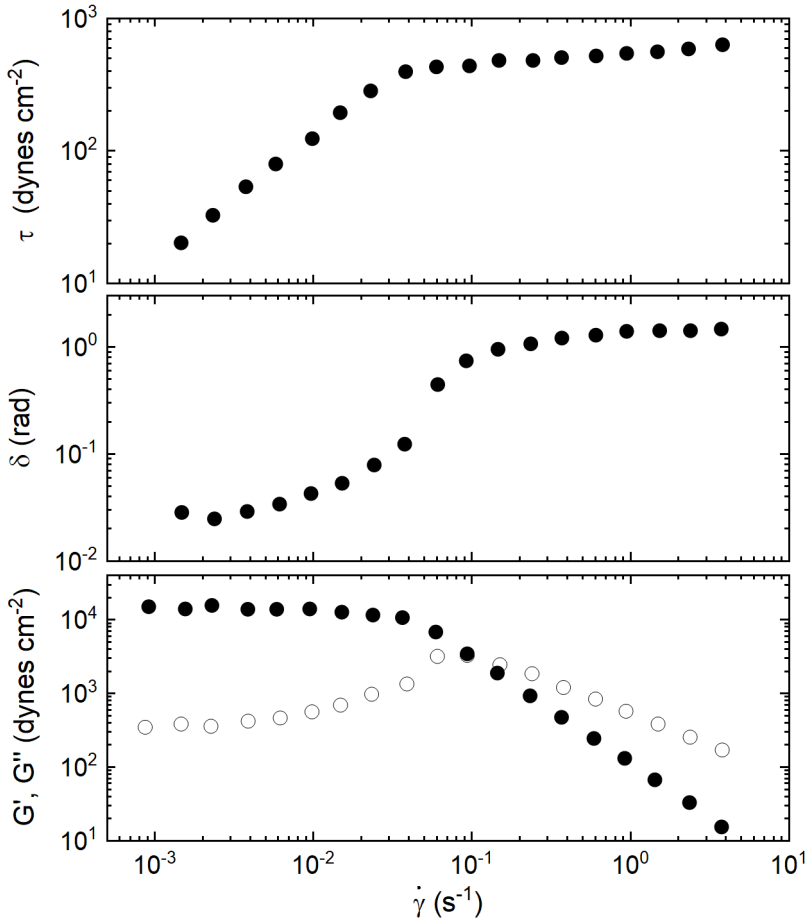

Figure 3.6: Rheology of a concentrated emulsion with a volume fraction of 0.7 and droplet radius d = 0.53 μm. Oscillatory shear was set at ω 1 rad/s. (a) Peak stress, τ (b) the phase lag, δ, and (c) the storage modulus, G', (solid circles) and loss modulus, G", (open circles) as a function of shear rate $\dot{\gamma}$ [111].

latter grater than the first one. In this regime, the number of plastic rearrangements is higher, they are distributed in all the system and the emulsion is flowing.

More recent studies confirm these behavior. For example, Schall *et al.* [112] visualized structural rearrangements in colloidal glasses in three dimensions and in real time by following the microscopic strain distribution under shear. The authors identify the shear transformation zones and show that they have a spatial extent of a few particle diameters and involve a highly localized structural rearrangement. The increase of the applied stress to the material extends the network of active regions throughout the sample.This study proposed, for the first time, the concept of cooperativity rearrangements.

§ 3.3.1. Shear banding

The flow of a concentrated emulsion shows an homogeneous flow for an homogeneous stress. If the stress is not homogeneous, one may have shear localization. The shear stress is zero in

regions where the local stress is below the yield stress and non zero in other regions of the system. Local velocity measurements have shown that another class of fluids present a more exotic behavior called shear banding or viscosity bifurcation. In particular, shear banding refers to the notion of strain rate localization. When a fluid material is sheared, the strain rate can take large values in narrow zones of the sample. In the presence of these region a Yield stress fluids can show an inhomogeneous flow due to different degrees of fluidization.
Such behavior has been observed in adhesive emulsion [113, 114], hard-spheres suspension [115], clay suspension [116], worm-like micelles [117] and star polymer [118, 119]. The flow curve can be schematically represented as in fig. 3.7b. It exists a gap in shear rate where the flow is unstable. If one imposes a shear rate in this unstable gap the system will split in a flowing and a solid-like bands. Experiment on emulsion [113, 114] have shown that introducing attractive interactions creates shear banding. Thixotropy seems to be also often present in shear banding fluids [113, 114, 119]. In fig. 3.7c are reported an experimental image showing the shear banding effect.

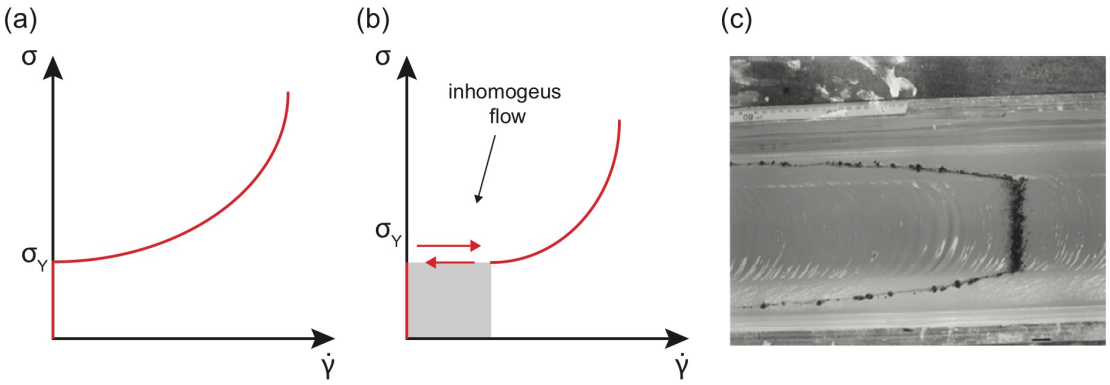

Figure 3.7: Schematic representation of the different laws that describe the behavior of an emulsion (a) Herschel-Bulkley, (b) solid-liquid discontinuous transition between a state and a non sheared fluid branch. The gray region indicates the region of inhomogeneous flow. (c) View of the top free surface of a kaolin suspension flowing in steady-state. Slight "dunes" at the free surface were formed far shear localization close to the walls and a central undeformed plug region. Reprinted figure from Coussot *et al.* [116]

§ 3.3.2. Dense emulsion flow

A comprehensive study of monodisperse emulsion flowing in a Couette cell was first gave by Mason *et al.* [111]. The flow curves measured show that for $\phi_{eff} > \phi_{RCP}$ (with ϕ_{RCP}, the random close packing volume fraction), the shear stress tends toward a non-zero value for a vanishing shear rate. ϕ_{eff} takes into account the deformation of the droplet interfaces as they are forced together. The repulsive interaction is represented crudely by a forbidden zone of penetration. When droplets are strained, their interfaces deform, and their surface increases. The energy stored during this deformation provides the elastic modulus and yield stress of the

material. Mason *et al.* showed that the yield stress, σ_Y, scales as

$$\sigma_0 \propto (\gamma/a)\phi_{eff}(\phi_{eff} - \phi^2_{RCP}) \tag{3.1}$$

with γ the surface tension (see fig. 3.8b). Beyond the yield regime, the flow curve follows a Herschel-Bulkley law. The stress varies as $\sigma/\sigma_0 - 1 \propto \dot{\gamma}^n$ $n = 0.5$. We note that emulsions with a volume fraction lower than ϕ_{RCP} display a simple shear thinning behavior without threshold value.

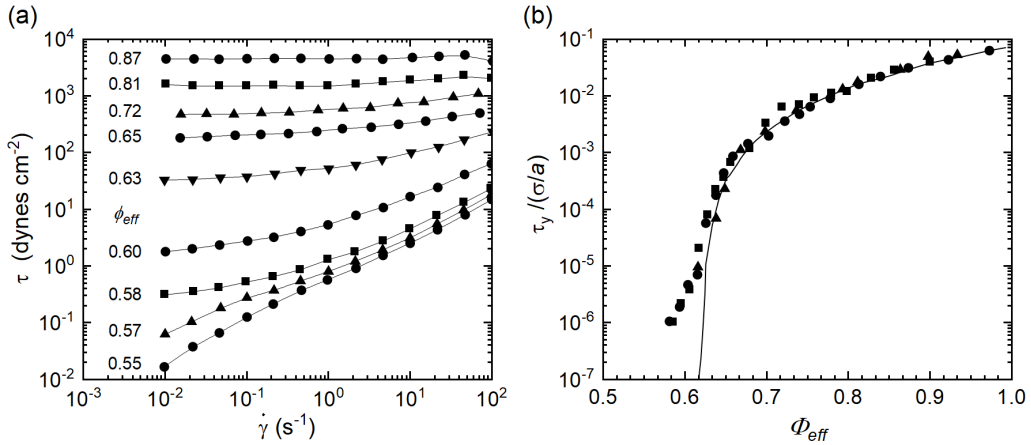

Figure 3.8: (a) Flow curve of an emulsion at different volume fractions. (b) Yield stress of an emulsion as a function of the volume fraction. Emulsions are monodisperse with radii 0.25, 0.37, 0.53, 0.74 μm. Reprinted figure from Mason *et al.* 1996 [111]

A few years later, it has been tested the link between the complex microscopic behavior and macroscopic features of the emulsion flow: the velocity of wall slip [5, 11]. Goyon and coworkers compared the flow of dense emulsion in two different geometries showing (see fig. 3.9a, b) that under confinement, the relation between the local stress and the and the local shear rate cannot be reconciled with a single master curves [11]. Such non-locality has been later confirmed for other SGM, such as foams [120] and Carbopol gels [121], suggesting common scenarios for the fluidization of SGM in confined microchannel. With the help of numerical simulation, it has been confirmed that such non-locality is connected to plastic rearrangements of material constituents [5, 20, 122]. These, in turn, are related to topological changes in the droplets configurations which take place local elastic deformations cannot be sustained anymore and yielding events relax the accumulates stress. This phenomenology has constituted the core of many theoretical works which have been put forward in the recent years to account for the non-local effects [16, 123–125].

One of them, the Kinetic Elasto-Plastic (KEP) model [123], describes such scenario using a kinetic description for the elastoplastic properties of a jammed material. Briefly, the KEP model describes the non-local effects using a diffusion-relaxation equation for the "fluidity" field $f = 1/\eta = \dot{\gamma}/\sigma$, in which is present a characteristic length-scale ξ. The so-called "cooperativity length", measures the spatial extension of the non-local correlations. Another important result

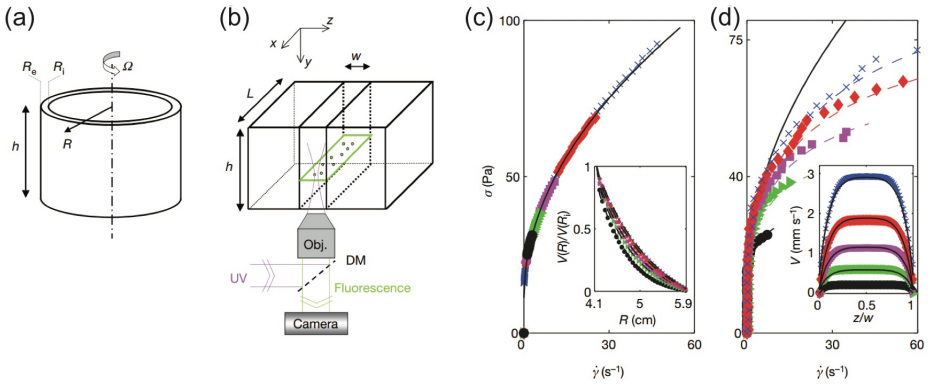

Figure 3.9: Schematic representation of the wide gap Couette cell (a) and microfluidic channel (b). (c) and (d) are the local flow curves extracted from the measurements of the velocity profiles in both geometries for an emulsion with volume fraction $\phi = 0.75$. Pictures and data are reproduced from Goyon *et al.* [11].

of KEP is the connection between the fluidity field with the rate of plastic rearrangements Γ, $\Gamma \propto \mathcal{A}f$, with $\mathcal{A}$ a constant, proportional to the elastic modulus of the material. A detailed description of the model is described in section 3.4.

Apart from a few exceptions (mostly numerical studies [126, 127]), the relation between the rate of plastic rearrangements and the flow profiles has been rarely tested. This is important especially close to the walls, where the the surface properties (i.e., roughness and/or wetting) can trigger droplets rearrangements. In that case these rearrangements increase the wall fluidity f_w, which ultimately affects the bulk properties over a distance determined by the cooperativity length scale ξ. The wall fluidity usually enters the picture as a free input parameter, and so far only a limited number of studies [19, 20, 128] provided insights into the specific role of the walls. Mansard *et al.* [19] analyzed the flow of concentrated emulsions in micro-channels with rough walls patterned with pillars of different heights, finding that slip and wall fluidization depend non-monotonously on the height of the rough elements. The non-monotonous behavior was explained in terms of an interplay between the (wall) yield stress and the plastic rearrangement time scale. For sufficiently large height, roughness was shown to provide enhanced fluidity close to the walls, a fact that was explained in terms of an "activation" of plastic rearrangements. Such activation picture was also supported recently by another study by Paredes *et al.* [20]: the authors showed that by controlling the wetting properties of the confining walls, the characteristic cooperativity length could be understood in terms of the activation of plastic rearrangements triggered by the "soft" roughness induced by adsorbed droplets on the wall.

§ 3.4. Models of Soft Glassy Rheology

The theoretical description of these materials is a challenging task for statistical physics. In literature, several authors proposed detailed models to describe the dynamics and the flowing mechanism of SGMs [20, 126, 129, 130]. All the proposed models follow the same approach: describe the dynamic in an intermediate level between the microscopic scale (i.e., individual

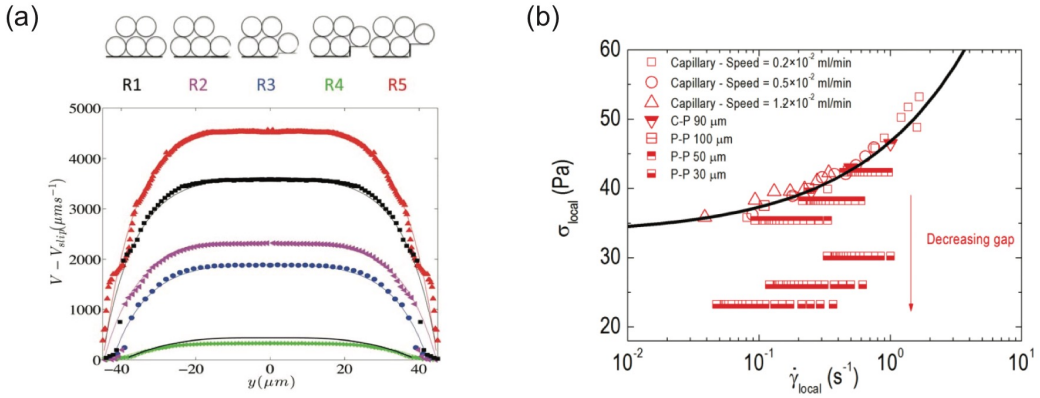

Figure 3.10: (a) Velocity profile for various roughness sizes depicted above [19]. (b) Microscopic flow curves obtained from the velocity profiles using a hydrophobic microchannel and hydrophobic plates-plates rheometer. The black line is the fit of collapsing curves to the Herschel-Bulkley model used as a reference [20].

droplets) and the macroscopic scale. In the following discussion, we will briefly present two different approaches that address this problem: Soft Glassy Rheology (SGR) and the Kinetic elasto-plastic (KEP) model.

§ 3.4.1. The Soft Glassy Rheology Model

The Soft Glassy Rheology model (SRG) is a scalar phenomenological model, inspired by the model of Bouchard [129]. It was presented by Sollich and coworkers [130, 131] to describe system with a structural disorder (concentrated emulsion/suspensions or foams) and in non-equilibrium state. The material is coarse grained into a collection of mesoscopic subsystems. The large number of these subsystems allows to describe the behavior of the entire system as the average of the elements that compose it. SGR was originally a scalar model, but a tensorial description has been proposed by Cates [132]. Only a single shear component of each of the strain and stress tensors is considered; these components will be denoted by $\dot{\gamma}$ and σ. In the system, constituent particles (i.e., droplets or bubbles) are spotted inside a cage formed by the adjacent particles. They can get out of these cages under the influence of two factors: an elastic deformation or by an interaction with another moving particle. In the case of an emulsion the energy barrier, associated with the rearrangements, is significantly higher than the thermal energy k_bT. This energy barrier can be crossed by the elastic energy (due to the applied shear) or by an interaction (a rearrangement that occurs in a specific place can spread and causes another rearrangement in the sample). In the model the state of the system at the time t is described by the probability P that have a local strain l and a barrier E . The probability $P(E, l, t)$ evolves in time according to two distinct mechanisms: the homogeneous shearing at a rate $\dot{\gamma}$ and the yielding of elements at a rate of $\Gamma(E, l, t)$ per unit of time. Thus, the master equation for $P(E, l, t)$ is the following:

$$\frac{\partial P}{\partial t} = -\dot{\gamma}\frac{\partial P}{\partial t} - \Gamma_0 e^{-(E-1/2kl_2)/x} P + \omega(t)\delta(l)\rho(E) \tag{3.2}$$

the first term describes the elastic deformation of the regions; the second describes how rear-

rangement, which occurred at a specific place in the material, may affect another region. x is defined as "activation thermal noise". The last term describes the relaxation region where the rearrangement occurred. For $x < 1$ the model predicts the existence of a yield stress.

§ 3.4.2. KEP model

Bocquet *et al.* [123] have recently used a kinetic elasto-plastic model to derive a non-local constitutive law for the flow by coarse graining the microscopic spatio-temporal dynamics. In the KEP model the sample is divided into elementary blocks of size a (typically the size of individual particles) carrying a scalar shear stress σ, and the system is described in terms of the block stress distribution $P(\sigma, t)$. At a given position, the stress evolves by three channels: an elastic response under an externally imposed shear rate $\dot{\gamma}$, a stress relaxation because of local plastic events and a modification of the stress caused by plastic events occurring in other blocks. The stress release after plastic events is transmitted spatially in the material via elastic interactions.

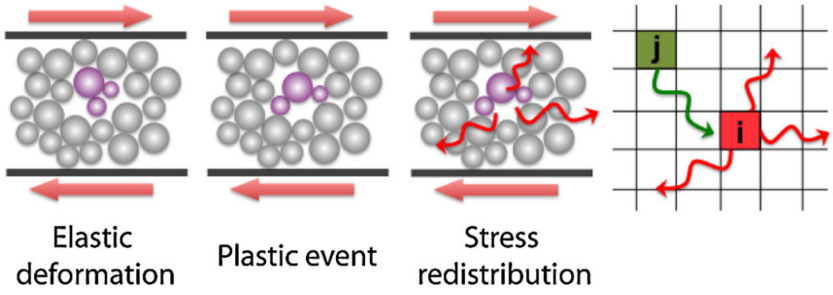

Figure 3.11: Sketch of plastic deformation in amorphous media. Deformation occurs via elastic deformation, localized plastic events, and nonlocal redistribution of the elastic stress, potentially triggering other plastic events. Image is reproduced from [123].

The authors introduced a new equation that link the local shear rate, the local shear stress and the number of plastic events per unit of time (i.e., the fluidity f)

$$\Gamma \propto f = \dot{\gamma}/\sigma \tag{3.3}$$

Moreover, for spatial heterogeneous flow, using a non-local equation, the authors showed that the fluidity obeys to a non-local equation as experimentally found by Goyon *et al.* [11]

$$\xi^2 \frac{\delta^2 f}{\delta^2 z} + (f_{bulk} - f) = 0 \tag{3.4}$$

where ξ is the length-characterizing flow cooperativity and f_{bulk} is the bulk fluidity (i.e., the

value of the fluidity without spatial heterogeneity)

$$\begin{aligned} for \qquad & \sigma > \sigma_0 \qquad f_{bulk} = \frac{1}{\dot{\gamma}} \left(\frac{\sigma - \sigma_0}{A} \right)^2 \\ for \qquad & \sigma < \sigma \qquad f_{bulk} = 0 \end{aligned} \tag{3.5}$$

f_{bulk} only depends upon the local shear stress, while f depends upon the position in space. Its value is equal to f_{bulk} when the shear stress and the shear rate are constant in an infinite geometry. To solve this set of equations and obtain the shear rate field, two boundary conditions on the fluidity are required. Knowledge of the velocity field will require an additional set of boundary conditions on the slip velocity v_s. This set of equations introduces non-local effects for the fluidity field and, consequently, for the velocity field. Physically, the length ξ that characterizes these heterogeneities quantifies the spatial spreading of the plastic activity as a result of the non-local elastic relaxation over the system. This characteristic length is only function of the volume fraction of the emulsion [11, 20, 133].

4. Microfabrication

Microfluidic technology aims at the miniaturization of conventional laboratory process to handle liquid at the microscale. In the last two decades lab-on-chip devices have been extensively studied and developed so as the microfabrication technology to realize them. Since the technology for developing these devices was initially adapted from conventional semiconductor and microelectronic industry, now there are plenty of other techniques and materials that can be used to fabricate microfluidic devices. This Chapter describes the most common microfabrication techniques used in microfluidic technology and it is organized as follow: in section 4.1 replication based and machining based techniques are reviewed. Then, in section 4.2, the discussion is focused on standard photolithographic technique. In section 4.3 an evolution of photolithography, called multi layer photolithography is described in more detail. Section 4.4 and 4.5 describes the properties and main features of the photoresist used in this work and, as last, section 4.6 explains the reasons to work in a dedicated environment to realize microfluidic devices.

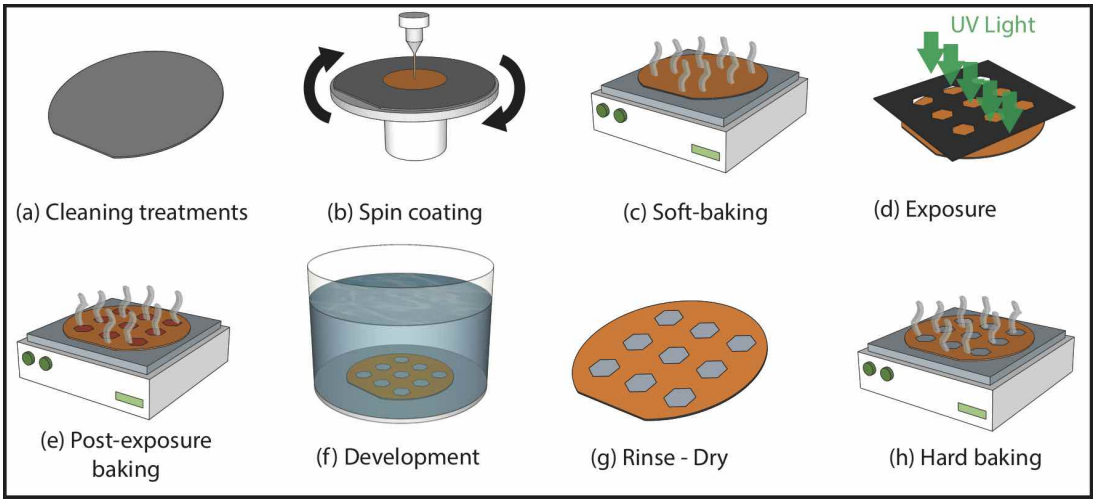

Introduction

Microfabrication technologies originate from the microelectronics industry, but now are widely used in many technological and industrial fields [134, 135]. They can be broadly classify into three types: i) replication based, ii) machining based process and iii) photolithography based. In the replication methods, a master mold is replicated using a thermoplastic of photocurable polymer. In this category are included Soft-lithography, Hot Embossing and Injection molding [136]. In the second category, a microdevices are fabricated using evolution of machining technique such as: micro milling, laser ablation, and recently additive manufacturing [137]. In photolithographic microfabrication, light is used to define patterns on a photosensitive material [134]. The choice of the fabrication method depends on various factors such as: the chemical/physical compatibility, features size, speed, quantity, and cost.

§ 4.1. Microfabrication techniques

Even if photolithography is the most diffused microfabrication techniques, it has some disadvantages. The size of the features are limited by optical diffraction and to obtain sub-micrometric or three dimensional structures are required complex facilities. It is a quite expensive technique and only few types of materials can be used. In addition, there is not a good control of the surface chemistry and this could be a problem for chemical and biological applications. For all these reasons, during these years others microfabrication techniques have been developed. In this section machining based and replica based techniques are briefly reviewed.

§ 4.1.1. Soft-lithography

Soft-lithography consists of non-photolithographic methods to transfer a geometrical pattern from a mold to a "soft" material, i.e., polymeric material [136]. The most notable polymer is the polydimetylsiloxane, commonly known as PDMS.
With respect to photolithography, soft-lithographic techniques involve simpler procedures and equipment, usually do not require a clean room and the typical materials used are cheaper. Nevertheless, soft-lithography allows high quality and high reproducibility fabrication of micro- and nano-structures. Some of the disadvantages of PDMS based soft-lithography include: shrinkage during curing, swelling by non-polar solvents and the softness of the material limits the achievable aspect ratio through sagging. The different techniques which are included in the soft-lithographic family are: replica molding (REM), microcontact printing (μ-CP) and microtransfer molding (μ-TM) [134].

Replica molding: replica molding (REM) allows to realize a negative copy of a initial master. Unlike the standard strategies to make a mold, in this case an elastomeric polymer is used, which can be easily removed from the master: the prepolymer is poured on a master and, after the curing time is peeled of as shown in fig. 4.1a. As a matter of fact, it allows to reproduce very complex (two or three dimensions) and resolute (nanometric scale) structures in one single

step [51].

Microcontact printing: In microcontact printing (μ-CP), a PDMS rubber stamp is coated with an ink of the molecules that one wants to print in selected patterns on a solid substrate. During stamping, only the raised parts of the stamp collect the ink that is transferred only by contact between the mold and the substrate. The deformability of the elastomeric stamp allows it to accommodate rough or rounded surfaces such as optical fibers or lenses. In fig. 4.1b we illustrate a generalized scheme for microcontact printing.

Microtransfer molding: In μ-TM the rubber mold (commonly PDMS) is filled with a polymer precursor. The polymer in excess is removed and the rubber stamp is then pushed up against a substrate (e.g., a Si wafer or glass) [138]. The polymer in the rubber stamp relief is cured and transferred to the substrate, and the stamp is peeled off. After the peel off the cured polymer remains on the substrate as shown in fig. 4.1c.

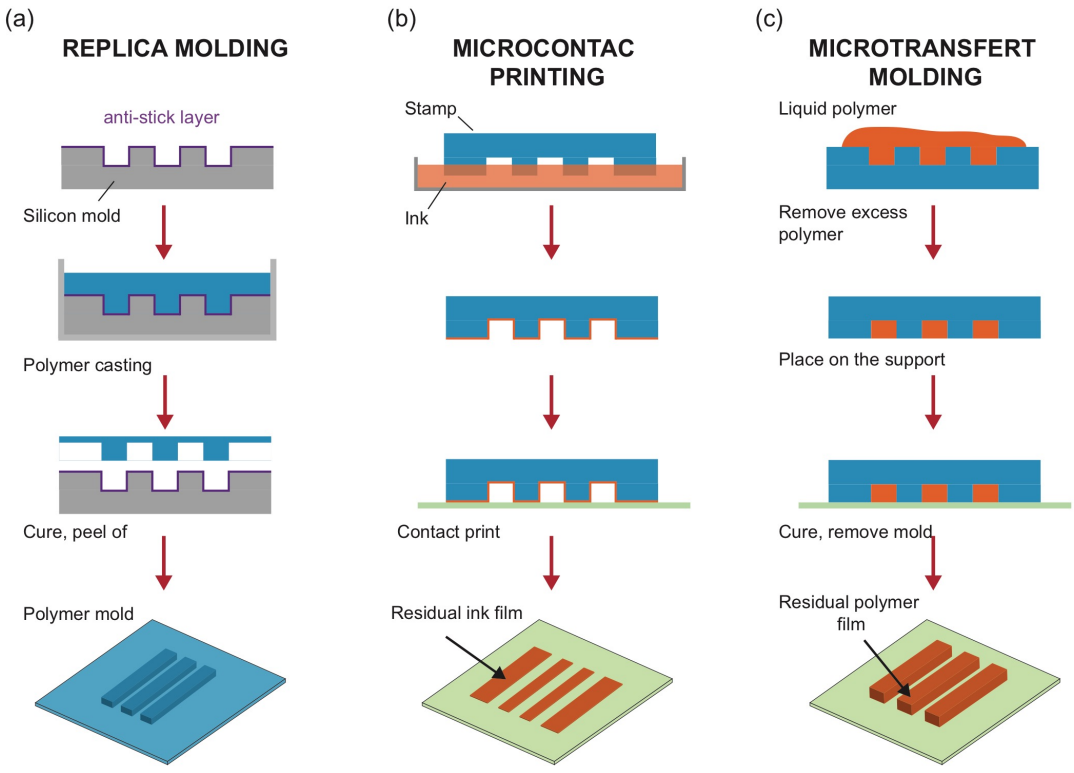

Figure 4.1: Schematic representation of soft lithographic techniques: (a) replica molding, (b) microcontact printing and (c) microtransfer molding.

§ 4.1.2. Micro-milling

Micro-milling is an alternative method that has the potential to address some of the challenges in microfabrication. The technique is characterized by the mechanical interaction of a sharp tool

with the workpiece material, causing the breakage inside the material along defined path, and eventually leading to removal of the useless part of the workpiece in the form of a chip [139]. Even though this technique cannot be capable of obtaining as small feature sizes as in lithographic processes, it is important in order to bridge the macro domain and the nano/micro domains for making functional components [140, 141]. Micro-milling has the capability of free form machining of complex 3D shapes from a wide variety and combination of traditional and well-understood engineering materials such as alloys, composites, polymers, glasses and ceramics. In the last ten years micro-milling spreads in many application fields: from biomedical to aerospace including information technology and telecommunication. Recent work has also shown Micro-milling to be effective for microfluidic devices[142, 143]. Respect to multilayer photolithography, micro-milling can achieve complex three dimensional features such as undercuts, rounded surfaces, and sharp internal corners by using appropriate tooling.

§ 4.1.3. Additive Manufacturing

Additive manufacturing, also referred to as 3D printing, has emerged as a flexible multi-material processing technique and enables the design and manufacture of novel functional materials and devices. This technique builds up the structure by adding successive joined layers of material one onto the other as opposed to removing material subtractively from a larger block (e.g. milling) [144]. 3D printing technologies are able to use a wide range of materials such as resins, thermoplastic polymers, photopolymers, biopolymers, preceramics and metals. In the last few years additive manufacturing, for microfluidic devices fabrication, became an interesting research topic, although much has yet to be done to develop specific solutions. Indeed, with respect to photolithography or machining based techniques, the spatial resolution is limited, on the order of hundreds of microns.

§ 4.2. Photolithography

The word lithography (Greek for the words stone [*lithos*] and to write [*gráphein*]) refers to a process invented in 1796 by Aloys Senefelder. Senefelder found that stone (he used Bavarian limestone) when properly inked and treated with chemicals could transfer a carved image onto paper. The most widely used form of lithography is photolithography. In this process, a pattern is transferred to a photosensitive polymer (a photoresist) by exposure to a light source through an optical mask. An optical mask usually consists of opaque patterns on a transparent support used to define features on a wafer. The pattern in the photoresist can be then further transferred to the underlying substrate by subtractive (etching) or additive (deposition) methods. In microfluidics this technique is commonly used to obtain simple or intricate devices [145].
There are several implementation of the photolithographic process with specific requirements, but there is a basic common flow of process that are common to most procedures. In this section, we introduce the basic lithography steps of preparation of substrate, resist application, exposure and development (see fig. 4.2).

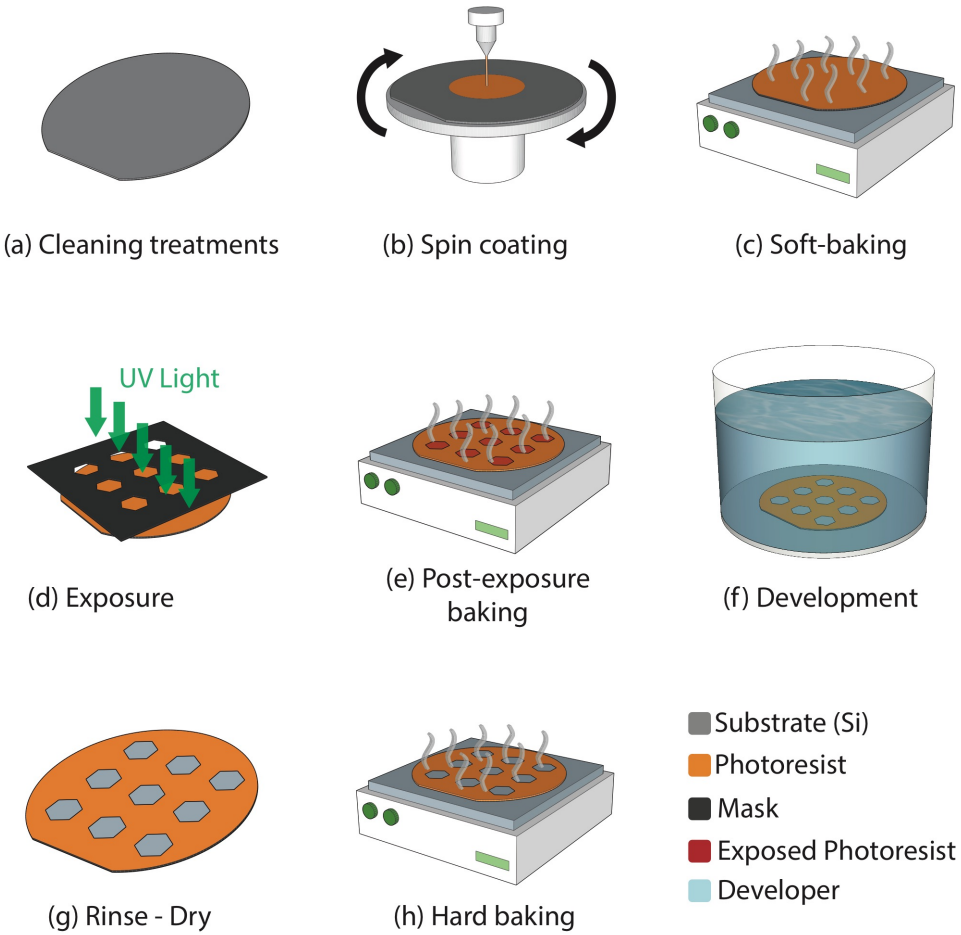

Figure 4.2: Sketches of photolithographic steps; (a) Cleaning of the substrate, (b) Resist deposition by spin coating, (c) Soft-baking, (d) Photoresist exposure, (e) Post-exposure baking, (f) Photoresist development, (g) Rinse of the sample and (h) Hard baking.

Preparation of substrate

Substrate cleaning is the first and a very important step in any lithographic process because the presence of impurities or residual coatings can compromise the adhesion or the quality of the coating. We can distinguish two main categories of contaminants:

- Physical: dust particles can hinder the lithography process by preventing light from exposing the photoresist or by disturbing the surface uniformity of a coated photoresist.
- Chemical: contaminants may react with various materials used in the lithography process, creating unwanted effects.

Usually, new substrates do not need cleaning, because they are cleaned before shipping and are kept in a contamination-free container. If cleaning of the substrate is necessary, a variety of methods (HF dip, use of piranha, plasma cleaning, and so on) can be used to remove different types of contaminants. The presence of water or water vapor compromises the adhesion between the photoresist and the wafer. Before the photoresist is applied, a dehydration bake is performed

(placing the substrate in a hotplate at ∼200°C) to remove water from the surface of the wafer.

Resist Deposition

In the second step of the lithographic process, a thin layer of an organic polymer sensitive to light radiation (from ultraviolet to X-Ray) or electrons rays, called photoresist (PR) is deposited on the substrate. We can distinguish two kind of PR: liquid and Dry Film resist (DFR). The liquid photoresist is dispensed onto a wafer that is held by a vacuum chuck in a spin coater. The wafer is then spun in one or more steps at precisely controlled speeds. The spin speed (between 1500 and 8000 rpm) allows the formation of a uniform film. At these speeds, the centrifugal force causes the liquid spreading to the edges, where the excess is expelled. The coating layer thickness t is, in good approximation, equal to: $t \sim \left(\frac{\eta}{\rho\omega^2}\right)^{1/2}$ where η is the fluid viscosity, ρ is the fluid density and ω is the angular velocity during the spin coating process [146].
The DFR are deposited to the substrate using lamination technique; a detailed description of DFR is reported in section 4.5.

Soft Bake

After spin coating, the liquid resist still contains up to 15% solvent and may contain residual stresses. The wafers are therefore soft baked at 75°C - 100°C to remove solvents, stress, and to promote adhesion of the resist layer to the wafer.

Exposure

The exposure is the key step of photolithography; the pattern is transferred onto a photoresist by shining light through a mask (see fig. 4.2d). As a light source one typically uses the g-line (435 nm) or i-line (365 nm) of a mercury lamp, but a wide range of wavelength can be used depending on the photoresist absorption. The action of light on a photoresist either increases or decreases the resist solubility depending on whether it is a positive or negative photoresist, respectively. Thus, for a positive tone photoresist (for example the Microposit®), the opaque pattern on the mask will determine the features remaining in the resist layer after development (see fig. 4.3). Conversely, after development of a negative photoresist (or example the SU-8)the clear pattern of the mask determines the remaining photoresist features. Usually, after the exposure step it is possible to observe a latent image of the mask on the surface of the photoresist. During the exposure step, the quality of the mask plays a crucial role. To obtain the best resolution, the masks are usually composed by a quartz plate which is transparent to deep UV, covered with an adsorber metal pattern, normally a chromium layer of tens nanometer. If it is not necessary to achieve high resolutions, it is possible to use a dark pattern printed by high resolution laser printers on a standard transparent acetate sheet. There are different methods for interfacing the photoresist film with the mask: i) contact printing, ii) proximity printing and iii) projection printing [145]. In the first case the mask and the resist are put into contact, while in the second case a gap of about 10 -50 μm is left between the two surfaces. Projection printing uses optics to demagnify images: in this case the feature resolution on the imaged wafer can be

even finer than the resolution of the mask.
Using both contact and proximity arrangements of mask and substrate, the resolution limit depends on various factors. These include the diffraction of the light at the edge of an opaque feature, the alignment of substrate respect to the mask, the not perfect flatness of the resist film and the dirty particles between mask and substrate. If we consider a periodic grating made of opaque and transparent stripes of equal width, b (see fig. 4.3a), the theoretical resolution R, is given by

$$R = b_{min} = \frac{3}{2}\sqrt{\lambda(s + \frac{z}{2})} \tag{4.1}$$

Where b_{min} is the minimum feature size transferable, s is the gap between the mask and the photoresist, λ is the radiation wavelength and z is the photoresist thickness. From this equation it is possible to observe that, smaller is the wavelength and the thickness of the film, higher is the possible resolution and that the contact printing, where $s = 0$, should give higher resolution than the proximity printing. However, as the contact between the polymer and the mask could cause mask damage or contamination, sometimes it is better to avoid working in contact mode.

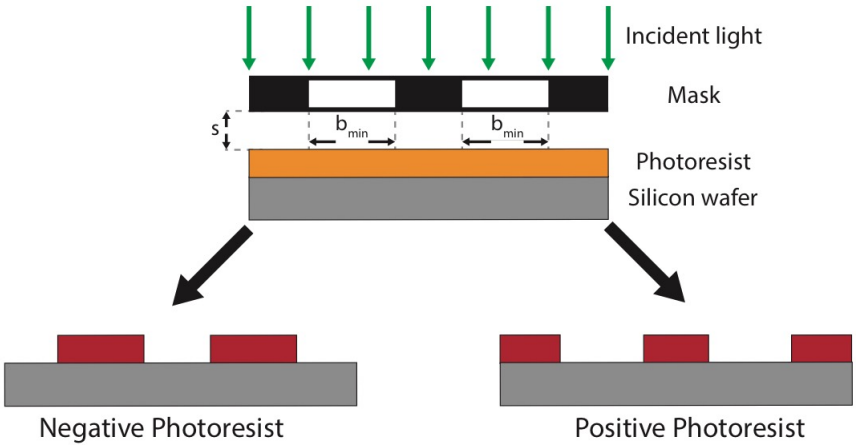

Figure 4.3: Top: side view of exposure process. Bottom: different outcomes of UV light exposure for positive and negative resists.

Post Exposure Treatment

A post-exposure bake step is conduced to further harden the insoluble region of photoresist, making it more resistant. The baking procedure is dependent on the photoresist formulation and thickness. Usually, the substrate is slowly cooled down to prevent the formation of cracks due to thermal stresses.

Development and Post Baking

During the development process, selective dissolving of resist takes place (see fig. 4.2f, g). De-

velopment is commonly done using a liquid (wet development), but a gas, or plasma can be used. Positive resists are typically developed in aqueous alkaline solutions, and negative resists in organic solvents. Post baking (or hard baking) removes residual solvents and anneals the film to promote interfacial adhesion of the resist that has been weakened either by developer penetration along the resist/substrate interface or by swelling of the resist. Hard baking also improves the hardness of the film. Improved hardness increases the resistance of the resist to subsequent etching and deposition steps. Post baking is usually done at higher temperatures (120°C) and for longer times (e.g., 20 min) than soft baking or post-exposure baking.

§ 4.3. Multilayer photolithography

Modern microfluidic devices can incorporate channel of different heights to fulfill their designed function [147, 148]. While the fabrication of a master with three dimensional features, is quite easy using machining based process with photolithography is also possible, but with a more complex and time expensive procedure. Multilayer lithography consists in the repetition of a separate set of photolithographic steps, including photoresist deposition, photomask alignment, exposure, and bakes, followed by a development step to realize a 2.5D master [134]. Another way to realize structures with different height on the same wafer is the gray tone lithography [149]

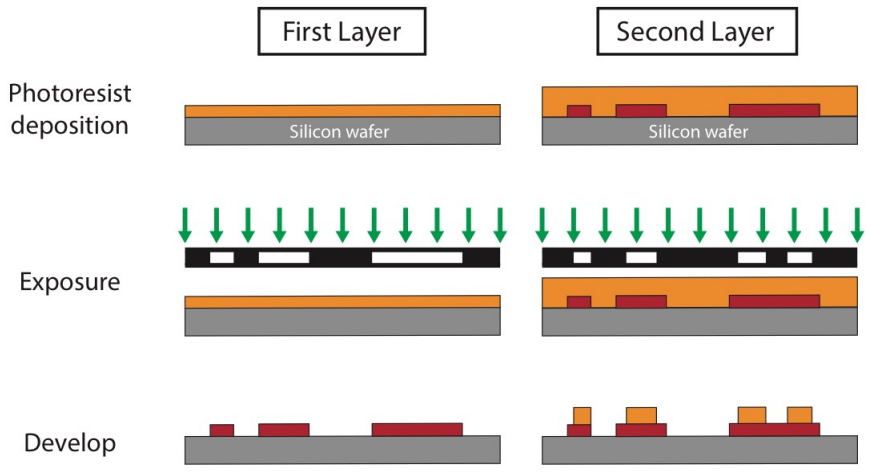

Figure 4.4: Schematic drawing of two-step lithography process to fabricate multilevel microchannels for negative photoresist.

In order to make useful devices [18, 150], the patterns from different photolithographic step must be aligned to one another. The first pattern transferred to a wafer usually includes a set of alignment marks (see fig. 4.5a, b), which are high precision features that are used as the reference when positioning the second pattern, to the first pattern. Markers must be designed such that they don't effect subsequent wafer processing or device performance. Typically two alignment marks are used to align the mask and wafer, one alignment mark is sufficient to align

the mask and wafer in x and y, but it requires two marks (preferably spaced far apart) to correct for fine offset in rotation. In fig. 4.5 are sketched the process of alignment.

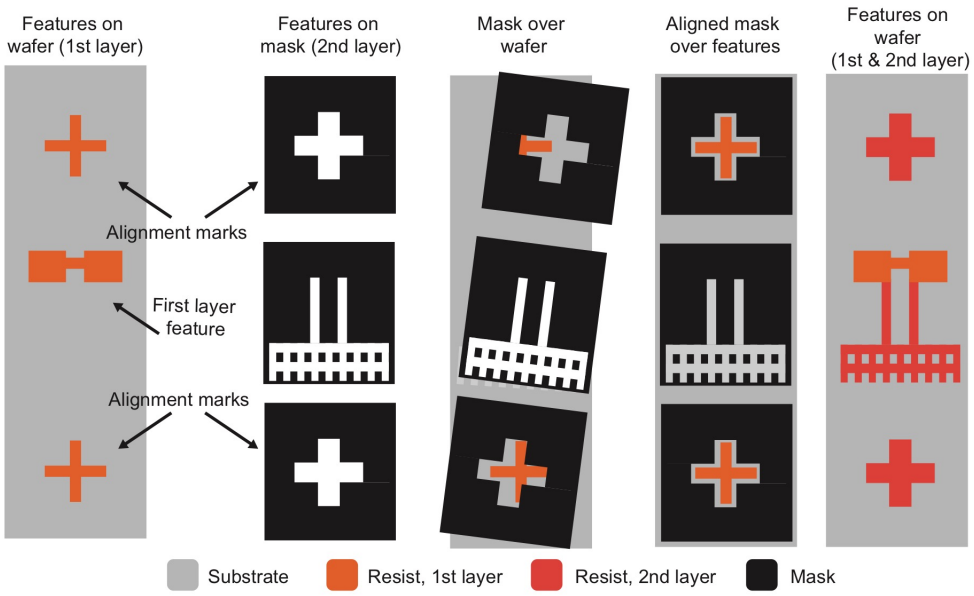

Figure 4.5: Use of alignment marks to register subsequent layers.

Depending on the lithography equipment the alignment may be done manually or automatically using a mask aligner; this kind of instrument have specific microscopes and stage micrometers for precise, micro-scale alignment of each layer's photomask with visible marks on the substrate wafer. They are indispensable tools for creating multilayer patterns with accurate registration. Modern mask aligner can easily reach an alignment precision up to 100 nanometer [147].

§ 4.4. Liquid photoresist: SU-8

SU-8 is one of the most common negative photoresist used in photolithography. It has been originally developed for the microelectronics industry for the fabrication of semiconductor devices. Today, it is mainly used for the fabrication of microfluidics devices thanks to its high sensitivity, chemical resistance and stability. It can be used for direct fabrication of microchannels [151] and to produce masters with relief patterns for molding devices in other materials [152]. SU-8 is an acid-catalyzed negative photoresist, made by dissolving EPON® SU-8 resin in an organic solvent gamma-butyrolactone (GBL). The structure of the monomer unit is shown in fig. 4.6a. Each monomer unit has 8 functional groups (epoxy rings), giving the commercial name of the chemical, the SU-8 [153].

SU-8 is very versatile PR and it can be used to realize structures with a wide range of height: from few micrometers up to 600 μm [154, 155]. This is achievable changing the rotational speed during the spin coating varying but also changing the concentration of the epoxy groups dissolved in the solvent. A wide range of photoresist viscosity from 7.5 cSt to 80000 cSt. During the spin coating deposition process can be used to The commercial SU-8 contains up to 10% wt of a mixture triarylsulfonium-hexafluoroantimonate salts as a photoinitiator fig. 4.6b. During

the UV exposure ($\lambda = 365\,\text{nm}$) of the film, acid photoinitiator is activated and acids are created. These acids catalyze cross-linking and polymerization of the film during the post exposure baking process. The polymerization reaction is illustrated in fig. 4.6c.

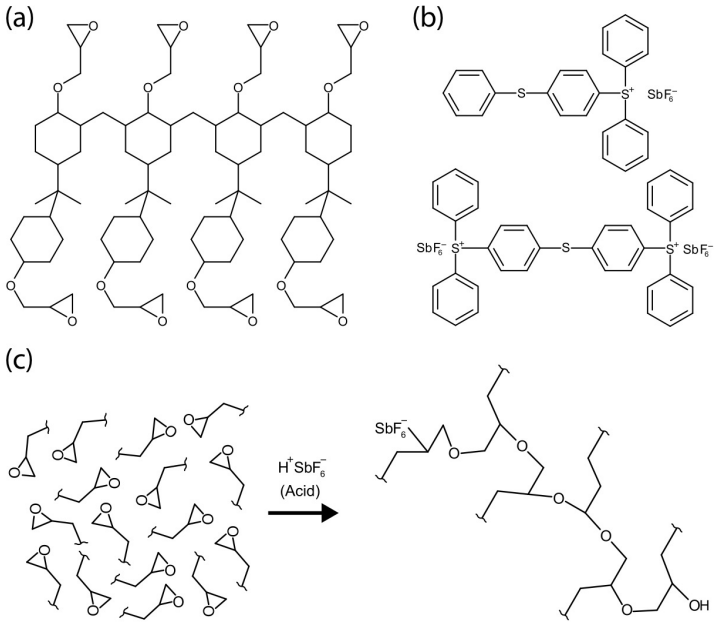

Figure 4.6: (a) Molecular structure of SU-8 monomer unit; (b) the mix of triarylsulfonium-hexafluoroantimonate salts used as photoacid initiator and (c) SU-8 polymerization reaction.

§ 4.5. Dry Film Photoresist

Dry film photoresists (DFR) were originally developed for printed circuit board (PCB) fabrication. Although application for MEMS (micro-electromechanical systems) fabrication is not very common, DFRs have been reported useful for fabricating electroplating molds [156, 157], sealing of microfluidic channels [158] and as a mask for powderblasting of microchannels [159]. DFRs offer many advantages over liquid resists, such as a good conformability, excellent adhesion to any substrate, good flatness, no necessity of liquid handling, no formation of edge beads, uniform resist distribution, low cost, short processing time and near vertical sidewalls [156]. In addition, it can be remarked that the setting up costs for DFR processing are significantly lower than for liquid resists. For sure the most important advantage of dry film photoresist is the uniform thickness provided by a carefully controlled coating process [160].

DFRs are typically three-layer structures: a polyethylene support base membrane; a resist layer varying in thickness between 5 and 150 μm depending on the intended application and a polyester cover sheet to protect the resist itself. While liquid photoresist is applied using a spin coater, DFRs are usually applied using hot roll lamination process, where photoresist is evenly rolled across the surface of the wafer with a controlled degree of pressure and temperature (see fig. 4.7). During lamination, bottom protection film is first removed while the resist remains on the upper side. After lamination and exposure, the other protection layer has to be peeled off without

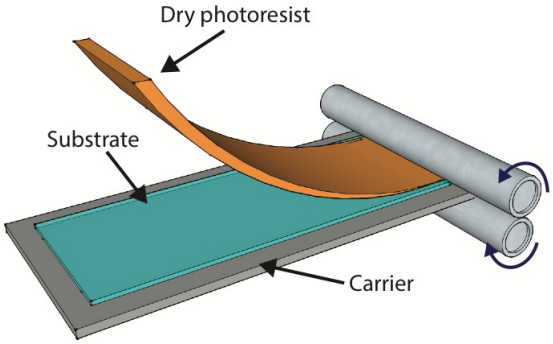

Figure 4.7: Schematic representation of the lamination processes of a dry film resist.

tearing the resist away from the surface. The lamination process has the objective of creating smooth and intimate dry contact between the substrate and the photopolymer. In contrast with liquid resist adhesion is normally not an issue working with DFRs.

§ 4.6. Cleanroom

One of the most important parameter to control during the microfabrication process is the cleanness of the substrate, the work environment and facilities. All the step of the photolithography usually take place inside a Clean Room (CR), which is a special enclosed area that is controlled with respect to the airborne particulates, temperature, air pressure, humidity, vibration and lighting. There are different kinds of clean rooms, which are classified according to the number of particles per cubic meter at a specified particle size. Just for comparison, a normal urban environment contains more than 35,000,000 particles per cubic meter of about 0.5 μm and larger, corresponding to an ISO 9 clean room, while an ISO 1 has only 10 particles per cubic meter of 0.1 μm and smaller [161]. The choice of the clean room depends on the size of the structures that are necessary to realize. During this work all the devices were been fabricated at the cleanroom of The Institute of Physical Chemistry of the Polish Academy of Sciences (ICHF-PAN) in Warsaw, Poland. The CR is a class ISO 7 (<2,930 particles with size of >5 μm), which is sufficient for the fabrication of devices with typical dimensions of about 10-100 μm.

5. Flow Visualization

The insight into a physical process is always improved if a pattern produced by this process can be observed by visual inspection. This is not so obvious in fluid dynamics because, most fluids, gases or liquids, are transparent media and their motion remain invisible. In order to be able to recognize the motion of the fluid, one must therefore provide a certain technique by which the flow is made visible. Such methods are called flow visualization techniques and they have always played an important role in the understanding of fluid mechanics phenomena.
In this chapter we introduce different techniques which are used for flow visualization (section 5.1). We focus on the description of direct flow visualization technique that uses tracers (section 5.2) in particular we describe in details Particle Image Velocimetry and Particle Tracking Velocimetry. In the last section we briefly describe how a tracking algorithm works (section 5.3).

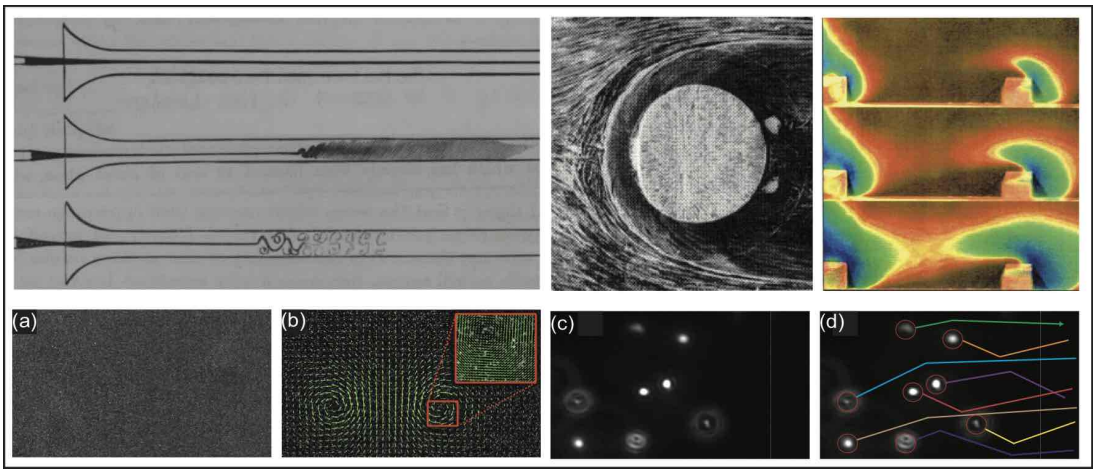

§ 5.1. Flow visualization techniques

Visualization is one of many experimental tools for surveying or measuring the flow of a fluid that is normally invisible due to its transparency. By applying the methods of flow visualization, a flow pattern is made visible and can be observed directly or recorded with a camera. The information on the flow is available for the whole field of view at a specific instant of time. This information can be either qualitative, thus allowing for an interpretation of the mechanical and physical processes involved in the development of the flow, or quantitative, so that certain properties of the flow (e.g., velocity, density) can be measured [162]. Also in microfluidics, direct flow visualization is of key importance for the fundamental understanding of micro-flows, analyzing, developing and evaluating novel microfluidic processes [163].

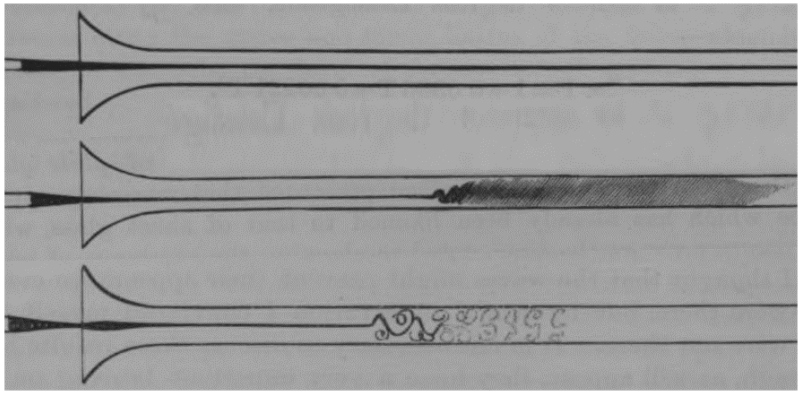

Figure 5.1: Water flow observed in a pipe, as drawn by Osborne Reynolds. Water flows from left to right in the transparent tube, and solid dye (represented in black). From top to bottom can be observed the transition from laminar to turbulent flow.

The methods of flow visualization can be classified according to three basic principles: i) light scattering from tracer particles, ii) optical methods relying on refractive index changes in the fluid and iii) interaction processes of the fluid flow with a solid surface.
The scattering and optical methods are based on the interaction of the fluid with light. A light wave incident into the flow field may interact with the fluid in two different ways: i) light can be scattered from the fluid molecules or from tracer particles with which the fluid is seeded; ii) the properties of the light wave can be changed due to a certain optical behavior of the fluid and, as a consequence, the light transmitted through the flow is different from the incident light. While the two former methods serve to visualize the pattern in the interior of a flowing fluid, the third method provides information on the transfer of momentum, heat, or mass between the fluid and a solid body.
In the next part we briefly describe the fundamental principle of these three fluid visualization methods, focusing on the physical principles and applications.

Optical method visualization

The properties of the light wave transmitted through the fluid flow may be changed due to changes of the refractive index of the fluid. The refractive index n is a function of the fluid density. The relationship is described by the Clausius-Mossotti equation. As the light wave arrives to the interface of two transparent media with different refractive indexes n_1 and n_2 its path and phase are altered; it is deflected from its original direction of propagation, and its optical phase is altered in comparison to the phase of the undisturbed wave. These alterations of the wave properties can be made visible in a recording plane at a certain distance behind the flow field under study. A particular method requires the use of an optical apparatus transforming the measurable quantity (light deflection, optical phase changes) into a visual pattern. The pattern is either qualitative [164, 165] (e.g. Shadowgraph, Schlieren) or quantitative [166] (e.g. Speckle, Interferometry), thus allowing for a deduction of data values of the refractive index or density distribution in the flow. Refractive index variations is particularly used in a fluid flow in which the density changes, heat release, or differences in concentration.

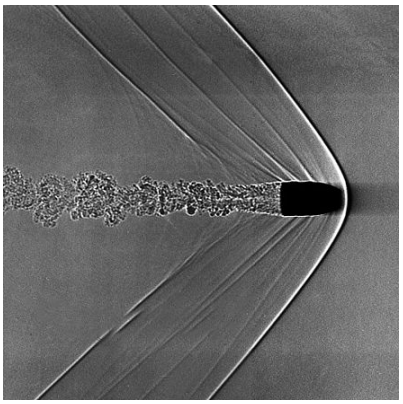

Figure 5.2: A Shadowgraph image of a supersonic bullet.

Surface flow visualization

The interaction of a fluid flow with a solid body is the subject of many experimental investigations. Such studies are aimed at determining, e.g., the shear forces, pressure forces, or heating loads applied by the flow to the body [167]. A possible means of estimating the rates of momentum, mass, and heat transfer is to visualize the flow pattern very close to the body surface. For this purpose, the body surface can be coated with a thin layer of a substance that, upon an interaction with the fluid flow, develops a certain visible pattern. This pattern can be interpreted qualitatively and, in some cases, it is possible to measure certain properties of the flow dose to the surface. Three different interaction processes can be used for generating different kinds of information:

- **Mechanical interaction** In the most common technique, which applies to air flows around solid bodies, the surface is coated with a thin layer of oil mixed with a finely

powdered pigment (see fig. 5.3a). Because of frictional forces, the air stream carries the oil with it, and the remaining streaky deposit of the pigment gives information on the direction of the flow close to the surface [168].

- **Chemical interaction** The solid surface of the sample is coated with a substance that changes color upon the chemical reaction with a material with which the flowing fluid is seeded. The reaction, and therefore the color change, is the more intense, the higher the mass transfer from the fluid to the surface.

- **Thermal interaction** The coating material changes color as a function of the surface temperature [169]. Observation of the respective color changes allows for determining the instantaneous positions of specific isothermal and deriving the heat transfer rates to surfaces as shown in fig. 5.3b.

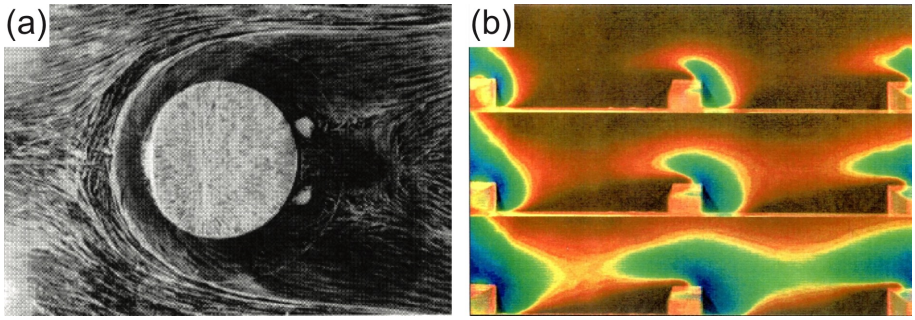

Figure 5.3: (a) Plan view of the air flow around a vertical circular cylinder as visualized with the oil film technique; (b) Surface flow visualization using thermochromic liquid crystal.

Visualization by Tracer Particles

Since the light scattered from the fluid molecules (Rayleigh scattering) is extremely weak, the flow is seeded with small tracer particles (e.g., dust, smoke, dye). These tracers have the aim to increase the scattered radiation from the fluid (see fig. 5.4). This methods assumes that the motion of the tracer is identical with the motion of the fluid, an assumption that does not always hold, particularly in unsteady flows. The scattered light simply carries information on the state of the flow at the position of the tracer particle [162]. These methods are discussed in more detail in the next section.

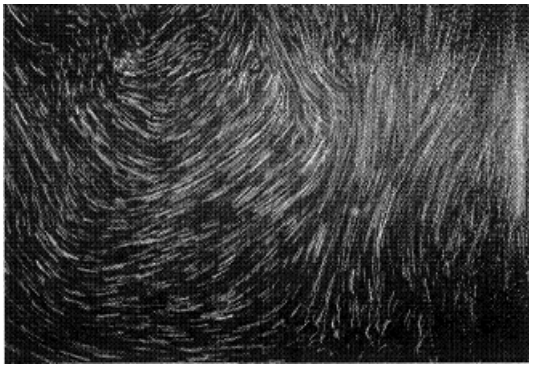

Figure 5.4: Stroboscopic exposure of tracer particles in a water flow.

§ 5.2. Tracers Methods

As briefly introduced in the previous section, tracers can be used to visualize the motion of single or multiphase flows. Tracking the movement and behavior of these particles, either individually as groups, allows to measure various features of the fluid motion such as diffusion or mixing.
This category includes techniques such as Laser Doppler Velocimetry (LDV) Particle Image Velocimetry (PIV) and Particle Tracking Velocimetry (PTV). The LDV measures the Doppler shift which results when light is scattered from a moving particle [170]. The PIV and PTV captures series of images with small time difference of tracers where are encoded velocity and directions on the flow.

§ 5.2.1. Particle Image Velocimetry and Particle Tracking Velocimetry

Particle Image Velocimetry and Particle Tracking Velocimetry are a well established measurement techniques for macroscopic flows and it extensively described in literature [171]. Both methods are a full-field non-intrusive measurement technique where the flow velocity is obtained by recording the displacement of small tracing particles seeded in the working fluid, that faithfully follow the local fluid motion. Moreover the two methods use similar experimental setup and make use the fundamental definition of velocity and estimate the local $\mathbf{u}$ from

$$\mathbf{u}(x,t) = \lim_{\Delta t \to 0} \frac{\Delta x(x,t)}{\Delta t} \tag{5.1}$$

where Δx is the displacement of a tracer initially located at position x and in time t, over a short time interval Δt separating observations of the marker image.
The main difference between PIV and PTV is the data analysis; PIV is an Eulerian method that measure the velocity filed of a group of particle, PTV tracks the trajectories of individual particles [172].
Tracers identification and determination of its position in space is a fundamental step in PTV. This is only possible if the number of particles per unit volume ρ_N=N/V where N is the number of particles in a observation volume V, is not too high. In the left side of fig. 5.5 are reported for comparison two experimental images regarding PIV (a) and PTV (c) while in the right side

are reported the results of the analysis for each of two techniques.
Micro-PIV (μ-PIV) or Micro-PTV (μ-PTV) is a modification of standard PIV and PTV techniques in order to access the small scales of microfluidic devices, allowing to reach sufficiently small spatial resolutions. Introduced in 1998 by Santiago *et al.* [173] these two techniques provide today one of the the most accurate methods to monitor, visualize and measure fluid velocity.

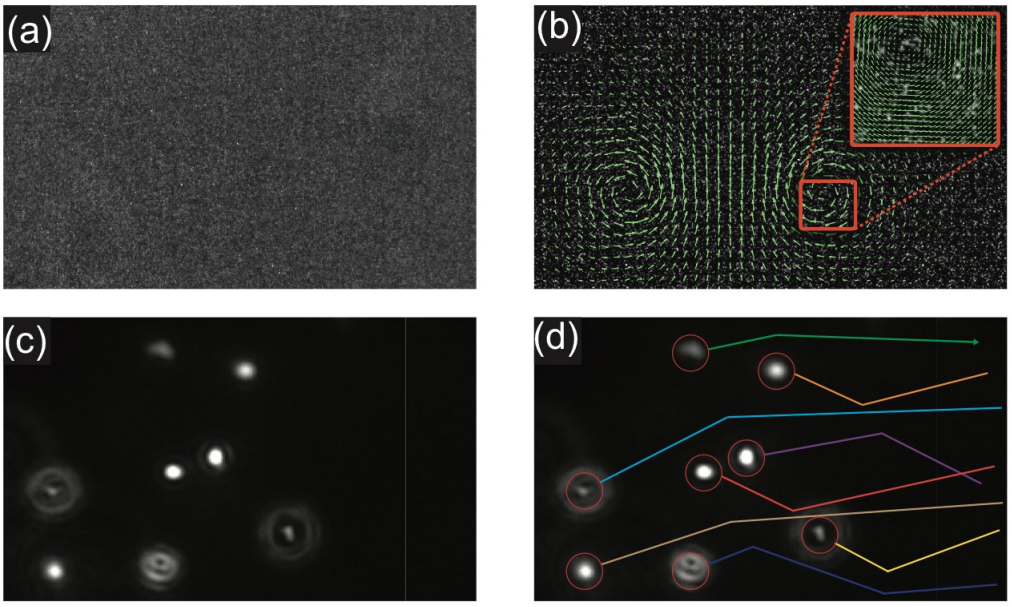

Figure 5.5: Example of experimental images (a) and the results (b) of Particle Image Velocimetry. Particle Tracking Velocimetry images and analysis (c, d).

§ 5.2.2. Tracer Particles

Tracer particles can be solid, liquid or gaseous and are usually injected directly into the fluid. Ideally they should be spherical, and mono sized. Since the host fluid velocity is inferred from their motion, selected particles must be capable of following the fluid motion with accuracy and precision without perturb it. An adequate number of particles must be present, as required by the experiment, but not so many as might affect the fluid behavior. In addition, tracer particles should exhibit good light scattering ability, but this is not always possible and is strongly dependent on the examined fluid. Generally fluorescence dyes are adopted.
Fluorescence is the emission of photons by an atom or a molecule, following to a temporary excited electronic state caused by absorption of photons of a certain wavelength from an external radiation source. When a fluorophore (i.e., a fluorescent molecule) absorbs a photon with energy E_0, an electron is excited from its ground state E_0 to a higher energy state (Excited state 1) corresponding to the energy of the absorbed photon, see fig. 5.6a. Due to the fluorophore's interactions with its molecular environment during the excited state, there is a loss of energy resulting in a relaxed excited state with energy E_2 (Excited state 2) from which fluorescence emission originates. After a short time interval the excited electron collapses back to the ground

state, emitting a photon of energy E = E_2 - E_0 corresponding to the difference between the electron's excited and ground states. The energy of a photon is given by

$$E = E_2 - E_0 = \frac{hc}{\lambda} \tag{5.2}$$

where h is Planck's constant, c is the speed of light, and λ is the wavelength. As $E_2 < E_1$, the wavelength for the fluorescent emission λ_{emit} is longer than for the absorbed radiation λ_{abs}.

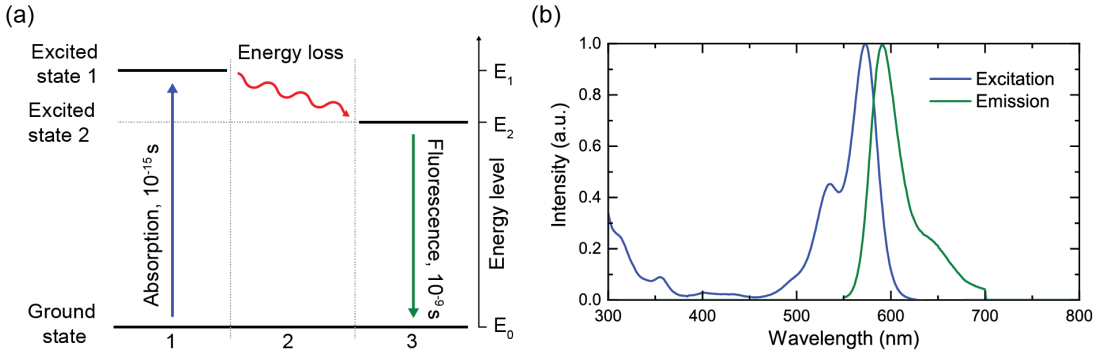

Figure 5.6: (a) Energy diagram illustrating the energy state transitions leading to fluorescence decay to the ground state. (b) Excitation and the red shifted emission profile of Rhodamine red dye.

The difference between the peak excitation and emission wavelengths, for a fluorochrome, is the so-called Stokes' shift, as depicted in fig. 5.6b. Due to variations in electrons' persistence in the excited state and, therefore, changes in energy loss prior to fluorescent emission, fluorophore emit photons over a continuous spectrum of wavelengths, the emission spectrum, even when excitation is performed by a monochromatic light source. In particle tracers, the fluorescent properties of tracing particles are crucial for successful particle imaging. The excitation wavelength λ_{abs} of the fluorescent dye loaded on the tracers should closely match the wavelength of the illumination source, to ensure high fluorescence intensity. Moreover, λ_{emit} should be sufficiently different for the optical filters and dichroic mirror to effectively filtrate the illumination wavelength, without loss of the emitted fluorescence signal.

§ 5.2.3. μ-PTV System Components

A typical μ-PTV system is sketched in fig. 5.7. As a monochromatic light source it is common to used a laser system. The illumination light is delivered to the microscope through several optical elements that deflect the light so that it fills the back of the objective lens, and thereby allows a broad illumination of the microfluidic device.The illumination light is reflected upward towards the objective lens by a mirror, which is designed to reflect the wavelengths form sources and and transmit all the others. Another possible solution is to use continuous chromatic light sources, such as an Hg-arc lamp or halogen lamp, to provide illumination light; in this situation, an excitation filter must be used to allow only a narrow wavelength band of light to illuminate

the test section. The choice of the microscope lens properties is of crucial importance for high resolution measurements. Generally are used high numerical aperture lens where NA, defined as the product $n \cdot \sin\Theta$, where n is the refractive index of the objective's working medium and Θ is the half-angle of the light collecting cone.

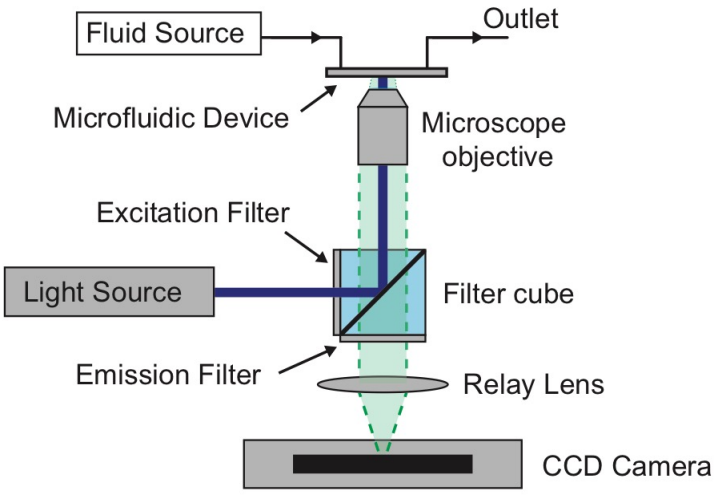

Figure 5.7: Schematic of a micro-PTV system.

Typically, the working fluid is directed through the microfluidic device by pressure or using a syringe pump. The working fluid can be any visibly transparent fluid (such as water) seeded with fluorescent particles. The particles can be made of a variety of materials and are coated with a fluorescent dye with an excitation wavelength closely matched to the light source, and an emission wavelength closely matched to the barrier filter. Suitable particles can be purchased from a number of manufactures. The microfluidic chamber has at least one optically transparent wall, so that it can be viewed through the microscope lens. A barrier filter is positioned between the mirror and the relay lens. The barrier filter filters out the illumination light that is reflected by the surface of the flow chamber or scattered by the particles. A sensitive and fast sCMOS (scientific CMOS) camera is commonly adopted to record the particle image fields. A large-format sensor is desirable because it allows more particle images to be recorded and increases the spatial dynamic range of the measurements.

§ 5.2.4. Depth of field

The depth of field δz of a microscope objective is given by Inoue and Spring [174] and it is defined as the resolution in the depth direction. For a standard wide field microscope δz is equal to

$$\delta_z = \frac{n\lambda_0}{NA^2} + \frac{ne}{NA \cdot M} \tag{5.3}$$

where n is the refractive index of the fluid between the microfluidic device and the objective lens, λ_0 is the wavelength of the imaged light in vacuum and e is the smallest distance that can be resolved by a detector placed in the image plane of the microscope; for a CMOS sensor, e is the pixel-to-pixel spacing on the CMOS chip. In eq. (5.3) the first term on the right-hand side is the depth of field resulting from diffraction while the second term refers to geometrical effects.

§ 5.3. Particle tracking theory

Particle tracking is the observation of the motion of individual or multiple particles within a medium. Generally, the tracking algorithm analyzes the particles coordinates (x, y, z) in 3D space, over a series of frames and outputs the movements of the particle: the trajectory. The trajectory can be analyzed to identify modes of motion or heterogeneity in the motion such as obstacles or regions of fast transport (e.g. due to active transport or flow).
There are a variety if algorithm, but all of them have a similar approach to the problem. At the basis of all tracking algorithms there are four fundamental features: spot detectors, spot analyzer, spot tracker and track analyzer.

- **Spot detectors**: This part is responsible for spot detection in the image. All detectors modules provide the following spot features: the spot coordinates in space (x, y, z), the spot diameter (d), the quality of the spot. This last value reflects the quality of automated detection. This feature is used in the initial filtering step, where spots with a quality lower that a specified threshold are simply discarded.
  The most common algorithm for particle detection is based on Laplacian or Gaussian filtering [175]. Given an approximate expected particle diameter d two Gaussian filter are produced with standard deviation $\sigma_1 = 1/(1 + \sqrt{2}) \times d$ and $\sigma_2 = \sqrt{2} \times d$. The image is filtered using these two Gaussians, and the result of the second filter (largest sigma) is subtracted from the result of the first filter (smallest sigma). This yields a smoothed image with sharp local maximas at particle locations. A detection spot is then created for each of these maximas, and an arbitrary quality feature is assigned to the new spot by taking the smoothed image value at the maximum.

- **Spot analyzer**: Spot features, such as *Max intensity*, *Estimated diameter*, etc., are calculated for all spots just after the initial filtering step. They are then used to select spots, based on filters set to retain only spots with a given feature below or above a specified threshold.

- **Spot tracker** This feature is the core of the entire tracking algorithm and aims to take the filtered spots and link them together to build tracks. There are several algorithms available e.g. Particle filtering, Linear Assignments Problems (LAP), linear motion tracker. In this work we used a Linear Motion LAP tracker, implemented by Tinevez and coworkers [176].

Briefly, the Linear Motion tracker relies on the Kalman filter [177] to predict the most probable position of a particle undergoing constant velocity movement. Each track, initiated from a pair of spots, is used to create an instance of a Kalman filter. In the next frames, each filter is used to generate a prediction of the most probable position of the particle. Then, all the predicted positions are linked to the real spot positions in the frame (based on square distance), and then added to the track corresponding to the predicted position they were linked to.

- **Track analyzer** Like for spot analyzers, this features operate on whole track. it is used to report track mean velocity or displacement. It is also used to filter spurious or anomalous tracks.

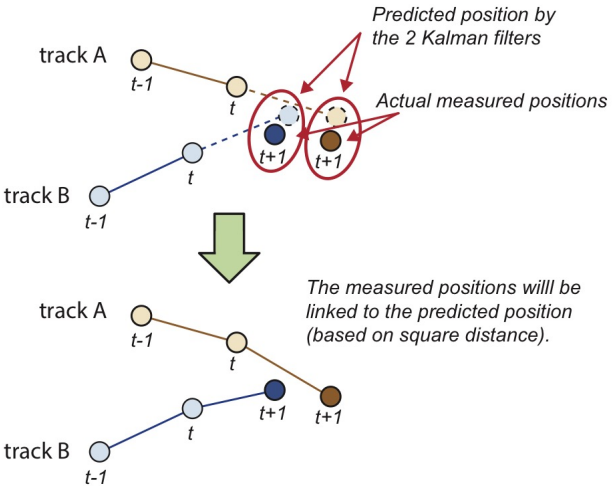

Figure 5.8: Linear motion tracker and Kalman filter is used to predict the most probable position oa a particle.

6. Materials and Methods

This Chapter is dedicated to the description of the experimental procedures used in this work to study the behavior of concentrated emulsion flowing in rough microfluidic channels. In the first section (section 6.1) we describe the emulsion preparation method and we report its rheological characterization. In section 6.2 we present the microfabrication protocol used for the realization of microfluidic channel. The section reports all the fabrication parameters and the characterization of the micro structured roughness performed with optical profilometry. In section 6.3 we describe in detail the micro Particle Tracking Velocimetry set-up and the apparatus used to control the emulsion flow. As last, in section 6.4 we describes how collected images are analyzed, and how the flow velocity profiles were reconstruct from them. The custom-made program used for the analysis is included is appendix A.

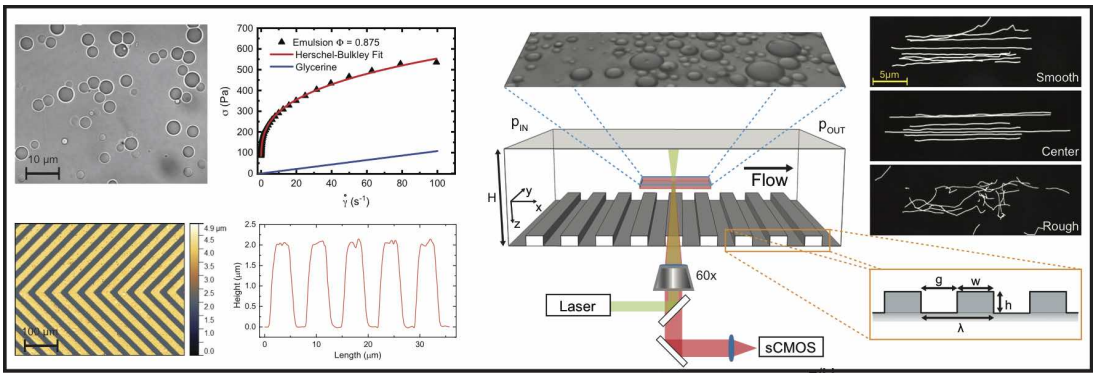

§ 6.1. Dense Emulsion

§ 6.1.1. Emulsion preparation

In this Thesis we use a concentrated emulsion as model of Soft Glassy Material. As described in chapter 3 there are several methods to produce an emulsion. Te emulsion has been prepared by simply mixing the oil and aqueous phases using a homemade spatula mixer. This method allow us to obtain in a large amount of emulsion (∼300 mL) in few hours without using complicated or expensive machines. A picture of the apparatus is reported in fig. 6.1.

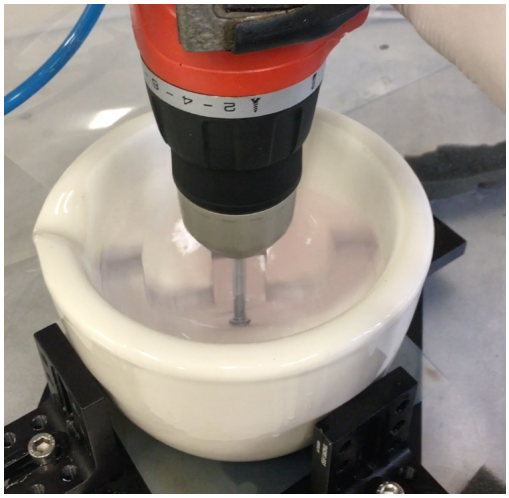

Figure 6.1: Picture of the homemade spatula mixer.

To reduce scattering or other optical distortions during Particle Image Velocimetry image acquisition, our emulsion must be transparent. Moreover it has to be stable in time and with a defined droplet size. To obtain a transparent emulsion is necessary that the refractive indexes of two phases (continuous and dispersed) are equals. In this work, the only way to obtain the match is to use a volume fraction of the glycerol-water blend for which the refractive index is equal to the silicone oil ones. The refractive index n of two liquids' mixture is given by the Clausius-Mossotti relationship

$$\frac{n^2-1}{n^2-2} = \frac{n_2^1-1}{n_2^1+2}\Phi_1 + \frac{n_2^2-1}{n_2^2+2}(1-\Phi_1) \tag{6.1}$$

where n_1, n_2 and Φ_1, $\Phi_2 = 1-\Phi_1$ are respectively the the refractive index and the the volume fraction of the two components [178]. At first we measure the refractive index of pure components: silicone oil (Rhodosil 47 v 1000, Bluestar Silicones, France), water and glycerol (Sigma Aldrich, Germany) with a refractometer (DSR-λ, Schmidt + Haensch, Germany). We obtain respectively: $n_{oil} = 1.4068$, $n_{water} = 1.3330$ and $n_{glycerol} = 1.1499$. Then, we prepare small amounts of glycerol and water mixtures with different volume fraction, from 0.45 to 0.55 and we measure the refractive indexes of each blends. As reported in fig. 6.2 the best refractive index matching is at $\Phi_{gly/water}$=0.54.
Hence, we prepared the emulsion using as dispersed phase silicone oil (poly-dimethyl siloxane,

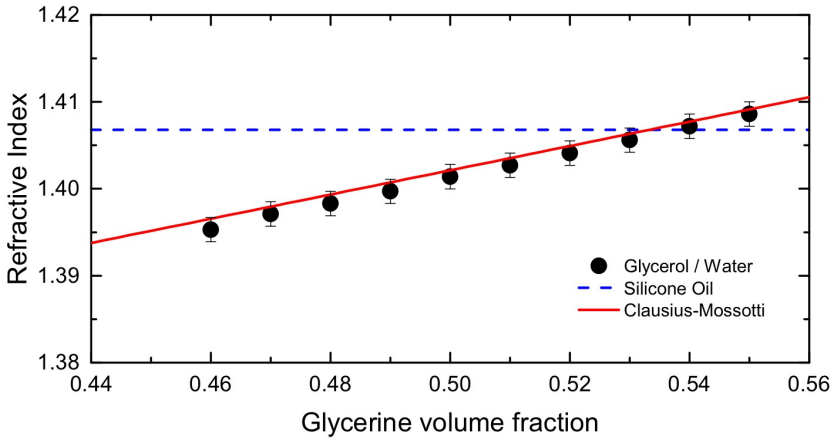

Figure 6.2: Measured refractive indexes as a function of the glycerol/water volume fraction Φ. Solid dots and red line refer respectively to measured and calculated (with eq. (6.1)) refractive index of glycerol/water solution. Blue dashes line represents refractive index of silicone oil.

η=1000 mPa s) and a glycerine-water mixture 54% (w/w) as continuous phase. Tetradecyl-trimethyl-ammonium bromide (TTAB) $C_{17}H_{38}N^+Br^-$ is added to the continuous phase (1% wt) as surfactant. Moreover, at the continuous phase we added a diluted suspension (0.002% wt) of fluorescent nanoparticles (size of $d \approx 0.2$ μm) used as tracers during Particle Tracking Velocimetry measurements. The continuous phase (containing the surfactant and the fluorescent tracers) has been put in the spatula mixer and the oil phase is added at the ratio of ∼1 ml/minute under constant and intense shearing until the volume fraction of the oil reached Φ=0.93. In this condition the emulsion is very dense and unstable so, for stability reasons, we added continuous phase to bring down the volume fraction to Φ=0.875, which we used as a stock solution. Prior to use it in the experiments we diluted this stock emulsion to the required volume fraction by adding a controlled amount of continuous phase. We prepared our samples by controlling the mass fraction, Φ_w. Nevertheless, it is more consistent to refer to the volume fraction in oil Φ_{oil}. The relationship between the two quantities is given by

$$\Phi_1 = \frac{\Phi_w/\rho_{oil}}{\Phi_w\rho_{oil} + (1-\Phi_w)/\rho_{aq}} \tag{6.2}$$

where the density of the oil is $\rho_{oil} = 0.97$ kg/L and the density of the continuous phase is ρ_{aq}=1.14 kg/L. After the dilution, the emulsion was poured in syringes and they were centrifuged to remove air bubbles. The process does not modify the droplets size and does not influence the emulsion size distribution.

§ 6.1.2. Concentrated Emulsion Characterization

To fully characterize the emulsion we need information about microstructure (i.e. mean droplet diameter, size distribution) and rheological behavior. We measure the mean diameter d, and the size distribution of the emulsion by optical method; we diluted a small sample of emulsion in aqueous solution of 1% TTAB, then placed a few drops of this solution between two microscope

cover slips and took a large number of optical images under bright field optical microscope with a 100 × magnification objective. With a FIJI software [179] we analyzed the images, averaged the measured values and determined the mean droplet diameter as d. The polydispersity was determined as the coefficient of the variance (CV=σ/d ×100%). Approximately 8500-10000 droplets were measured. To test the stability of the emulsion we repeated the measurements a few times within a two months period during which the experiments took place and no noticeable difference was observed. Moreover we measured samples before injecting the emulsion into the microchannels and after they flew through it and again, no difference was detected.

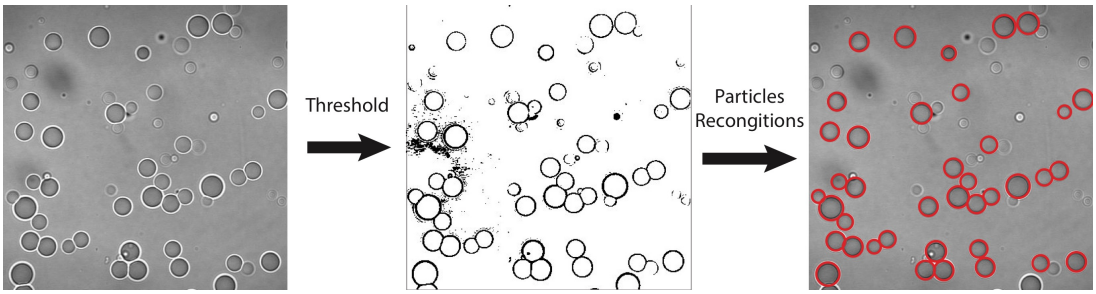

Figure 6.3: Image of a semi-dilute emulsion during the size distribution analysis.The red circles are the particles detected by FIJI software.

To measure the rheology, we have employed a cone-plate rheometer (ARES 4400, TA Instruments). This device is composed of a static plane and a cone, which turns under a torque of Γ at an angular velocity of ω. The angle of the cone, α, is equal to 0.04 radiant (2.29 degrees). To avoid contact with the bottom surface, the cone lifted up, and the gap between the cone tip and the bottom is fixed. Moving from center in radial direction the gap is proportional to the distance from the center: $g(r) = \tan(\alpha)r$. Because the shear rate is proportional to the distance from the center divided by the gap, it is constant in the sample

$$\dot{\gamma} = \omega r/g(r) = \omega/\tan\alpha \tag{6.3}$$

For most materials, the stress is a function of the shear rate; therefore, it should also be constant in all of the samples

$$\sigma = \frac{3\Gamma}{2\pi R_0^3} \tag{6.4}$$

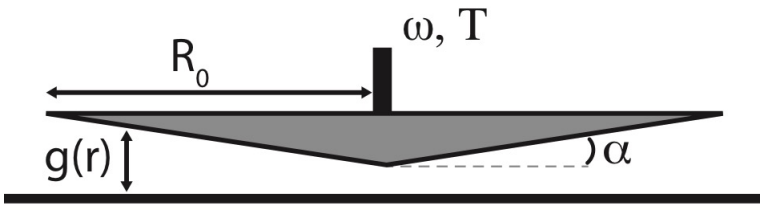

Figure 6.4: Schematic draw of the cone-plate rheometer.

Figure 6.4 depicts the cone-plate geometry. Depending on the rheometer, the torque or the angular velocity is imposed and the other is measured. We used a stress controlled rheometer working at a steady state to measure the flow curve. At $\phi > \phi_{RCP}$, the emulsion presents a yield stress and its rheological behavior could be described by the Herschel-Bulkley model, where $\sigma = \sigma_0 + A\dot{\gamma}^n$ (with n=0.5). An example of characteristic bulk rheological curve for a dense emulsion is reported in fig. 6.5. After the passage through the channel a small decrease in the stress at a constant shear rate is observed. This decrease may be a result of coalescence at high shear rates but the variation is negligible respect to the initial value of yield stress σ_0.

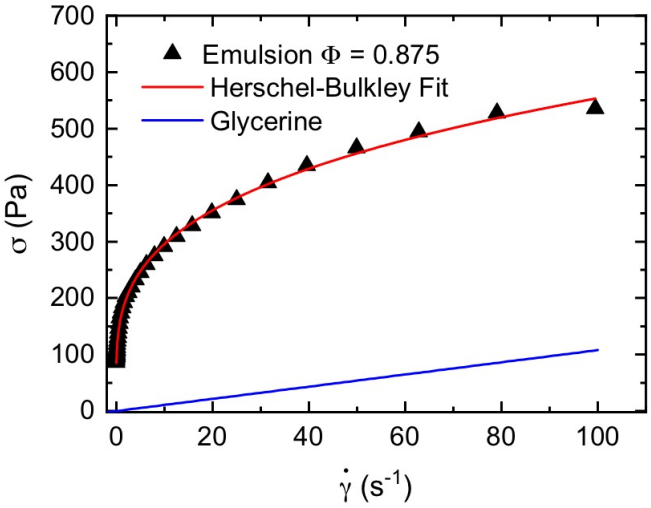

Figure 6.5: Bulk rheological curve for a dense emulsion above the jamming point fitted with Herschel-Bulkley model (red line). Blue line is the rheological curve for pure glycerin used as Newtonian reference.

§ 6.2. Microfluidic channel

To study and understand the effect of wall roughness on the flow of a dense emulsion we used several microfluidic channels with a characteristic roughness located on the bottom wall of the channel. This roughness presents a length scale comparable with the emulsion droplets and it was designed with two different topologies. The first consists in rectangular grooves orientated perpendicularly to the flow direction, while the second one consists on the same grooves, but they present an herringbone pattern. In this section we report the fabrication details and the characterization of the microfluidic channel with these two micro-patterns. We realized these samples at the Institute of Physical Chemistry, Polish Academy of Science (Warsaw, Poland) in the group of Prof. Piotr Garstecki.

§ 6.2.1. Fabrication details

The microfluidics devices have been fabricated by standard multilayer UV photolithography using SU-8 photoresist (Microchem, USA) following all the steps described in section 4.2. In

the first step we cleaned a 75×50 mm glass plate (thickness of 1 mm) with ethanol ultrasonic bath for 15 minutes and then dried with nitrogen. In the second step we uniformly deposited a thin ($\sim 2\mu$m) layer (labeled as 0^{th} layer) of SU8-2002 using a spin coater (Laurell WS-650, USA). We observed that this thin layer is necessary for better adhesion of the next resist layers to the substrate. After the complete polymerization of this layer we deposited another layer of resist to realize the micro-grooves (1^{st} layer) as structured roughness. Their height was chosen to be $h \leq 0.5\ d$ (d being the mean diameter of the droplets in the emulsion), since the effect of roughness is expected to be more pronounced for this value [19]. After all the photolithographic process the samples were hard baked to increase hardness and stability. As last step we realized the channel walls; we deposited SU8-2150 (2^{nd} layer) with a height $H_{\text{wall}} \simeq 180\ \mu$m. Fabrication parameters used in the realization of the 3 different layer are reported in table 6.1.

Table 6.1: Fabrication parameters for each layer: the 0^{th} layer used for better adhesion, the 1^{st} layer used for micro-grooves and the 2^{nd} layer used as channel walls.

Layer	Spin Coating	Soft Bake	Exposure	Post Exposure Bake	Development	Hard Bake
0^{th}	@2000rpm	2min @ 95°C	20" + 20"	5min @ 95°C	-	-
1^{st}	@1500rpm	2min @ 95°C	8" + 8"	7min @ 95°C	5min	2min @ 150°C
2^{nd}	@1500rpm	7min @65°C 30min @95°C	32" + 32"	5min @65°C 15min @95°C	10min	5min @ 150°C

As a cover plate we used a 24 × 75 mm microscope glass slide, on which we drilled holes (prior to bonding) for inlet and for outlet. We injected a small amount of Norland Optical Adhesive (NOA 63; Norland Products Inc., USA) all over the outside of the channel walls using a syringe and a needle. After that, on the two ends of the device, we put a piece of microscope cover slips ($s = 220\ \mu$m) as a spacer, put on the cover plate with holes, fixed it using a paperclip and cured the adhesive under UV light. The final channel height, H, was determined by the thickness of the spacer (i.e., $H = 220\,\mu$m). The fabrication process is depicted in fig. 6.6.

The previous fabrication method requires multilayer photolithography and a it is very expensive in term of time. To speed up and simplify the fabrication process we developed another strategy for the fabrication of V-grooves patterned channels. The fabrication steps for the deposition of the first and second layers (the one containing the grooves) remain the same. In the last step, instead of using ultra thick resist SU8-2150 for the realization of the channel walls we used a dry film photoresist WBR-2000 (DuPont, USA). This method allowed to avoid the difficult and time consuming deposition of the SU8-2150 and the complicated procedure multilayer photolithography.

To fabricate the channel walls using this dry photoresist, we first cut a piece of it slightly bigger than the glass plates containing the structured roughness. Then, using a knife plotter (Craft Robo CC200-20, Graphtec, Japan) we cut the channel shape. We laminated the resist to the

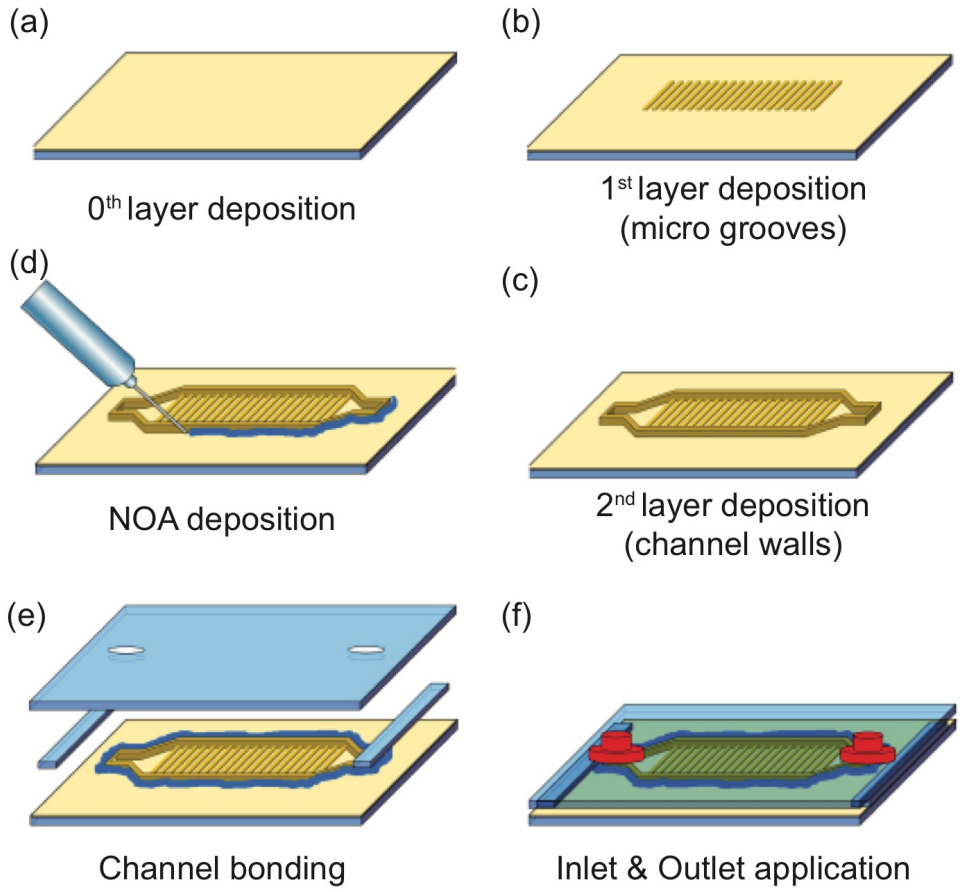

Figure 6.6: Schematic representation of channel fabrication: (a) realization of 0^{th} layer, (b) deposition of the microstructured grooves (first layer), (c) deposition of the channel walls (second layer), (d) deposition of NOA for channel bonding, (e) Bonding of spacers and cover plate, (f) realization of tubes connections.

glass plate removing the trapped air bubbles. To bond the cover plate (with drilled holes for inlet and outlet) we put the sample under a hydraulic press for 5 minutes at 80°C with a pressure of 2 bar. With this step we "pre-bond" the cover plate to the cover glass. Finally, to fix the different layer and to polymerize the photoresist, the sample was exposed to UV light (i-line 365nm) for 60 seconds. Using dry photoresist the fabrication process is more reproducible and the height of the channel is simply determined by resist thickness $H = 120\,\mu$m.

§ 6.2.2. Roughness topologies

Straight Grooves: The roughness consists in an array of rectangular posts of width w, gap g and period $\lambda = w+g$ as depicted in fig. 6.7a. The posts cover the whole width of the channel and were orientated perpendicularly to the direction of the flow. We fabricated different combination of gaps and widths ranging from 6 to 37.5 μm as summarized in table 6.2.

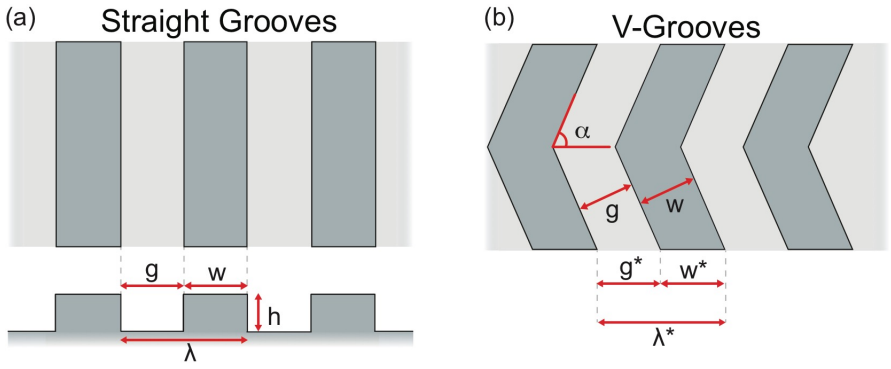

Figure 6.7: Characteristic dimensions of straight (a) and V-shaped grooves (b).

Table 6.2: Summary of straight grooves patterns used in our experiments. Wide ranges of groove spacing (g) and post widths (w) were used.

g (μm)	w (μm)				
6†	6	8	-	20	-
8	-	8	15	-	37.5
15	-	8	15	-	37.5
20	-	8	-	20	-
37.5	-	8	15	-	37.5

†For technical reasons, in channels with gap spacing $g = 6\,\mu$m only the emulsions with $\Phi = 0.875$ was tested.

Herringbone grooves: Rectangular posts are fabricated with a fish bone shape as sketched in fig. 6.7b. Grooves are characterized by the same quantities w, g, as straight groove, and by the angle α defined as the grooves intersection angle with the channel longitudinal axis. We labeled with w^*, g^* and λ^* the effective width a gap and lambda for tilted grooves. We selected only symmetric combination of w^* and g^* with length 8, 15 and 25 μm with 3 different angles: 30°,

45° and 60°. A summary of V-shaped grooves is reported in table 6.3.

§ 6.2.3. Channel Characterization

To characterize the goodness of microgrooves patterns we used an optical profilometer (SENSOFAR S neox, Spain). It allows to obtain a 3D surface topography of a large area in few seconds with a resolution up to 0.2 μm (magnification of 50×). The patterning structures have a reproducibility within 1%. We can observe that the structures have nice sharped edges and the surfaces have a mean roughness (RMS) of 150 nm that is negligible respect to the grooves height ($h \sim 2,5\,\mu$m). Conversely, we observed that random fluctuations of the channel height H are due to fabrication imperfections. These fluctuations are more evident in the multilayer procedure than in the DFR process, but they are always below 5%. In fig. 6.8 are reported an example profilometer scan with relative extracted profile.

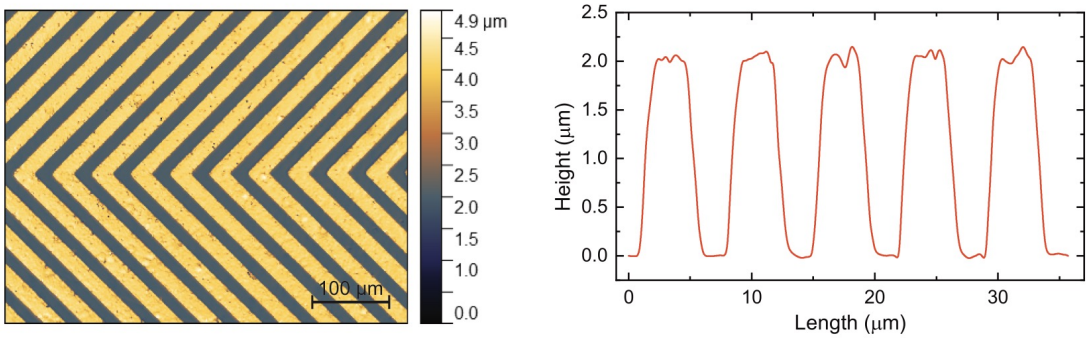

Figure 6.8: Profilometer scan and extracted profile for herringbone grooves: w^*=25 μm, g^*=25 μm and α=45 deg.

§ 6.2.4. Surface modification

We observed that our emulsion easily coalesces when it flows inside the microfluidic channel. This phenomenon take place either for glass and resist surfaces. Moreover, the two materials have different interaction with the emulsion; indeed the different wetting properties of the surfaces can influence the slip velocity. To avoid these problems, we added a non-ionic hydrophilic coating produced with Polyvinylpyrrolidone (PVP).

To realize a hydrophilic inner surfaces we treat the closed microfluidic chip with a oxygen plasma to activate the inner surfaces. Then, with a syringe pump, we flux a 2.5% (w/w) PVP (Polyvinylpyrrolidone K90, AppliChem) water solution inside the channel for 2 hours with a flow rate of ∼1.5 ml/h. To verify the goodness of the surface treatment we performed contact angle measurements with a dedicated set-up depicted in fig. 6.9. The apparatus consists in a optically transparent box filled with the continuous phase of the emulsion: water and TTAB (1% w/w). The sample is immersed in the liquid with interested surface faced to the bottom. Using a syringe connected to a bend needle and controlled by a syringe pump (UltraMicroPump 3, WPI, Germany), oil droplet with a fixed volume of 1 μl was deposited on the surface. Images

Table 6.3: Summary of V-grooves patterns used in our experiments.

Angle [deg]	Width-Gap combination (A) [μm]	Effective Width-gap combination(B) [μm]	Image
30	4-4	8-8	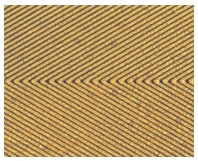
	7.5-7.5	15-15	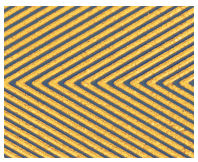
	12.5-12.5	25-25	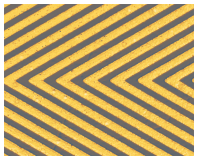
45	5.5-5.5	8-8	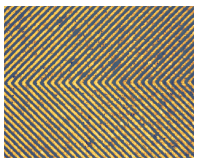
	11-11	15-15	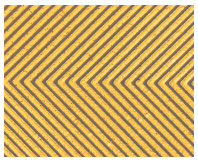
	18-18	25-25	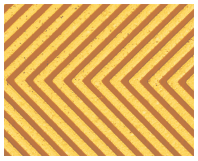
60	7-7	8-8	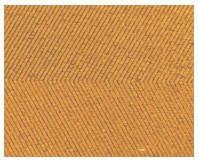
	13-13	15-15	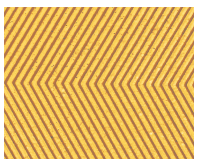
	21-21	25-25	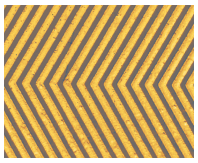

were recorded by a CCD camera connected to a computer and the analyzed with a custom-made LabVIEW software to measure the contact angle.
Images and contact angle values for glass and SU8 surfaces, before and after the surface modification are reported in fig. 6.9. Since we obtain the same contact angle values with the glass and the resist, we can conclude that the coating is as good on the resist as on the glass.

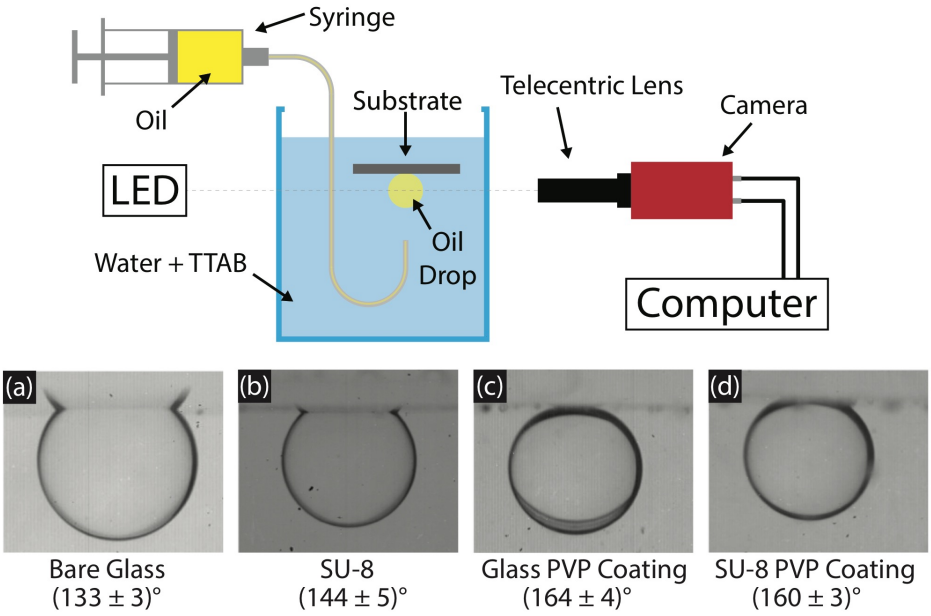

Figure 6.9: Dedicated apparatus for the measurements of the contact angle. Equilibrium contact angles for oil drops immersed in water and TTAB on Glass and SU8 before (a, b) and after the PVP coating (c, d).

§ 6.3. Micro-PTV experimental setup

The experimental set-up, used for the micro-Particle Tracking Velocimetry, consists in a motorized inverted microscope (Eclipse Ti-E, Nikon, Japan) coupled to a sCMOS camera (Zyla 5.5, Andor, UK). The emulsion inside the channel was illuminated with a DPSS laser beam with a wavelength of 532 nm and a maximum power of 5 mW. A scheme of the experiential setup is depicted in fig. 6.10.
We acquired fluorescence images of tracers dispersed in the continuous phase of the emulsion; these particles are free to move in the continuous phase and they are not adsorbed on the droplets surfaces. As tracer particles we used polystyrene microspheres (FluoSpheres™, Thermo Fisher, USA), size of 0,2 μm diameter loaded with orange fluorescent dyes which have absorption and emission peaks at 540 nm and 560 nm (see fig. 6.11). A dichroic TRITC band-pass emission filter with spectral bandwidth $570 - 620$ nm was placed before the camera. The dichroic mirror cuts the light of the laser source used to illuminate the sample from above, in the epiluminescence configuration, and it transmits the emission spectrum to the camera.
We used a 60× magnification, apochromatic corrected, long working distance WD = 2 mm objective with a numerical aperture NA = 0.7 (SuperPlan Fluo, Nikon, Japan), whose vertical

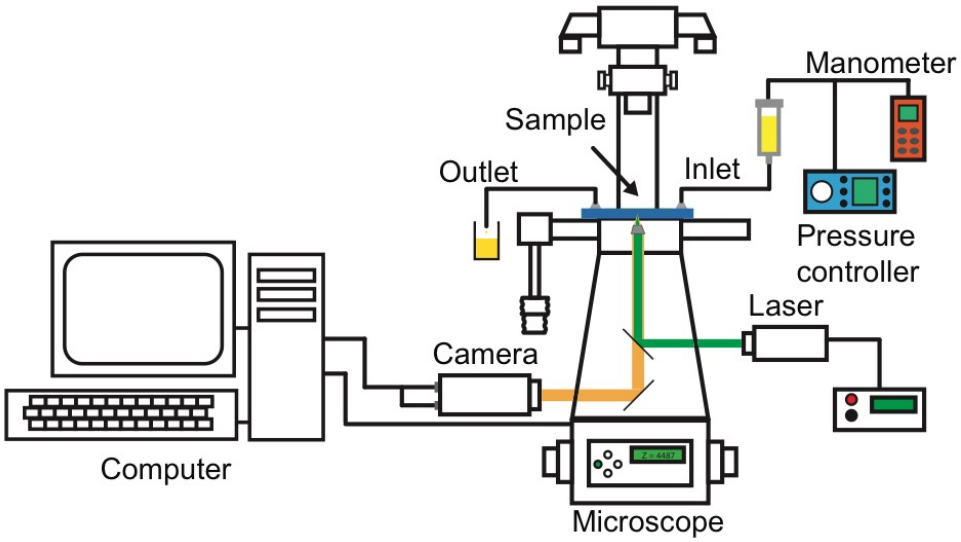

Figure 6.10: Schematic draw of the experimental set-up.

position can be fine adjusted with step resolution of 0.025 μm. The depth of field δ_z of the microscope objective is

$$\delta_z = \frac{n\lambda_0}{NA^2} + \frac{ne}{NA \cdot M} = 1.5 \ \mu\text{m} \tag{6.5}$$

for n = 1.41 (emulsion refractive index), $\lambda_0 = 532$ nm (wavelength of the imaged light in vacuum) and e = 10 μm (pixel-to-pixel spacing on the CCD sensor). We collected images with a resolution of 320×64 pixels (corresponding to a field of view of 35×7 μm.
The pressure, used to flow the emulsion, was applied using a pressure controller (F4200N.1, Fisnar, Italy) where the amount of pressure was easily controlled by a manual valve. The difference of pressure between the channel inlet and outlet was measured with a digital manometer in the range of 0-5 bar with a precision of 5 mbar.

§ 6.3.1. Experimental procedure for data acquisition

The channel is filled by the emulsion that is prepared as described in section 6.1, taking care that no air bubbles are trapped inside during the initial filling. At first, the position in the x-y plane of the center of the channel is determined in bright field using a lower magnification (4× or 10× objective) by measuring the distance form the walls or centering the roughness pattern in the Region of Interest (ROI). To reconstruct the flow profile we ran z-scans over the entire channel height (H) starting from the smooth wall and proceeding towards the rough wall. For a precise determination of the bottom and top walls, white light is turned off and the DPSS laser is switched on. In this configuration is easier to focus the tracers an set the z_{bottom} and the z_{top} value. We set exposure times and the frame rate (FPS, frame per second) to acquire μ-PTV images with no blurry tracers.

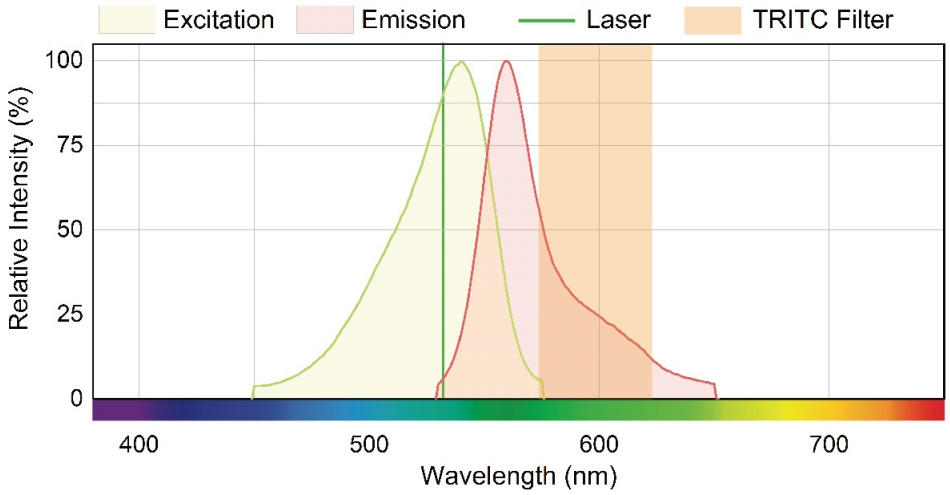

Figure 6.11: Fluorescence excitation and emission spectra of FluoSpheres orange fluorescent microspheres in H_2O as a function of the wavelength (nm). In the graph are also reported the laser wavelength and the TRITC filter bandwidth.

We then turn on the pressure controller and we ran z-stack acquisition with 2 μm steps to avoid velocities correlation between two neighboring planes. For each plane we collected a stack of 500 images at a frame rate up to 3500 fps ($\sim$0.3 ms). The next section describes the analysis software used to reconstruct the flow profile.

§ 6.4. Image Analysis - Particle Tracking Velocimetry

To extract the velocity profiles we analyze the z-stack sequences, collected by microscope, with a custom made program based on TrackMate algorithm [176]. The analysis steps are described below and summarized in fig. 6.12. The Python code is reported in Appendix A.

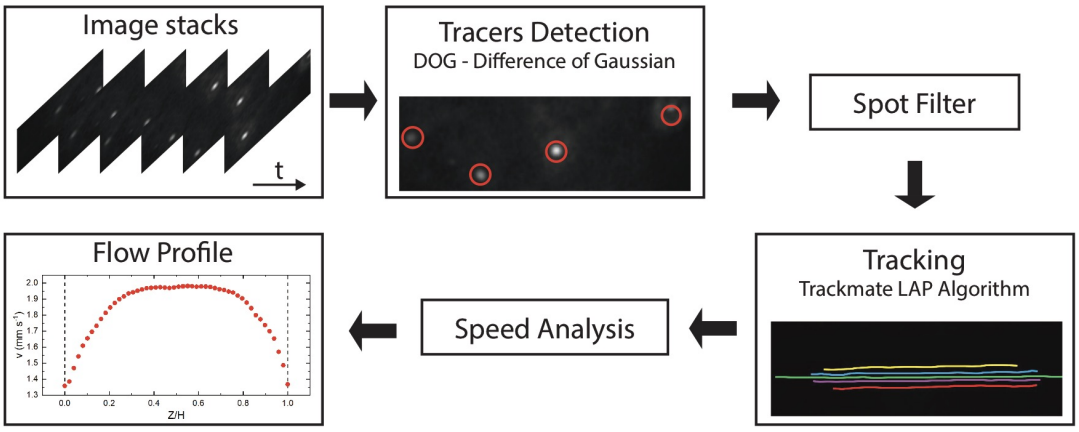

Figure 6.12: Diagram representing the analysis steps from collected images to reconstructed flow profile.

1. **Tracers detection**: In the first step the program detects the tracers that are visible in the image as a white spots. The detection is done with a Difference of Gaussian (DoG) algorithm. This detection process require as input parameters the estimated particle diameter and a threshold value to distinguish the dark/bright border.

2. **Spots Filter**: Detected spots are then filtered; just tracers that have a *quality* greater than a threshold value are considered by the tracker. The *quality* is calculated automatically by the software and take account of the bright spots, how much the spot diameter is close to the specified diameter and the edges sharpness.

3. **Tracking**: The tracking algorithm is based on a simple LAP (Linear Assignment Problem). The tracker uses only three configuration fields to compute the tracking: i) *Linking Max Distance* defines the maximal allowed linking distance. This value limits the spatial search range for candidate matching spots. ii) *Gap-Closing Max Distance* defines the maximal distance for gap-closing. If the value is low two track segments will not be bridged if the last spot of the first segment is further away than the first spot of the second segment. iii) *Max Frame Gap* deals with the detection of gap-closing events, and sets the maximal frame interval between two spots to be bridged.

4. **Speed Analysis**: The tracker completes the analysis calculating the mean velocities of each tracks in the sequence. Another filter considers the only tracers that display at least 30 displacement in the sequence. Only these are used to calculate the average flow velocity $v_{flow}(z)$, at the selected stack z.

5. **Flow profile analysis**: the previous steps are repeated for each plane. Adding all the velocities we then reconstruct the entire flow profile inside the channel. An example is reported in the bottom-left panel of fig. 6.12.

From the flow profile we can collect a large number of information about the emulsion flow. We can easily obtain the slip velocities v_{slip} at the bottom/top wall of the channel or the velocity in the middle v_{plug}. Moreover with few math steps we can calculate the local rheology inside the channel (i.e shear rate, $\dot{\gamma}$ and the stress, σ).

7. Results

In this Chapter we report the results regarding the effect wall roughness on the flow of a dense emulsion in a microfluidic channels. In our study we systematically investigate the effect of controlled roughness providing the first direct evidence that plastic rearrangements of droplets are all coordinated around rough elements. Moreover, by a fine tuning of the roughness, we can predict and control the fluidization of the emulsion. Experimental results are suitably complemented and confirmed by lattice Boltzmann numerical simulation. These numerical simulations are key to highlight the change in the spatial distribution of plastic rearrangements caused by the surface roughness and to elucidates the micro-mechanics of the yielding scenario via an unprecedented statistical analysis of the droplets displacements close to rough wall.
This Chapter is organized as follow. The main differences in the flow of concentrated emulsion respect to Newtonian fluid are illustrated in section 7.1. Then, in section 7.2, we present the effect of surface roughness on the flow of dense emulsion. In particular we discuss the effect of straight grooves in the activation of plastic rearrangements and the consequent fluidization process. In section 7.3 we report the presence of two fluidization scenarios due to different rough elements' density and in the last part of the Chapter (section 7.4) we present the effects of asymmetric roughness having the shape of herringbone pattern.

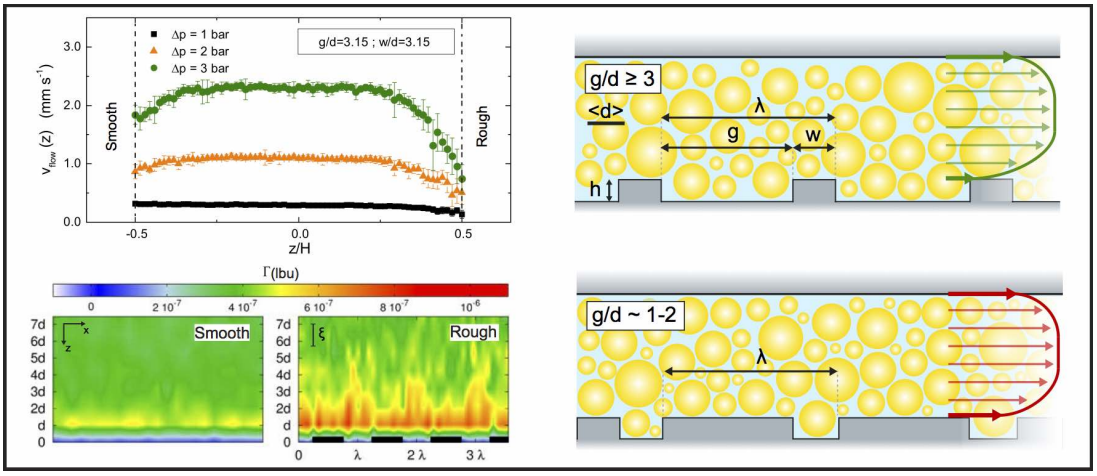

§ 7.1. Smooth Channel

To better understand the complex behavior of dense emulsion in microfluidic channels and the effect of the roughness we performed some preliminary experiments comparing the flow of a dense emulsion (model of SGM) and a common Newtonian fluid. Both fluids were tested in the same microfluidic channel (see fig. 7.1a) presenting smooth walls on both sides (bottom and top). The channel's length (L), width (W) and height (H) are respectively: L=50 mm, W=4 mm and H=120 μm. The flow is driven by a pressure drop $\Delta p = p_{IN} - p_{OUT}$ controlled by a digital manometer. Velocity profiles were reconstructed using micro Particle Tracking Velocimetry. We ran z-scan measurements, collecting image stack along the z axis of the channel with steps of 2 μm. The detailed descriptions of the fabrication process and experimental set-up is described in chapter 6.

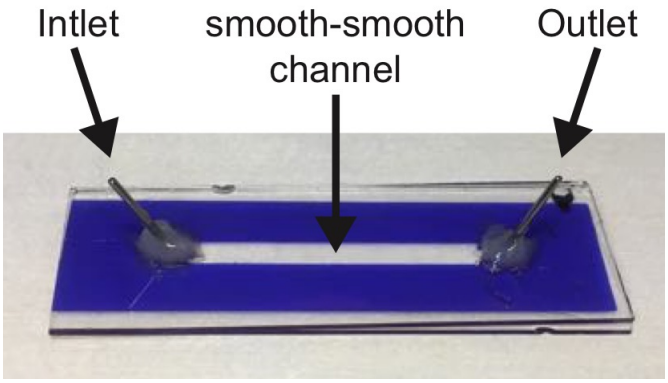

Figure 7.1: Example of the smooth-smooth microfluidic channel.

§ 7.1.1. Newtonian fluid's flow profiles

As Newtonian fluid we use pure glycerol (Sigma-Aldrich, Germany). We perform a rheological characterization with a cone plate rheometer measuring a dynamic viscosity η=1078 Pa·s at 23°C. Reconstructed velocity profiles for different pressure drop are reported in fig. 7.2a. The parabolic shape, more visible for higher pressure drop, is the characteristic mark for Newtonian flow and it is described by the expression

$$v(z) = \frac{\Delta p}{2\eta L}(H/2 - z)z \tag{7.1}$$

This equation allows us to have a relationship for the velocity as a function of the position along the z axis z of the channel. The calculated curves are reported as solid lines in fig. 7.2a. They are un good agreement with experimental data. From the flow profile, it is possible to calculate

the stress $\sigma(z)$ and the shear rate $\dot{\gamma}(z)$ using respectively:

$$\sigma(z) = \sigma_{\text{smooth}} + \frac{\Delta \text{p}}{L}(z + H/2) \tag{7.2}$$

$$\dot{\gamma}(z) = \frac{d}{dz}v(z) \tag{7.3}$$

Local rheological curves are reported in fig. 7.2b. As expected, for a Newtonian fluid the graph shows a linear relationship between σ and $\dot{\gamma}$. In the graph is also reported (red line) the data points measured with the cone plate rheometer.

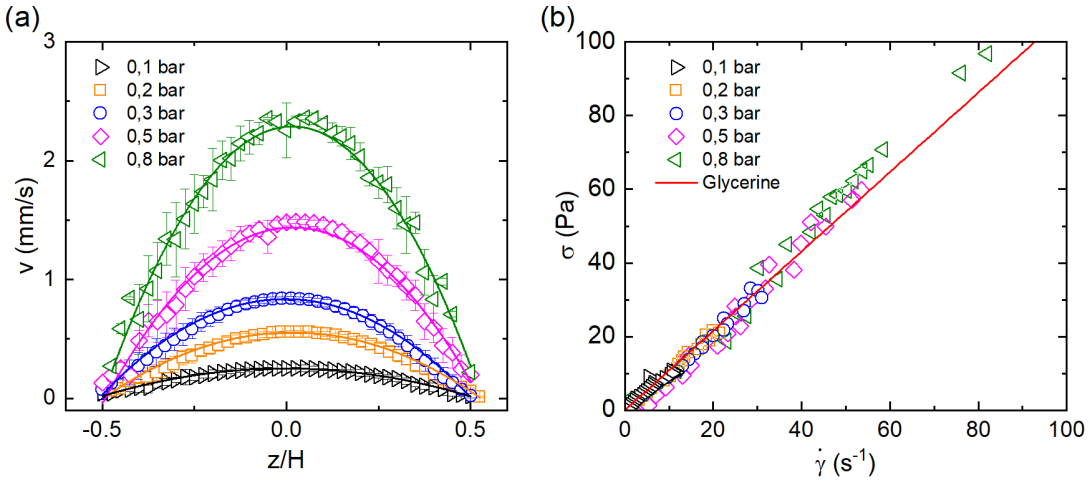

Figure 7.2: (a) Experimental velocity profile as a function of the reduced position in the channel, for pure glycerol. Losses Δp charge applied are: 0,1(▷), 0,2(□), 0,3(○), 0,5(◇), 0,8(◁) bar. Solid lines refer to calculated flow profile from eq. (7.8). (b) Local rheology curves derived from velocity profile, varying pressure drop. the order of the symbol is the same as the speed profile. Red line refers to pure glycerol measured by cone plate rheometer.

§ 7.1.2. Dense Emulsion's flow profiles

As model of Yield Stress Fluids we used a concentrated oil-in-water emulsion prepared by mixing Silicone oil (dispersed phase) and a mixture of glycerol and water (continuous phase), as described with more detail in Chapter 6. The emulsion was optically transparent and non-adhesive. The mean diameter of the emulsion was $d = 4.75\,\mu$m with a polydispersity index (coefficient of variance) of 0.61. We diluted the stock emulsion at three different volume fractions respectively: $\phi = 0.80$, $\phi = 0.85$ and $\phi = 0.875$ all three are above the jamming point ($\phi_J = 0.64$). The rheology of the emulsion, characterized by a cone plate rheometer, exhibits an yield stress behavior. The rheology curves follow the Herschel-Bulkley law $\sigma = \sigma_0 + A\dot{\gamma}^n$, with parameters summarized in table 7.1.

The graph of fig. 7.3a report experimental flow profiles of dense emulsion with a volume fraction ϕ=0.80 for three different pressure drop. Respect to the Newtonian case, where the flow profiles show a parabolic shape, emulsion velocity profiles present a "plug" region in the center of the

Table 7.1: Parameters for the bulk rheological flow curves according to the Herschel-Bulkley model $\sigma = \sigma_0 + A\,\dot{\gamma}^n$, for various volume fractions Φ of the emulsions.

Volume fraction Φ	σ_Y (Pa)	A ($\mathrm{Pa\,s^{1/2}}$)	n
0.875	55.14	31.41	0.5
0.85	40.99	27.82	0.5
0.80	22.16	19.91	0.5

channel, as observed by Goyon *et al.* [11] and described in Chapter 1. In this region, the applied shear stress is below the Yield stress ($\sigma(z) < \sigma_0$) and its values is not enough to fluidized the emulsion. Hence, the emulsion flows compact as a solid, showing a constant velocity (i.e., a flat velocity profile). By increasing the applied pressure drop the shear stress inside the channel increases and the flow profiles partially recover the classical Poiseuille profile, yet they display a plug region in the center. The yield stress value varies with the volume fraction ϕ; higher is the volume fraction, higher is the value of σ_0. Hence, at a fixed pressure drop it is more difficult to make the emulsion flow. The effect of the volume fraction is showed in fig. 7.3b where the flow profiles for three different volume fractions, respectively $\phi = 0.80$, $\phi = 0.85$ and $\phi = 0.875$, at a fixed pressure drop Δp=3.0 bar are reported. Only the lowest volume fraction ($\phi = 0.80$) shows a developed profile, while in the others two ($\phi = 0.85$, $\phi = 0.875$) the plug regions cover the entire channel.

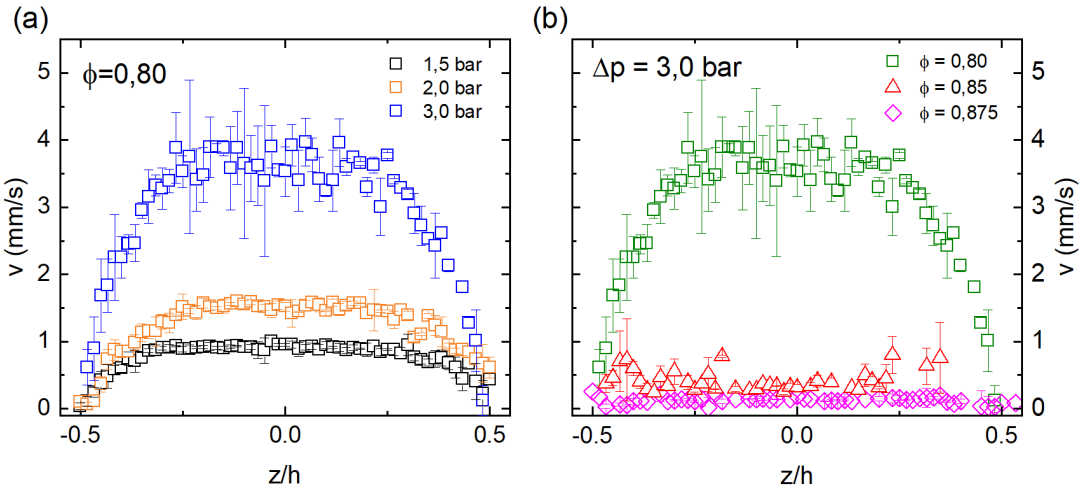

Figure 7.3: (a) Experimental velocity profile as a function of the reduced position in the channel, for a dense emulsion. (a) Emulsion with fixed $\phi = 0.80$ for different pressure drops. (b) Flow profile at fixed pressure drop Δp = 3 bar at different volume fractions.

Conclusions

- From the velocity profiles it is possible to obtain local rheological information about the flowing fluid.
- For a Newtonina fluid (glycerine) the flow profiles show the typical parabolic shape described by Poiseuille model for parallel plates geometry.
- For a dense emulsion the flow profiles show a plug region, characteristic of Yield stress behavior.

§ 7.2. Smooth-Rough channel

The flow of a dense emulsion, a classical example of soft glassy materials, is characterized by a succession of elastic deformation of the microstructural constituent (e.g. droplets) and subsequent plastic rearrangements which release the accumulated elastic stress [130, 180]. Experimental studies report that roughness can change the material structural properties, trigger and promote rearrangements. To study and characterize the roughness effect we designed a dedicated microfluidic channel with a smooth wall opposed to a rough wall allowing us to compare the slip velocities and roughness-induced fluidization on smooth and rough walls in the same channel under the same flow conditions. Microfluidic devices were fabricated by multilayer photolithography using SU-8 photoresist on glass as detailed described in section 6.2. The microfluidic channel had a width W of 4 mm, height H of 220 μm and length L of 4.5 mm. Controlled roughness was provided by an array of rectangular posts of width w, gap g and periodicity $\lambda = w + g$, extending over the whole width of the channel (see bottom zoom of fig. 7.4). The posts are orientated perpendicularly to the direction of the flow and have heights of $h \approx 2.5$ μm somewhat smaller than the droplets diameter, so the effect of plastic activity is pronounced [19]. As already describes, only one face of the channel was patterned ($z = H/2$), the other glass was smooth ($z = -H/2$) as shown in fig. 7.4. We performed the experiments with the same emulsion used in the previous section and with the same experimental set-up. The flow profiles were reconstructed using micro Particle Tracking Velocimetry, measuring the liquid velocity at different channel height.

§ 7.2.1. Numerical model

Experimental results are complemented with numerical simulations of a model of emulsion based on the lattice Boltzmann method [181] performed by Prof. M. Sbragaglia and Dr. M. Lulli (University of Rome "Tor Vergata"). The lattice Boltzmann methodology gives direct access to the hydrodynamical variables (expressed in this paper in lattice Boltzmann units, lbu), specifically velocity and stress fields, which are useful to construct the fluidity fields. All the numerical simulations have been carried out in two dimensional (2D) domains $L_x \times H$. The wall-to-wall gap H

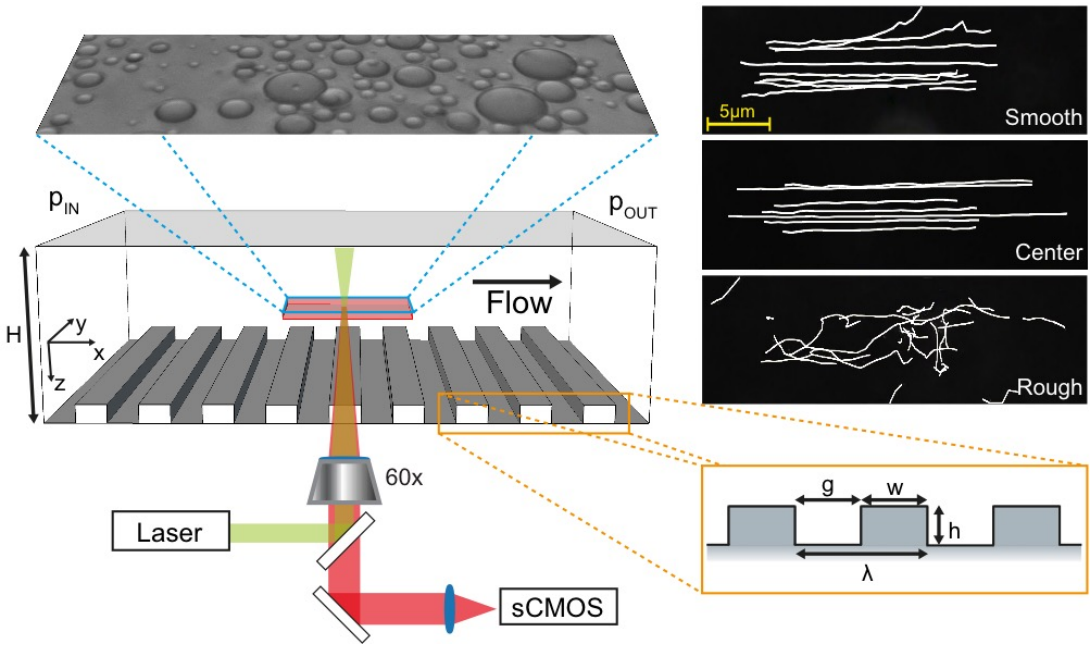

Figure 7.4: Experimental setup used for flow visualization of dense emulsions. The flow is driven by a pressure drop $\Delta p = p_{IN} - p_{OUT}$ through a microfluidic channel of height H, one wall of which is patterned with a controlled roughness. Black backgrounded snapshots show the trajectories of fluorescent nanoparticles suspended in the continuous phase of the emulsion, flowing at different channel height z: close to the rough wall (bottom snap), in the center of the channel (middle snap, corresponding to the plug region) and close to the smooth wall (top snap).

is resolved with 512 grid nodes. With a single droplet diameter resolved with roughly 30-35 lbu, we are able to accommodate roughly 14 droplets in the wall-to-wall gap H. Periodic boundary conditions are applied in the stream-flow (x) direction and the length L_x has been resolved with a variable number of grid nodes, also depending on the value of λ used. A complete wetting (zero contact angle) condition for the continuous phase is adopted, which results in a non-zero slip velocity for the droplets in contact with a smooth wall. This slip velocity is suppressed by the surface roughness [20, 21], thus allowing the study of the variation of the slip velocity between smooth and rough walls [182]. the major novelty brought in by numerical simulations consists in the possibility of accessing simultaneously the flow profiles and the plastic rearrangements of the droplets, something that is not possible in our experiments. With respect to earlier work, the technical novelty is a procedure to detect plastic rearrangements in geometries with arbitrary boundary complexity [183]. Briefly, what we do is comparing two consecutive configurations by using the corresponding Delaunay triangulations [184] built starting from the centers of mass of the droplets. The implementation allows to constrain the triangulation boundary to any given geometry so that it is possible to collect the data related to the events inside the grooves of the channel as well. The triangulation provides the nearest neighbors of each droplet while maximizing the minimum angle of all triangles with respect to other possible triangulations. A topological change (plastic rearrangement) takes place every time a link between two droplets disappears, for boundary events, and a new one appears for bulk events (see fig. 7.5). then, one

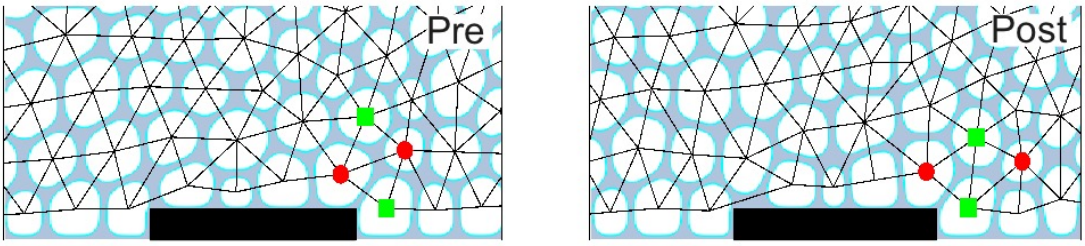

Figure 7.5: Plastic rearrangements are identified by comparing the Delaunay triangulations of two consecutive configurations.

can count the total number of plastic rearrangements $N_{\text{plastic}}(\vec{x})$ in such a localized region. The local rate $\Gamma(\vec{x})$ follows

$$\Gamma(\vec{x}) = \frac{dN_{\text{plastic}}(\vec{x})}{dt} \tag{7.4}$$

The number of plastic rearrangements is directly connected to the fluidity field (f) of the material. The relation is described by the Kinetic Elasto-Plastic model (KEP) where Γ is proportional to the fluidity ($\Gamma \propto \mathcal{A}f$) with a proportional constant $\mathcal{A}$ related to the elastic modulus of the material [5, 11].

§ 7.2.2. Dependence on periodicity

In this work we are interested in how the roughness structure affects the flow in comparison to smooth wall. Experimental flow profiles are showed in fig. 7.6. The measured velocity profiles $v(z)$ exhibits the characteristic plug region in the center of the channel and the shearing regions at the walls, with non-vanishing slip velocities. We observed the presence of a difference on the wall slip velocities between the smooth and the rough walls as show in fig. 7.6a. This difference was not present in the smooth smooth channel where both wall slip velocities were equal. We define the wall slip difference $\Delta \mathrm{v}_{\text{slip}}$ as

$$\Delta \mathrm{v}_{\text{slip}} = \mathrm{v}_{\text{smooth}} - \mathrm{v}_{\text{rough}} \tag{7.5}$$

where $\mathrm{v}_{\text{smooth}}$ and $\mathrm{v}_{\text{rough}}$ are the wall slip velocities in contact with the smooth ($z = -H/2$) and rough ($z = H/2$) wall respectively. The latter values were determined by fitting the last four data points of the μ-PTV measurement in proximity of the walls.
Since the channel walls are hydrophilic, they are wetted by the continuous phase of the emulsion, while the droplets slide on them. Once the shear stress exceeds the yield stress of the emulsion, σ_0 (which depends on the volume fraction) the emulsion undergoes plastic rearrangements. We point out that the shear stress on the two walls (smooth and rough) may differ because of the asymmetric character of the channels. Stress distribution may then be also asymmetric, albeit linear as we will discuss later. By increasing the applied pressure drop, the flow profiles partially recover the classical Poiseuille profile, yet they display a plug region in the center, characteristic of yield stress fluids (low shear regions where $\sigma(z) < \sigma_0$) as showed in fig. 7.6a. In addition,

fig. 7.6a shows that by increasing the pressure drop, Δv_{slip} increases.

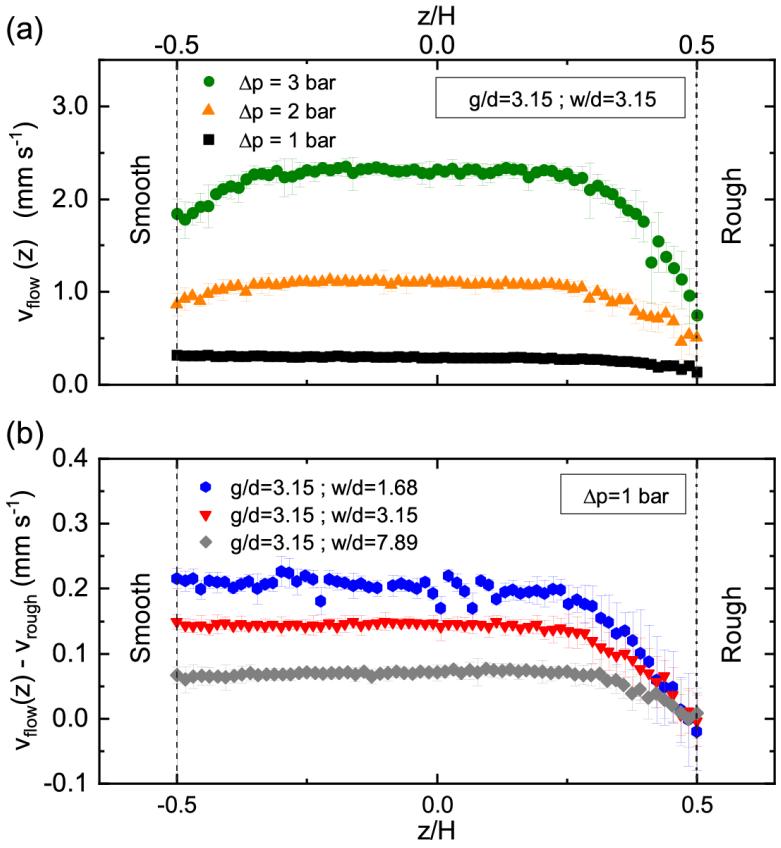

Figure 7.6: Flow profiles $v_{flow}(z)$ in a smooth-rough microchannel for different pressure drops (a) and at fixed pressure drop for different surface roughness (b). In the latter case the slip velocity on the rough wall v_{rough} has been subtracted.

By keeping the gap g fixed and changing the widths of the post w, we observed a systematic evolution in the flow profiles: increasing the periodicity $\lambda = g + w$ led to a smaller fluidization (i.e., velocity gradient) and consequently smaller Δv_{slip} as reported in fig. 7.6b. From the micro-mechanical point of view, the observed decrease of v_{rough} (with respect to v_{smooth}) can be accounted for the increased number of plastic rearrangements [5, 11, 16]: droplets encountering the rough elements (gaps, posts) change their speed and often also their direction causing a scramble with their neighbors, whereas their falter on the smooth wall is rather occasional and almost absent in the plug region. This is clearly visible in the three black backgrounded snapshots of fig. 7.4. The white lines correspond to the recorded tracks of tracers suspended in the continuous phase of the emulsion at three different channel height z. Starting form the top (smooth wall) tracks do not show large segmentation meaning that the number of plastic rearrangements are low. Tracks are even more straight in the center of the channel (center snap) where the rearrangements are almost absent. Finally in the bottom snap (rough wall), tracks are fragmented confirming that the number of rearrangements are higher than near the smooth wall. The observed experimental behaviors illustrated in fig. 7.6 were actually well reproduced by numerical simulations, as reported in fig. 7.7a, b, where the corresponding rates of plastic

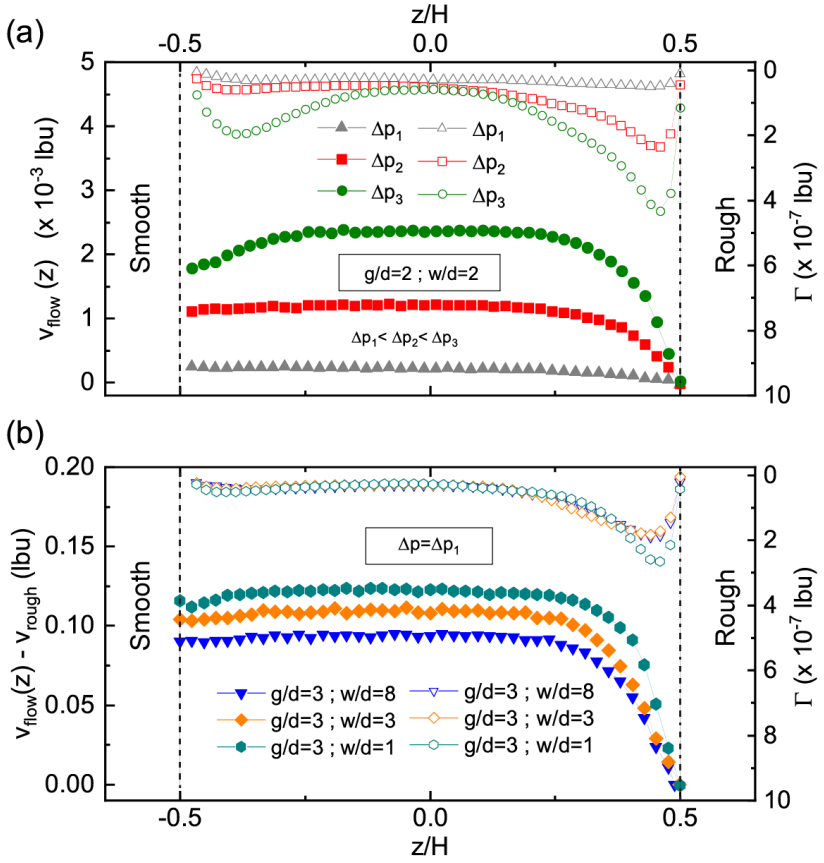

Figure 7.7: Flow profiles (solid symbols) and rate of plastic rearrangements (empty dots) Γ eq. (7.4) from numerical simulations based on the lattice Boltzmann methods. (a): velocity profiles and the associated Γ for a fixed roughness and increasing pressure drop Δp. Data at fixed Δp for different roughness are also displayed (b). Slip velocities at the rough walls are negligible for geometry $g/d = 3$; $w/d = 1$, while they are 10^{-4} and 2.5×10^{-4} for geometries $g/d = 3$; $w/d = 3$ and $w/d = 8$ respectively.

rearrangements are also displayed (empty dots). These figures clearly show that both the asymmetry of the profiles at fixed roughness (fig. 7.7a) and the different fluidization properties at fixed pressure drop (fig. 7.7b) have a direct correspondence to the rate of plastic activity, with the latter being more pronounced at high velocity gradient. Hence, the rough wall enhances the number rearrangement inside the emulsion. This is further highlighted from fig. 7.8 that reports the spatial distribution of plastic rearrangements in the simulations with Couette geometry. For the smooth wall the rate of plastic rearrangements, Γ, is relatively small and rather homogeneous along the flow (x direction); this contrasts the case of a rough wall, where Γ is enhanced, with a periodic modulation dictated by the roughness. Furthermore the figure shows that the rate of rearrangements is significantly increased in the wells and not on the top of the bumps.

Experimental results are supported by numerical lattice Boltzmann numerical simulations [21, 185, 186]. These allow to access simultaneously the flow profiles and plastic rearrangements. It is important to discuss whether the different degrees of fluidization can be described by a

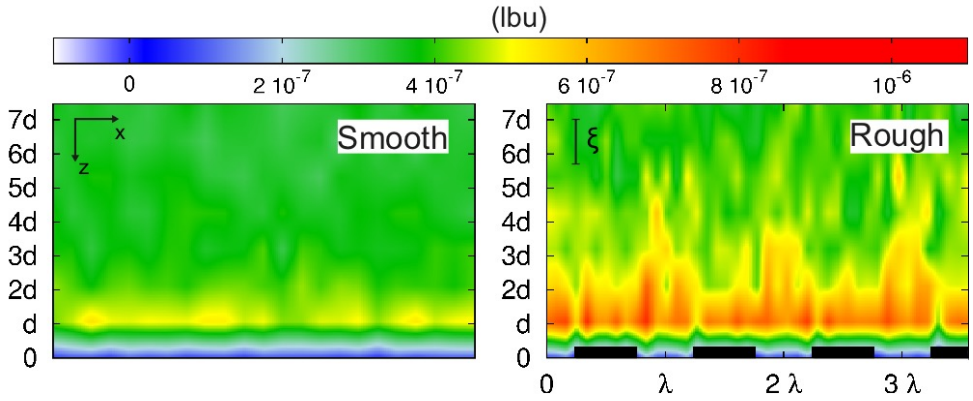

Figure 7.8: Spatial distribution of Γ in a Couette geometry, highlighting the properties of a sheared layer close to smooth and rough walls. The distance from the wall shown in units of the mean droplet diameter. Data are reported in lattice Boltzmann units (lbu).

unique shear-stress relationship. This requires an accurate knowledge of the shear stress profile. In conditions where the velocity profile is symmetric, because the two walls are either both rough or both smooth, the shear stress profile is a linear function of z and it is easily computed from the pressure drop, yielding the same (in absolute value) stress at the two walls ($z = \pm H/2$) [5, 11]. When the channel geometry is asymmetric, the corresponding stress profile is still linear as described by eq. (7.2). However, the wall stresses are different, and the wall stress on the rough side is larger. This is both confirmed experimentally and numerically as shown respectively in fig. 7.10a, b. Both graphs report the absolute values of the stress profile $|\sigma(z)|$ as a function of the reduced channel height for smooth-smooth and smooth-rough channels. Experimental data are calculated from velocity profiles, reported in the inset of fig. 7.9a. The relative stress curves calculated using the Herschel-Bulkley relationship is showed in fig. 7.10.

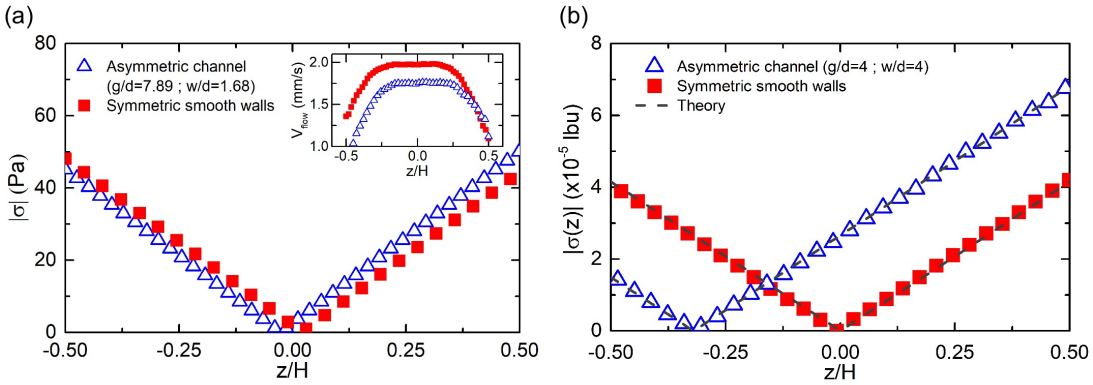

Figure 7.9: Stress profile for symmetric channel with smooth walls on both side $z = \pm H/2$ and for asymmetric channel with a smooth from one side ($z = -H/2$) and a rough wall on the other side ($z = +H/2$). Curves are calculated from experiment (a) and from lattice Boltzmann numerical simulation (b).

Being the wall stress larger, one could explain the increase of fluidization by invoking the Herschel-Bulkley relation without considering cooperativity. On the other hand, we also found

evidences of cooperativity behavior. To show that, we repeated the numerical simulations in a Couette geometry. In this geometry, the fluidity model can be solved exactly [5, 11, 123] al-

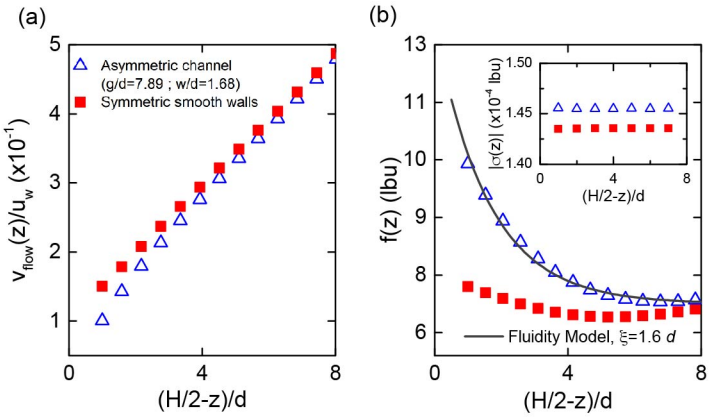

Figure 7.10: (a, b): velocity and fluidity profiles for a Couette geometry obtained by applying a constant wall velocity u_w at the wall in $z = -H/2$ for the two channel configurations used in fig. 7.9. The inset of (b) reports the stress profile as a function of the distance from the wall in $z = +H/2$. Data are reported in lattice Boltzmann units (lbu).

lowing to measure the cooperativity length ξ via the analysis of the velocity and stress profiles. Indeed, in a steady Couette flow, the stress is spatially constant, and an exact calculation [5] for a Dirichlet-type boundary condition leads to the fluidity profile as a function of the distance from the rough wall in $z = +H/2$

$$f(z) = f_b(\sigma) + (f_w - f_b(\sigma))\, e^{(z-H/2)/\xi} \tag{7.6}$$

where we have assumed that the wall in $z = -H/2$ is smooth (i.e., $f(-H/2) = f_b(\sigma)$) and that $H \gg \xi$. The quantity f_w is the wall fluidity [5, 11] which parameterize the effects of the roughness. The wall-to-wall distance was chosen to be $H \approx 16\,d$ and we kept fixed the nominal shear by applying a constant velocity u_w at the smooth wall in $z = -H/2$. We then performed different simulations by changing the nature (i.e., smooth or rough) of the wall in $z = +H/2$. The resulting stress was studied as a function of the distance from the wall in $z = +H/2$ and was found to be spatially constant separately in each simulation; this constant value was larger in presence of roughness as showed in the inset of fig. 7.10b. When the wall in $z = +H/2$ was smooth, the flow profile was essentially a linear one with a slip velocity, resulting in a rather constant fluidity throughout the channel. When the wall in $z = +H/2$ was rough, the slip velocity was reduced and the wall fluidity was increased [21]. This produced a local viscosity (i.e., the inverse of the fluidity) that was smaller when close to the rough wall, and the effect spread over a distance $\xi \approx 1.6\,d$ from the wall, in agreement with eq. (7.6) and with other observations [5, 11, 20, 21]. In summary, the rough walls enhance the shear stress triggering a cooperative behavior which protrudes into the channel over a distance proportional to the cooperativity length.

To further characterize the effect of roughness periodicity and quantify the asymmetry in the velocity profiles we considered Δv_{slip} as a function of λ. Results are reported in see fig. 7.11a show a clear evidence that, for a fixed pressure drop, Δv_{slip} scales with the periodicity of the roughness

$$\Delta v_{slip} \sim K\lambda^{-1} \tag{7.7}$$

where the prefactor K is found to increase with the applied pressure drop. This may be taken into account by further normalizing Δv_{slip} for a characteristic velocity dependent on the pressure drop. To this aim, we calculated the maximum (plug) velocity v_{plug} by averaging the measured velocities in the 8-10 droplet diameter region in the center of the channels ($z \simeq 0$). The dependence of plug velocities as a function of the pressure drop is reported in the inset of fig. 7.11b. Upon rescaling with v_{plug}, the individual scaling curves nicely collapse into a single master curve as reported in fig. 7.11b.

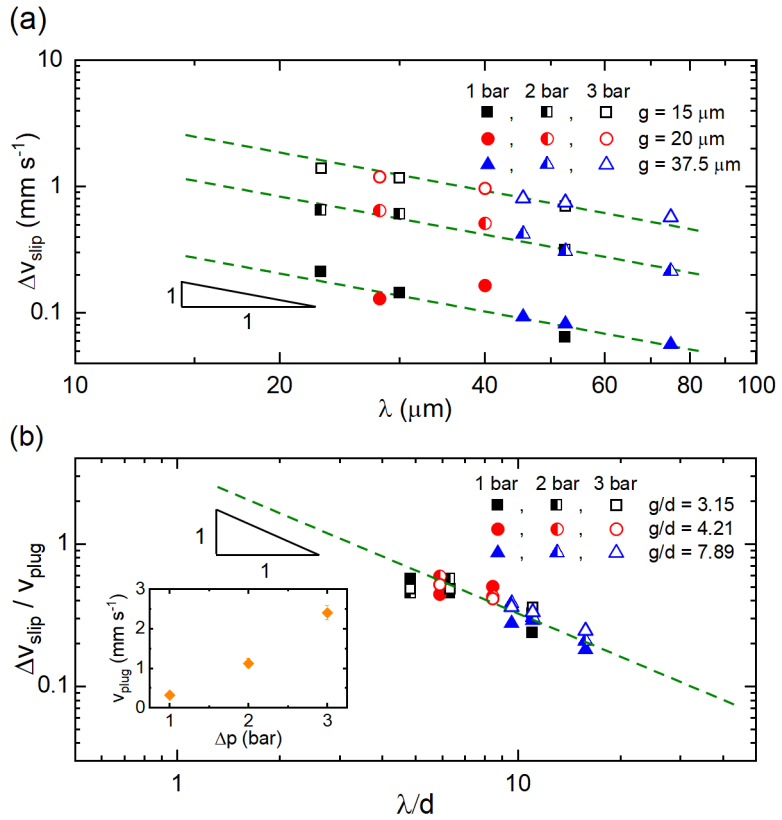

Figure 7.11: (a) Difference of the slip velocities eq. (7.5) as a function of the roughness periodicity $\lambda = w+g$ for different pressure drops Δp and different gaps g. Dashed lines are guides for the eyes with slope -1. (b): Difference of the slip velocities, normalized by the maximum (plug) velocity v_{plug}, as a function of the wall roughness periodicity λ in units of the mean droplet diameter d. Dashed line is a guide for the eyes with slope -1. Inset shows the dependence of v_{plug} with Δp.

Finally, fig. 7.12 shows the relation between the numerical Δv_{slip} and the rate of plastic rearrangements. Again simulations in a Couette geometry for both smooth and rough channels were performed. The results of numerical simulations confirm the observed experimen-

tal scaling $\Delta v_{slip} \sim \lambda^{-1}$ (inset of fig. 7.12). Moreover, we computed the increase of the rate of plastic rearrangements (due to the rough wall) with respect to the case with a smooth wall, $\Gamma_{TOT} = \frac{1}{4}\int(\Gamma_{rough}(\vec{x}) - \Gamma_{smooth}(\vec{x}))\, d\vec{x}$, and observed a linear relation between Γ_{TOT} and $\Delta v_{slip} = \int dz(\dot{\gamma}_{smooth} - \dot{\gamma}_{rough})$, $\dot{\gamma} \propto f$. This result further indicates that the induced fluidization is related to plastic rearrangements; specifically, its increase in the Couette geometry scales linearly [123] with respect to the number of plastic rearrangements, for different rough wall realizations.

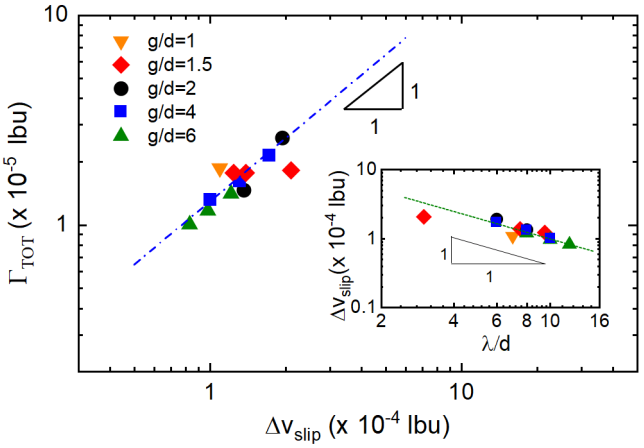

Figure 7.12: Lattice Boltzmann simulation results for the increase of the rate of plastic rearrangements induced by the rough wall, Γ_{TOT} (see text for details). Γ_{TOT} is plotted as a function of the slip variation Δv_{slip} eq. (7.5). Dashed-dotted line is a guide for the eyes with slope 1. The inset reports the slip variation as a function of the dimensionless period λ/d. Dashed line is a guide for the eyes with slope -1. Data are reported in lattice Boltzmann units (lbu).

Conclusions

- Introducing a controlled roughness, consisting in an array of transversal microgrooves placed on one wall of the channel, we observe a difference in the wall slips between the smooth and rough rourfaces.
- With the help of numerical simulation we justify the wall slip difference to the different number of plastic rearrangements near the two walls. The plastic activity is higher in the rough wall than in the smooth wall.
- Surface roughness can trigger plastic rearrangements inducing a more efficient fluidization in the material.
- We find a direct corrispondence between the wall slip difference and the periodicity of the roughness.

§ 7.3. Gaps effect: from stiff to soft roughness

In previous sections we tested channels with different density of rough elements finding a that the difference of wall slip velocities scales with the inverse of the roughness periodicity λ as described by eq. (7.7). The single master curve of fig. 7.11 suggests a common scenario for roughness structures having wide gaps. For gaps of at least several ($g/d > 3$), the observed decrease of v_{rough} (with respect to v_{smooth}) and the associated scaling laws can be explained in terms of *"get-in-get-out"* scenario. Flowing droplets fell into the grooves (gaps), scramble with and push out a neighboring droplet and change their speed. After that they get out of the grooves easily (more precisely pushed out by a forthcoming neighbor), while triggering plastic rearrangements, which protrude into the channel by a distance on the order of the cooperativity length. The larger is the density of grooves (i.e., the smaller is λ) and the larger is the fluidization. However, this gain of fluidization does not proceed indefinitely as λ decreases. Indeed if the gap is reduced below $2d$ a loss of fluidization is registered (i.e., smaller slip velocity difference). Then, as λ is further decreased, the fluidization starts increasing again, following the same scaling with respect to the grooves' periodicity λ. Data collapse over two master curves with the same power-law dependency on λ, however the two different perfactors are associated to two different pathways of wall fluidization as shown in fig. 7.13a. The graph reports the difference of the wall slip velocities, normalized by the v_{plug}, as a function of the roughness periodicity λ in unit of the mean droplet diameter d for three pressure drop at fixed volume fraction.

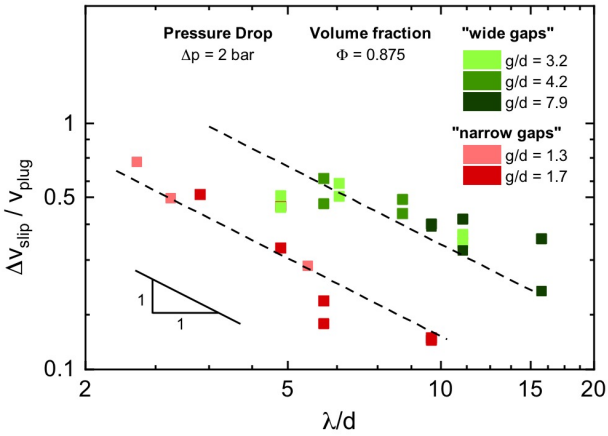

Figure 7.13: Difference of the wall slip velocities eq. (7.5), normalized by the maximum (plug) velocity v_{plug}, as a function of the wall roughness periodicity $\lambda = g+w$ in units of the mean droplet diameter d, for different pressure at fixed volume fraction ϕ=0,875. Green colored symbols refer to wide gaps $g/d \geq 3$ and red scaled symbols refer to narrow gap $g/d \approx 1-2$. Dashed line are guides for the eyes with slope -1.

Beyond the *"get-in-get-out"* scenario for wide gaps ($g/d \geq 3$), another new scenario emerges for narrow gaps ($g/d \simeq 1-2$), wherein Δv_{slip} still scales with λ^{-1}, but the scaling is shifted to a lower curve, i.e., $K_{narrow} < K_{wide}$. The scaling in λ suggests that we still have to do with periodically modulated sources of fluidization; however, the smaller prefactor indicates that the sources of

fluidization are somehow weakened. We argue this as *"trapping"* scenario, where droplets get trapped into the grooves and cannot escape easily, thus forming periodically repeated "soft obstacles" [20]. The lower slip velocity difference suggests that such soft obstacles induce plastic rearrangements and related fluidization to a smaller extent with respect to the solid ones. The two scenarios are depicted in fig. 7.14.

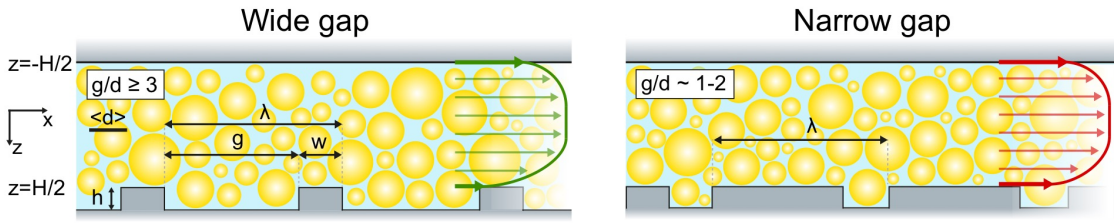

Figure 7.14: Difference of the wall slip velocities eq. (7.5), normalized by the maximum (plug) velocity v_{plug}, as a function of the wall roughness periodicity $\lambda = g+w$ in units of the mean droplet diameter d, for different volume fraction Φ at fixed pressure drop Δp. Green colored symbols refer to wide gaps $g/d \geq 3$ and red scaled symbols refer to narrow gap $g/d \simeq 1-2$. Dashed line are guides for the eyes with slope -1.

It is necessary to note that the "trapping" is expected to be temporary since the post height is slightly below the critical value $h_{crit} = d/2$, which, according to previous study [19], should lead to constant no-escape scenario and increased fluidity. However, the time of entrapment is much longer than the typical flow time (*i.e.* the time necessary for a droplet to flow over a single roughness unit $g+w$), thus the periodic soft obstacles interrupt the flowing of the droplets layer less frequently. Moreover, due to the relatively high polydispersity of the emulsion, the formed soft obstacles should have somewhat random heights. Thus the temporary character of droplets entrapment together with the polydispersity of the emulsion led to the formation of an ever changing soft/elastic asperities with fluctuating heights, and the local slip velocity (and slip velocity difference) fluctuates accordingly. Indeed, for wide gaps, repeated experiments led to the same (or very similar) Δv_{slip} values, whereas for narrow gaps the measured slip velocities on the rough wall (and the resulting Δv_{slip} values) from repeated experiments showed relatively large oscillations (see fig. 7.13).

Numerical simulations help us to highlight the differences between the two scenarios. We looked at the fluidity profiles $f = \partial_z v/\sigma$, with σ the stress in the system (a constant for the Couette cell). Results are displayed in fig. 7.15, where we report the fluidity profile averaged along the stream-flow direction and displayed as a function of the distance from the rough wall. Notice that a coarse-graining at the droplet diameter scale was carried out, which naturally becomes the length at which we observe fluidity variations.

While for a smooth wall the fluidity profile (light blue line) stays essentially constant across the channel (only a slight increase is detected close to the solid wall), for wide gaps the fluidity is remarkably enhanced, reaching a peak close to the wall, $z_{peak} \approx d$, and monotonously decays towards the bulk regions (green lines). This is a clear signature of a cooperative behavior, in

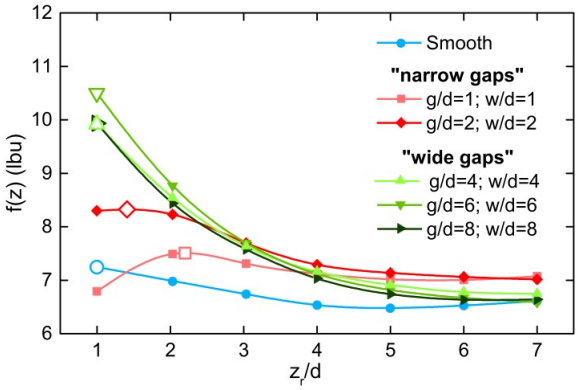

Figure 7.15: Lattice Boltzmann numerical results for the fluidity field averaged along the flow direction x as a function of the distance $z_{\mathrm{r}} = H/2 - z$ from the rough wall, measured in units of the mean droplet diameter d. The fluidity is measured in lattice Boltzmann units (lbu). The larger open symbols indicate the location where the fluidity attains its maximum value.

agreement with the solution of the non-local fluidity equation

$$f(z) = f_{\mathrm{b}}(\sigma) + \xi^2 \partial_{zz} f(z) \tag{7.8}$$

where ξ measures the spatial extension of plastic rearrangements, while $f_{\mathrm{b}}(\sigma)$ is the bulk fluidity [5, 11]. The novelty in fig. 7.15 is the quantitative comparison of fluidity profiles for different realizations of the gaps. For the narrowest gap (red lines), the fluidity profile is found to be non-monotonous, in contrast with the observation for wider gaps. One may consider the location of the peak as the physical location where the continuum fluidity description provided by eq. (7.8) matches an "effective" boundary condition; if so, then the results in fig. 7.15 show that for the narrower gaps such boundary condition location is offset by roughly 1 droplet diameter with respect to the case with wider gaps. Moreover, with the narrower gaps, the peak value of the fluidity profiles is smaller than the peak value observed for the wider gaps, indicating that the softness of the roughness has less impact in the fluidization of the emulsion close to the wall. Overall, we observe a crossover at a gap value g_c that is of the order of the spatial extension of the plastic rearrangements, here measured to be $\xi/d \approx 1.6$. Notice that the numerical value of ξ is below the corresponding value expected for the experimental emulsions [11]. This can explain why a marked distinction between the two scenarios is clearly observable in the study of $\Delta \mathrm{v}_{\mathrm{slip}}$ *vs.* λ in fig. 7.13, whereas this distinction could not be clearly detected for the few narrower gaps analyzed with numerical simulations.

§ 7.3.1. Dependence of volume fraction

As remarked in the previous discussion, the scaling law is understood in terms of the spatially modulated plastic activity induced by the roughness, which makes the fluidization to scale proportionally to the density of rough elements. Since plastic rearrangements and cooperativity effects are present above the jamming point [5, 11], it is logical to expect this result to hold for different volume fractions above the jamming point. To verify these effects experimentally, we diluted our emulsion to various concentrations. As expected, with decreasing concentration of

the emulsion, the flow velocity increases. Specifically, the plug velocity (plug regime becomes slimmer though), the slip velocities on both walls and the slip velocity differences increase, while obeying the $\Delta v_{slip} \sim \lambda^{-1}$ relationship at each Φ. For each concentration of the emulsion we observed lower values of Δv_{slip} for the narrow gaps, *i.e.* scaling with λ^{-1} but with a smaller prefactor compared to larger gaps $g \geq 3\,d$, indicating that the trapping and get-in-get-out scenarios are robust at changing the emulsion concentration above the jamming point. In fig. 7.16 we plot the slip velocity difference Δv_{slip} normalized by the maximum velocity v_{plug} as a function of the roughness periodicity for different concentration of the emulsion and for different pressure drop. We still observe the presence of two separate groups of data as for fixed volume fraction. The two sets correspond respectively to the scenarios get-in-get-out and trapping.

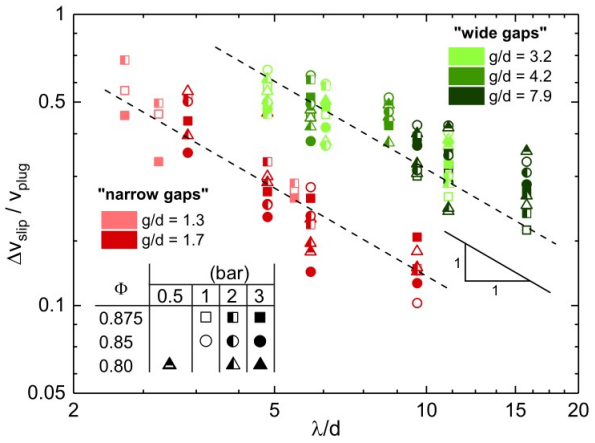

Figure 7.16: Difference of the wall slip velocities eq. (7.5), normalized by the maximum (plug) velocity v_{plug}, as a function of the wall roughness periodicity $\lambda = g+w$ in units of the mean droplet diameter d, for different pressure drop Δp along the channel, and different volume fraction Φ at fixed. Green colored symbols refer to wide gaps $g/d \geq 3$ and red scaled symbols refer to narrow gap $g/d \approx 1-2$.

With numerical simulations we also could visualize in more detail how the peculiar surface yielding scenario changes at changing packing fraction Φ, complementing the experimental observations. The lowest packing fraction analyzed Φ_{low} is roughly located at the jamming point $\Phi_{low} \approx \Phi_{J,2D}$, where the yield stress disappears [5, 11]. For the lowest packing fraction we still observe some large variation of plastic activity in a localized region of thickness $\approx d$ close to the rough wall: these are yielding events caused by droplets hitting against some other droplets that remained blocked into the grooves; however, for distances larger that $1-2\,d$ from the rough wall, the spatial distribution of plastic rearrangements that we observed for the jammed emulsion is totally lost; plastic rearrangements are more homogenized throughout the channel without any clear periodic structure. The change in the surface yielding scenario has direct consequences in the scaling law for the difference of the wall slip velocities: we essentially observed a well defined scaling law for $\Delta v_{slip} \sim \lambda^{-1}$ only for the packing fractions above the jamming point. Whereas at the lower packing fractions no clear evidences of scaling were found, but rather a constant Δv_{slip} as a function of λ emerges. This lends further credit to the idea that the scaling of Δv_{slip} can be accounted by the modulated and periodic increase of plastic rearrangements triggered by

surface roughness above the jamming point, i.e., in a situation where the cooperativity scenario holds [5, 11, 182].

§ 7.3.2. Displacement analysis

To express more quantitatively the difference between the two scenarios outlined above, we report the analysis of the displacement field $\vec{s}_i$, which is given by the difference of the positions of the centers of mass of the i-th droplet in a given time interval δt (see fig. 7.17a, b). The field $\vec{s}_i$ can be obtained in a rather natural way from the numerical analysis proposed in [183], since one needs to identify the same droplet in two different configurations separated by a time distance δt. Hence, defining the position of the center of mass of the i-th droplet at a given time by $\vec{r}_i(t)$, its displacement is simply given by $\vec{s}_i(t) = \vec{r}_i(t + \delta t) - \vec{r}_i(t)$ (see fig. 7.17b), where δt is a time lapse of the order of the droplet deformation time-scale. We then studied the estimator of the probability density function (PDF) of the two components of the displacement field, s_x and s_z, separately. Such an analysis is aligned to the results presented in [16, 124] concerning the larger fluctuations of the local shear rate, $\delta\dot{\gamma}(\vec{x})$, near rough walls. We focused on the displacements of the first row of droplets in contact with the rough wall, *i.e.* the row located at the boundary of the Delaunay triangulation [184] of the droplets centers of mass (see thick purple segments in fig. 7.17a. Such row is actually given by the edges whose ending points only share one neighbor, whereas ending points sharing two neighbors define bulk edges. For comparison, we also report the corresponding results for a smooth wall. In fig. 7.17c, d we show the normalized histograms for the two components of the displacement field. Results can be summarized as follows. *Displacement in the flow direction*: for smooth and wide gaps $p(s_x)$ has a positive most probable value indicating that boundary droplets move according to the flow direction, however the wide gaps PDFs have larger tails because of droplets entering and exiting the grooves experience an *acceleration* with respect to the mean flow, and enhanced negative values due to recoiling events against the stiff obstacles; negative and positive tails are even wider for the narrow gaps PDFs which, together with a vanishing most probable value, indicate that some droplets get trapped in the narrow gaps between stiff obstacles for long times forming a soft roughness with complementary geometry; other boundary droplets can be trapped between such *soft* obstacles which allow large stream-wise oscillations, *i.e.* fat symmetric tails. *Displacement in the cross-flow direction:* for smooth and wide gaps $p(s_z)$ has a vanishing most probable value and it can be considered to a good approximation to be Gaussian for the smooth case (droplets that are pushed against the wall react like harmonic springs along the z direction), whereas negatively skewed fat tails appear for wide gaps signaling that grooves *get-in* events (positive tail) are less abrupt with respect to *get-out* events (negative tail) since droplets are pushed against the stiff spots; for narrow gaps, tails magnitude is roughly the same but they become more symmetric with respect to the wide-gaps ones since droplets are blocked so that *get-in* (positive tail) and *get-out* (negative tail) events are correlated, *i.e.* no droplet gets blocked until another droplet gets unlocked in the same process. For both directions, we observe that the presence of a mean flow is linked to smaller fluctuations.

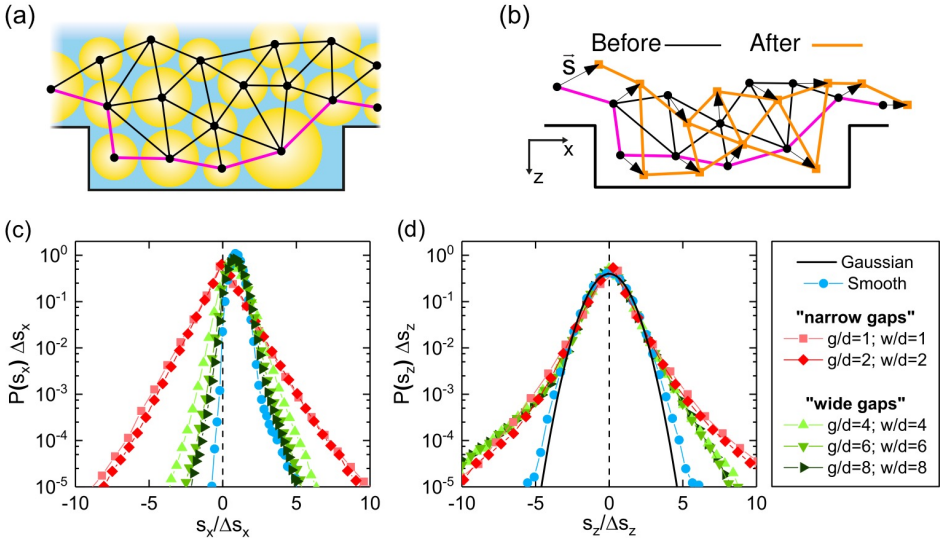

Figure 7.17: (a) Delaunay triangulation [126, 183] constructed from the centers of mass of the droplets (black dots); the triangulation boundary is highlighted in thick purple segments. (b) Displacement field construction: we compare two successive triangulations, *before* (black thin line) and *after* (orange thick line), thus defining the displacements vector field $\vec{s}$ (arrows). (c-d) Estimator of the probability density function (PDF) for the components s_x and s_z of the displacement field of droplets belonging to the triangulation boundary, normalized by the corresponding standard deviations $\Delta s_{x,z} = \left(\langle s_{x,z}^2 \rangle - \langle s_{x,z} \rangle^2\right)^{1/2}$.

Conclusions

- We observe a transition from a fluidization activated by "stiff" roughness to a fluidization activated by "soft" roughness changing the roughness periodicity.
- The fluidization scenarios are descibed by two different rearrangement models labeled as: "get-in-get-out" and "trapping".
- We note that, since plastic rearrangements and cooperativity effects depend on the volume fraction, this effect may be less pronounced at lower concentrations of the emulsion.
- Numerical simulation confirm the presence of the two scenario performung an analysis of th droplets displacement.

§ 7.4. Herringbone pattern

In the previous section, we presented a systematic study regarding the effects of a straight grooves, placed perpendicular respect to the flow, on the fluidization of a dense emulsion. We tested different emulsion volume fraction, pressure drop along the channel and a wide number of widths-gaps combination. In this section the results are described for a different roughness topology consisting in rectangular grooves with a herringbone shape (or V-grooves). Respect to the straight grooves, where there is not a preferential direction of the flow (i.e., the roughness is symmetric in the transversal section), in V-grooves this symmetry is lost. The aim is to understand how the transversal asymmetry, introduced by the herringbone grooves, influences the flow of concentrated emulsion in term of plastic rearrangements and local fluidization.

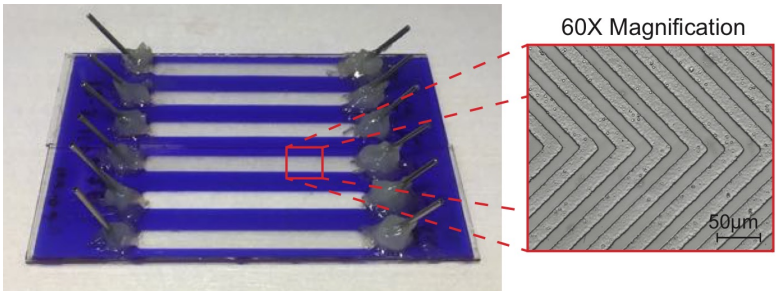

Figure 7.18: Pictures of the microfluidic channel presenting herringbone pattern on the bottom wall.

The devices were fabricated following the same procedure described in section 6.2. The V-shaped grooves were realized on the bottom wall of the channel and we used dry photoresist to realize the channel walls. With this procedure we obtained channels with a height H=120 μm, a length L=4 cm and a width W=0,5 cm. The controlled roughness, placed centrally respect the longitudinal axis of the channel, is characterized by an fixed height of 2.5 μm. The herringbone pattern are characterized by an angle α=45° and three combinations of widths and gaps: 8-8, 15-15 and 25-25 μm (see fig. 7.18). We used an oil-in-water emulsion with a mean droplets diameter of d =5.65 μm and a polydispersity index of 0.65. In table 7.2 are reported the parameters used to fit rheological curves for different volume fraction, measured with a rotational rheometer. As for previous experiments, the flow profiles $v_{flow}(z)$ were collected using μ-PTV and analyzed with a custom made software (see Chapter 6).

Table 7.2: Parameters for the bulk rheological flow curves according to the Herschel-Bulkley model $\sigma = \sigma_Y + A\,\dot{\gamma}^n$, for various volume fractions Φ of the emulsions.

Volume fraction Φ	σ_Y (Pa)	A (Pa s$^{1/2}$)	n
0.875	43.17	26.86	0.5
0.85	29.47	22.64	0.5

§ 7.4.1. Forward vs. Backward

Using a roughness with herringbone pattern we can distinguish two different flow directions as depicted in fig. 7.19. We labeled these two as *forward* and *backward*. In the forward direction ("fwd"), the fluids flow has the same direction of the grooves' tips, while in the backward direction ("bwd") the flow is opposite to the grooves' tips. During experiments, flow profiles were collected in two regions in the transversal direction of the channel y: in the center (i.e along the longitudinal axis of the channel) and in a side region at the same distance ($\sim 1\,\mathrm{mm}$) between the herringbone tips and the side wall of the channel (see fig. 7.19).

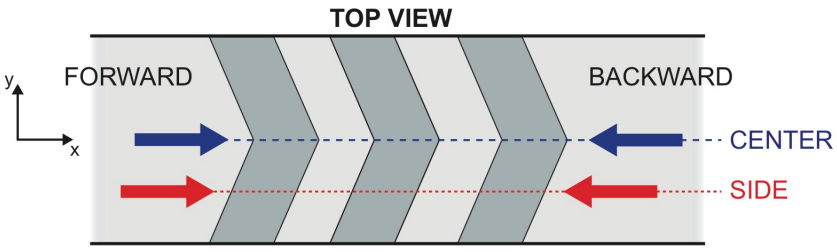

Figure 7.19: Top view representation of V-grooves roughness. Arrows indicate the two possible flow direction: forward and backward. Dashed and dotted lines indicates respectively the position at the center (blue) and on the side (red) of the channel.

Experimental flow profiles for a fixed volume fraction $\phi = 0.85$ and fixed geometry ($w/d = 2.65$, $g/d = 2.65$) are reported fig. 7.20. Filled dots curves refers to flow profiles collected in the center of the channel in the froward (▲) and backward (▼) direction. As for the straight grooves, both curves show a difference in the slip velocities between the smooth and rough surfaces due to the presence of the roughness on the bottom wall. Moreover, flow curves exhibit different plug velocities in the central region of the channel (z/H $\simeq$ 0). The plug velocity in the forward direction ($\mathrm{v_{fwd}}$) in grater than the plug velocity in the backward direction ($\mathrm{v_{bwd}}$), i.e., the emulsion flows faster in the forward respect to the backward direction.

Flow profiles collected on the side region are reported with empty dots. Upside triangles (△) refer to forward direction, while downside triangles refer to (▽) backward direction. The two curves are identical, meaning that the flow exhibits the same behavior in both directions. Conversely, the presence of asymmetric roughness introduce a difference in the plug velocities only in the central region of the channel where the grooves' asymmetry is greater. On the side region where the asymmetry is less marked, this difference vanishes.

To explain this different between the center and the side of the channel, where the flow profile is biased by the asymmetry of the roughness, we propose a very simple and intuitive description in term of a different micro-mechanical behavior of the emulsion flow in the two cases. First, we consider the flow along the x axis of the channel in the forward direction. In this case the emulsion droplets are flowing in the same direction of the herringbone tips driven by the applied pressure drop. Once a droplet falls into a groove it can easily slide along the groove, pushed by other droplets, instead of jumps across it. At this point two forces are acting on the droplets as depicted in fig. 7.21a, b. The first force is the pressure drop which it is parallel to the longitudinal

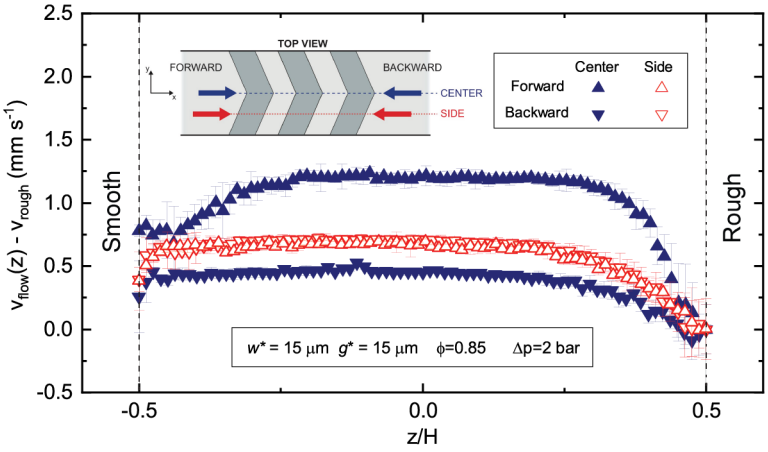

Figure 7.20: Velocity profiles $v_{flow}(z)$ measured for emulsions' droplets flowing through microfluidic channel patterned with V-grooves roughness characterized by w^*=15 μm and g^*=15 μm. Wall slip velocity at the rough walls has been subtracted from the whole profile.

axis of the channel while the second it is the normal force of the wall. The resulting force (blue arrows of fig. 7.21) is parallel to the grooves' walls and pushes the droplet until it reaches the center of the channel. Once the center is reached, the droplet can only moves jumping across the grooves pushed by other droplets coming from both sides and from the back. The jump activates a plastic rearrangement. In this pictures the rearrangements are more concentrated in the middle of the channel respect the side. They are promoted by: i) droplets that jumps over the grooves (as for straight grooves) and by ii) droplets motion from the side to the center. As a consequence, the rate of plastic rearrangements is very high and the fluidity of the emulsion increases. The high fluidity affects the velocity profile exhibiting a large absolute plug velocity and a bigger Δv_{slip}.

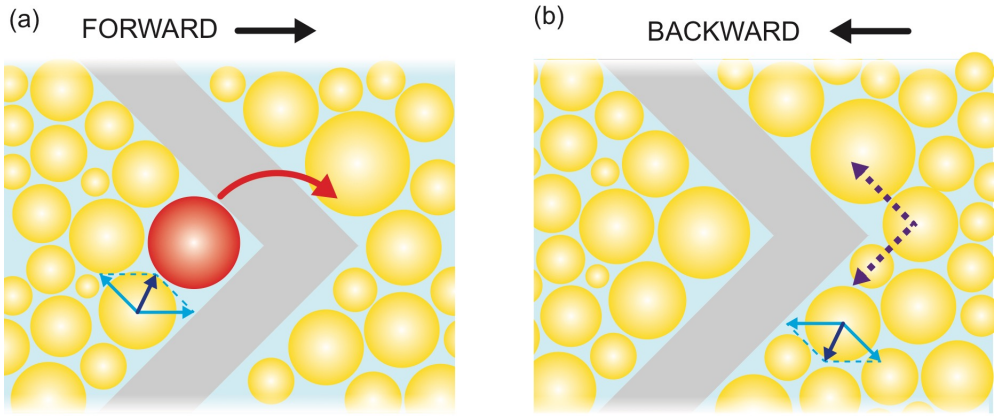

Figure 7.21: Graphical representation of rearrangement mechanism for the emulsion flowing in the central region of the channel respectively in (a) forward and (b) backward direction.

In the backward direction, when a droplet reaches the herringbone tip it is not confined by the geometry as for the forward case. It can easily move to the left or right (respect to the center) and

slides along the wall (see fig. 7.21b) triggering a smaller number of plastic rearrangements. As a consequence, the Δv_{slip} and the absolute value of v_{plug} are narrow, meaning that the fluidization is smaller, i.e., the droplets rearrange less frequently than in the forward case. While in the central region of the channel the geometry is clearly different in the forward and backward direction, on the lateral region the difference is less pronounced. In fact, far enough from the later walls and the herringbone tips, the roughness consists in a series of tilted grooves with two opposite orientations depending on the flow direction. Flowing forward or backward the effect on the emulsion is the same. Once droplets fell into the a groove, they behave similarly. They slide along the wall and sometimes jump out activating a plastic rearrangements. As a consequence, the rate of plastic activity and the resulting fluidization is comparable in both directions. This explains the absence of difference in the plug velocities between the two directions in the center of the channel as reported in fig. 7.20. Unfortunately numerical simulations can not help and support this description because they are limited to the 2D case.

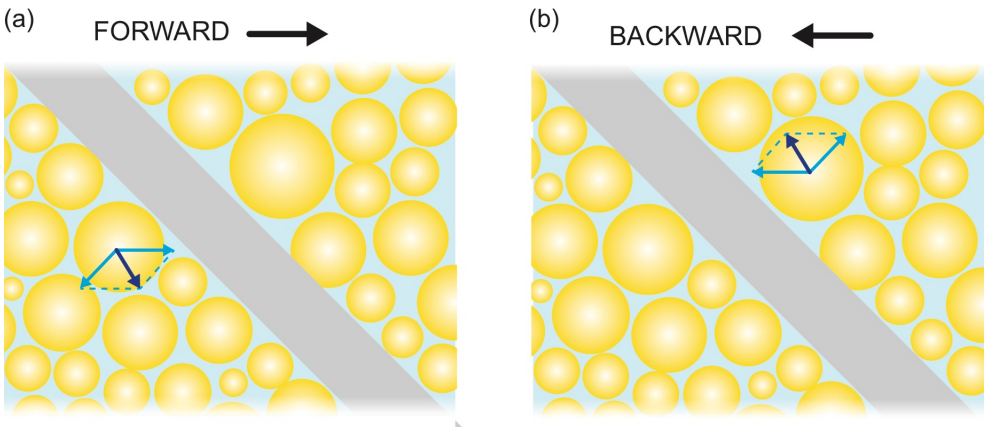

Figure 7.22: Graphical representation of rearrangement mechanism for the emulsion flowing in the lateral region of the channel, respectively in (a) forward and (b) backward direction.

In our previous discussion, we justify the presence of a difference in the plug velocities between the forward and the backward flow describing two different fluidization scenarios. Both of them deal with the presence of plastic rearrangements, due to the interaction of emulsion's droplets with grooves. This plastic activity is not present in the flow of a Newtonian fluid as reported in fig. 7.23b. The graph shows the velocity profiles for pure glycerol at two different pressure drops in a microfluidic channel presenting the herringbone pattern. For both pressures the profiles do not present any significant difference in the plug velocities in the forward and backward direction. The presence of asymmetric roughness does not influence the velocity profiles because there are no plastic rearrangements (i.e., glycerol molecules are too small to interact with the roughness). Moreover, both flow profiles show a parabolic shape typical of Poiseuille flows where the flux is laminar ($Re \simeq 10^{-5}$) and there is not turbulence. The only effect, introduced by the roughness, is a very small variation in the slip velocity [187–190], but it is too small to be quantify by our experimental setup.

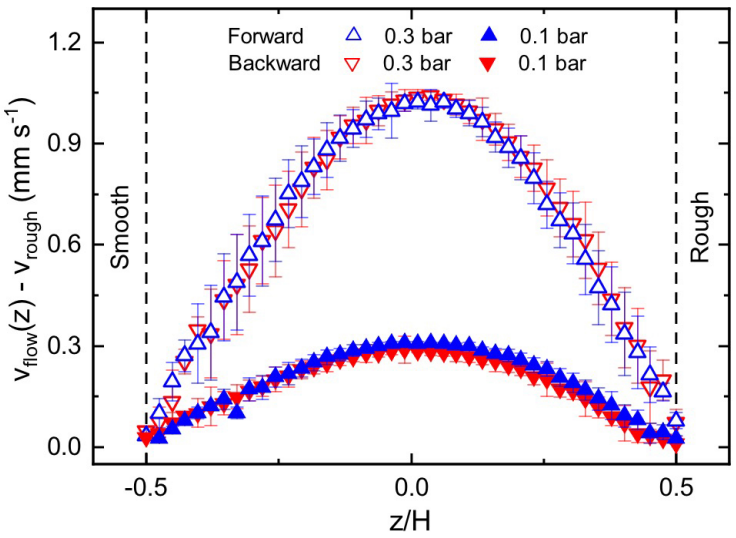

Figure 7.23: Velocity profiles $v_{flow}(z)$ measured in V-grooves channel for glycerol.

§ 7.4.2. Effect of the grooves' periodicity

To better characterize the effect and understand which parameters are involved, we performed measurements using various width-gap periodicity and different pressure drops. To characterize quantitatively the difference of plug velocities we defined the quantity Δv_{plug} as:

$$\Delta v_{plug} = \frac{v_{fwd} - v_{bwd}}{v_{fwd}} = 1 - \frac{v_{bwd}}{v_{fwd}} \tag{7.9}$$

with v_{fwd} and v_{bwd} respectively the plug velocities for the flow in forward and backward directions. We calculated v_{fwd} and v_{bwd} by averaging the measured velocities in the 5-10 droplets diameters region within the center of the channel ($z \simeq 0$). The effect of the herringbone roughness are observed only along the longitudinal axis of the channel (i.e., central region). For this reason, we focused our measurements only in this region while neglecting the side region.

We extend our experiments to other of widths and gaps combinations. In fig. 7.24a, we report flow profiles (backward and forward) for three different roughness combinations (g-w): 8-8, 15-15 and 25-25 μm at a fixed pressure drop Δp=3 bar. From the graph we observe that increasing the periodicity of the roughness the Δv_{plug} decrease. This is highlighted from the inset of fig. 7.24a where plug velocities difference is plotted as a function of the roughens periodicity.
A larger periodicity induces a smaller number of plastic rearrangements. In fact, increasing λ we recover a smooth surface where the plastic activity is reduced respect a rough ones. On the contrary, in small width-gap combination ($g/d \simeq 1$) the rate of rearrangements is very high. This plastic activity induces an huge fluidization on the shear region of the flow increasing the flowing velocity. The droplets are forced to move towards the center of the channel where they rearrange with a high frequency. This trend it is not valid at higher volume fraction (ϕ=0.875)

as reported in fig. 7.24b where, the Δv_{plug} is plotted as a function of periodicity λ for all pressure drop and both volume fractions. An emulsion with higher volume fraction has an higher yield stress as reported in table 7.2. Consequently, it is necessary a higher stress to induce the plastic rearrangements. At low pressure drop (1 and 2 bar) the stress, in the shear region, is not sufficient to activate plastic rearrangements and the profiles have similar Δv_{plug} for al widths-gaps combinations. Increasing the pressure drop the stress is higher and the fluidization process is more efficient and, increasing lambda, the Δv_{plug} slightly decreases.

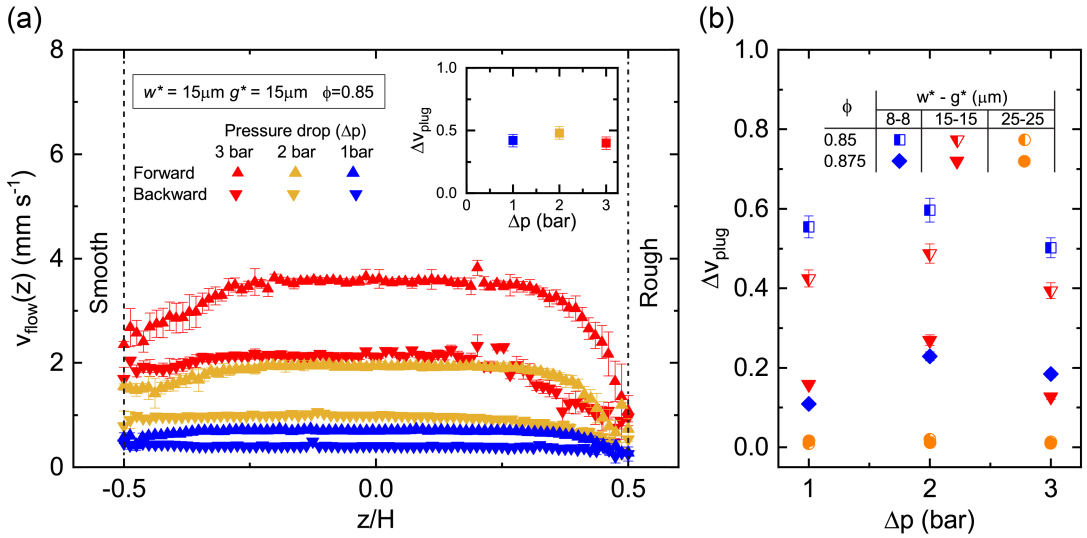

Figure 7.24: (a) Velocity profiles $v_{flow}(z)$ measured for different combinations of width (w) and gaps (g), at fixed volume fraction and pressure drop. Inset reports the Δv_{plug} as a function of $\lambda^* = (w^* + g^*)$. (b) Plug velocity difference as a function of lambda for all pressure drops and volume fractions.

§ 7.4.3. Effect of the pressure drop

After the effect of the grooves' periodicity, we study the effect of pressure drop in the difference of plus velocities. In fig. 7.25a are reported the velocity profiles, collected for both directions, at three different pressure drop: $\Delta p = 1, 2, 3$ bar keeping fixed the volume fraction (ϕ=0,85) and the periodicity (w^*-g^*= 15-15 μm).

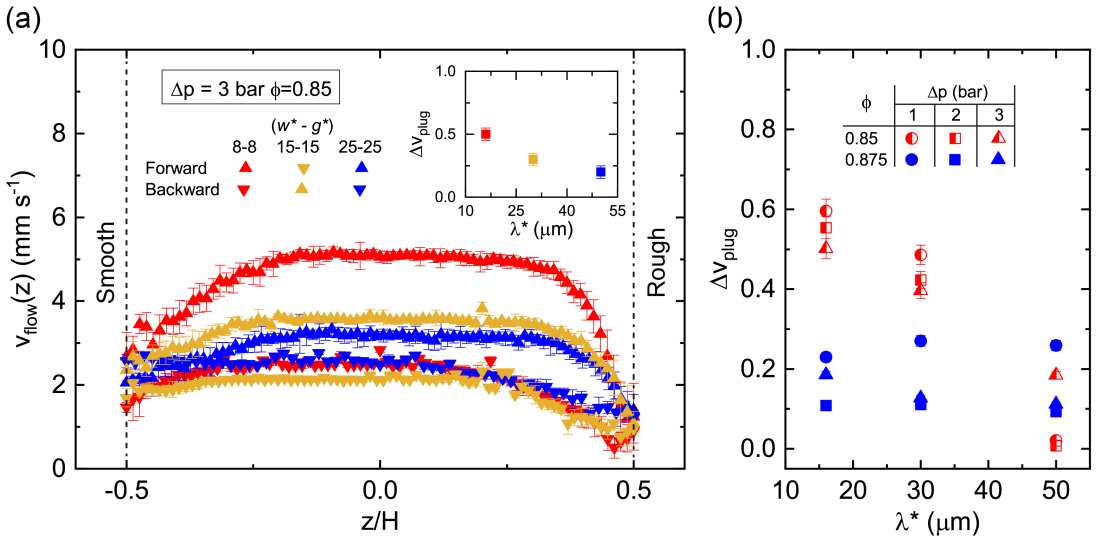

Figure 7.25: Flow profiles $v_{flow}(z)$ at fixed V-grooves roughness ($w = 21$, $g = 21$) for different pressure drops at fixed volume fraction. In the inset are plotted Δv_{plug} as a function of pressure drop Δp. (b) Plug velocity difference as a function of pressure for all lambdas and volume fractions.

Increasing the pressure drops, absolute values of plug velocities increase in both direction because the emulsion is flowing faster. Looking at the Δv_{plug}, it does not increase with higher pressure drops as highlighted in the inset of fig. 7.25a. The Δv_{plug} slightly increases at 2 bar, but then at 3 bar it decreases and reach a value similar to the ones at 1 bar. This is also true for the other volume fraction (ϕ=0,875), and for other widths-gaps combinations as reported in fig. 7.25.

At first, for all data points, the increment of pressure drop leads to an higher value of Δv_{plug}. Increasing the pressure, the stress grows up, as well as the the shear region's size. More plastic rearrangements take place and the effect of asymmetric roughness is visible. If the pressure increases even further (3 bar) the applied stress covers the effect of the roughness. Hence we observe a decrement of the Δv_{plug}.

§ 7.4.4. Effect of the angle

In order to obtain a full characterization of the effect of the V-grooves roughness in the flow of dense emulsion, we tested three different herringbone patterns with an angle α: 30°, 45° and 60° (see fig. 6.7b). A summary with the characteristics of the V-shape patterns is reported in table 6.3. The collected flow profiles for fixed pressure drop $\Delta p = 1$ bar, volume fraction ϕ=0.75 and a combination of g^*-w^*=15-15 μm are reported in fig. 7.26. Upside triangles refer to forward flows while downside triangles refer to backward flows. Moreover, velocity profiles for straight grooves (α=90°) are reported as reference with empty triangles.

Considering the values plug velocity, we observe an increment of the forward velocity if the angle decreases. On the contrary, the plug velocities in the backward direction decrease with the decreasing of the angle. This combined effect leads to an higher Δv_{plug} as the angle decreases.

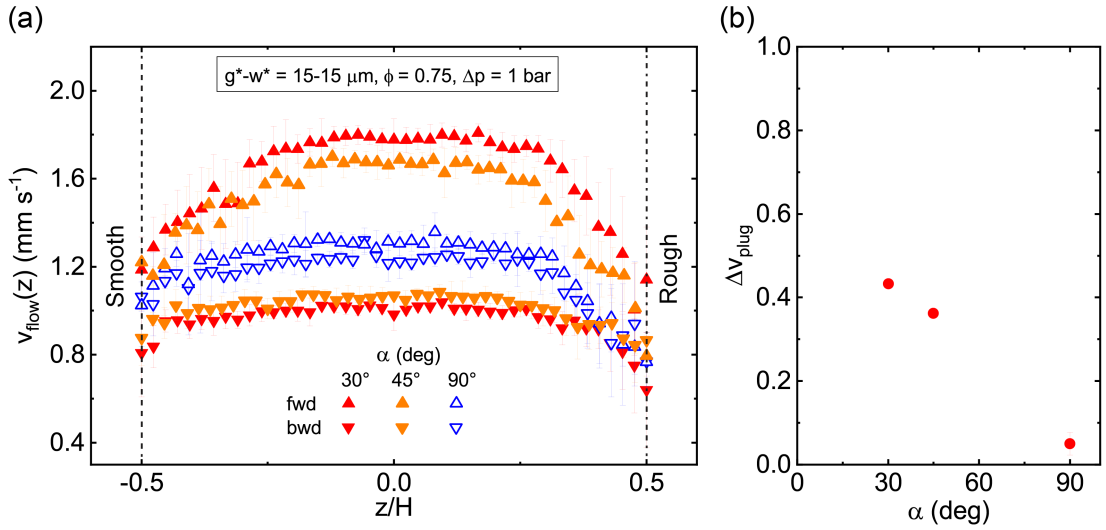

Figure 7.26: Flow profiles $v_{flow}(z)$ at fixed V-grooves roughness (w^*-g^*=15-15 μm), pressure drop ($\Delta p = 1$ bar) and volume fraction (ϕ=0.75) for different angles of the herringbone grooves.

For the 90° we observe a slight difference between the two directions even if the two profiles should be equals because of the transversal symmetry of the roughness. This difference is less than 10% and we can ascribe it caused by small variation of the emulsion volume fraction during the experiment.
Considering the forward flow, smaller is the angle (i.e., 30°) higher is the guidance effect of the grooves. Hence a high number of plastic rearrangement occurs increasing the fluidity of the fluid and so emulsion flows faster. Increasing the angle, the guidance effect is lower and so the flow is slower. For the backward flow the outcome is the opposite. The greater guiding-effect provided by smaller angles deflects droplets from the center. Therefore the rate of plastic rearrangements in the center is reduced (i.e., less fluidization) and a slower speed. Combining the two effects, we observe a progressive reduction of the Δv_{plug} increasing angle the V-grooves patterns as reported fig. 7.26b.

Summary

- The presence of herringbone roughness introduces an asymmetry in the velocity velocity profiles between the *forward* and *backward* direction. The enhancement effect is present only in along the longitudinal axis of the channel. In the side region of the channel the two flow profiles are equal.
- We suggest a micro-mechanical interpretation to describe this difference of plug velocities in terms of different fluidization (i.e., different rate of plastic rearrangements).
- We observe that increasing the roughness periodicity λ the plug velocity difference vanishes.

Conclusions

This PhD research studied the effects of micro-textured roughness on the fluidization of concentrated flowing in a microfluidic channel. The fluidization originates from a succession of elastic deformations of the micro-structural constituents (*e.g.* droplets in the case of emulsions) and plastic rearrangements which releases the accumulated elastic stress induced by the roughness. In this research we deeply analyzed the connection between the fluidization, heterogeneous dynamics and rate of plastic rearrangements close to the rough walls: in fact, surface roughness can trigger rearrangements and introduce large fluctuation of the local fluidization associated with the interactions of droplets against the rough wall. The main conclusions of this work are reported below. Taken all together, our findings suggest operative strategies for tuning the flowing properties of soft-glassy materials in confined microchannels by a suitable tailoring of the surface roughness.

(i) Roughness effects

The flow of oil-in-water concentrated emulsion was investigated in dedicated microfluidic channels having one smooth wall and the other patterned with a controlled micron-size roughness. This configuration allowed to compare the slip velocities and the rough-induced fluidization on smooth and rough walls in the same channel under the same flow conditions. We observed the presence of a difference on the wall slip velocities between the smooth and the rough walls. This difference is directly connected to the rate of plastic rearrangements. The higher is the velocities difference, the higher is the rate of plastic rearrangements (i.e. fluidity). By changing parameter as: grooves density, emulsion packing fraction and applied pressure rescaled data collapsed into a single master curve in which triggered fluidization follows a power-law scaling in terms of the density of the rough elements.

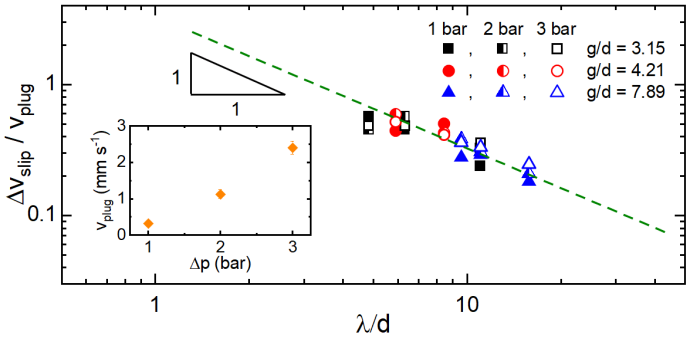

Difference of the slip velocities, normalized by the maximum (plug) velocity v_{plug}, as a function of the wall roughness periodicity λ in units of the mean droplet diameter d. Dashed line is a guide for the eyes with slope -1.

(ii) Spatial distribution of plastic activity

Lattice-Boltzmann numerical simulations allowed to access simultaneously the flow profiles and plastic rearrangements. We mapped the plastic activity and we observed that the rate of rearrangements is enhanced near the rough wall in contrast with the smooth case where, the rate is relatively small and rather homogeneous. Consequently, the fluidization is more efficient near the rough wall. This analysis provide a direct link between the fluidization and the spatial distribution of plastic rearrangements.

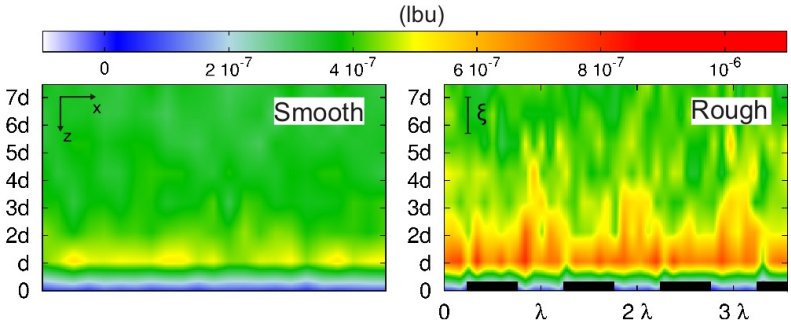

Spatial distribution of Γ in a Couette geometry, highlighting the properties of a sheared layer close to smooth and rough walls. The distance from the wall shown in units of the mean droplet diameter. Data are reported in lattice Boltzmann units (lbu).

(iii) Gaps effect: from "stiff" to "soft" roughness

By analyzing an ample variety of patterns, we observe a transition in the fluidization with the decreasing of grooves' separation. To justify this transition we suggest two different scenarios: for wide gaps (i.e large grooves separation) droplets can get-in and get-out of the grooves quite easily; for narrow gaps droplets get trapped and cannot escape easily, thus form periodically repeating "soft" obstacles. Numerical simulations have been instrumental to show that the two scenarios can be further distinguished via the profiles of the fluidity field and – more importantly – via the statistical properties of the displacement field of the droplets.

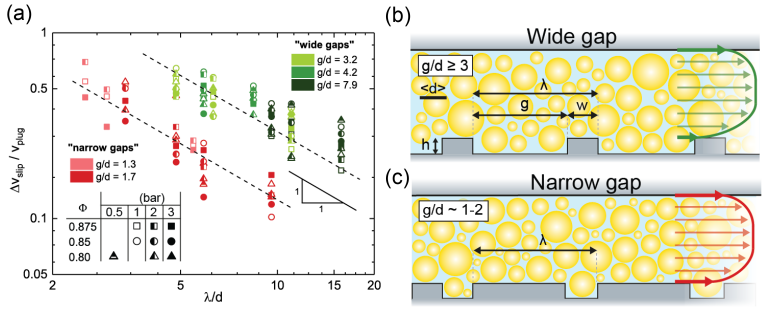

Difference of the wall slip velocities, normalized by the plug velocity v_{plug}, as a function of the wall roughness periodicity $\lambda = g + w$ in units of the mean droplet diameter. Green colored symbols refer to wide gaps $g/d \geq 3$ and red scaled symbols refer to narrow gap $g/d \approx 1 - 2$. Schematic representation of "wide" (b) , and "narrow" gaps geometries (c).

(iv) Herringbone pattern

We have investigated the effect of other geometries with the aim to obtain a more precise control in the flow properties. The presence of asymmetric micro-roughness (herringbone pattern) introduced new scenarios and interesting flow behaviors. With this asymmetric roughness we observed an enhancement of fluidization (i.e. the emulsion flow faster) when the flow has the same direction of the herringbone (*forward direction*) respect the case in which the emulsion is flowing in opposite direction (*backward direction*). Flowing forward, emulsion's constituents moved toward the center where they are forced to rearrange releasing the accumulated stress (i.e higher fluidization). Otherwise, in the backward direction emulsion's droplets moved towards the sides of the channel with a lower rate of plastic rearrangements (i.e. lower fluidization).

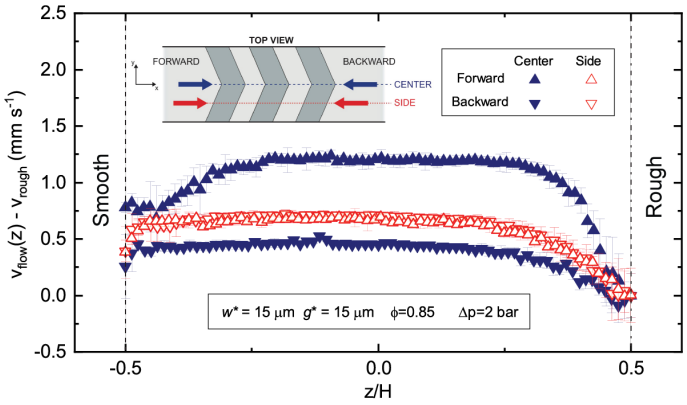

Velocity profiles $v_{flow}(z)$ measured for emulsions' droplets flowing through microfluidic channel patterned with V-grooves roughness characterized by w^*-g^*=15-15 μm. Wall slip velocity at the rough walls has been subtracted from the whole profile.

A. Tracking program: python code

In this appendix the Python code of Particle Tracking Velocimetry analysis is reported.

```
from ij import IJ, ImagePlus, ImageStack, WindowManager
import fiji.plugin.trackmate.Settings as Settings
import fiji.plugin.trackmate.Model as Model
import fiji.plugin.trackmate.SelectionModel as SelectionModel
import fiji.plugin.trackmate.TrackMate as TrackMate
import fiji.plugin.trackmate.Logger as Logger
import fiji.plugin.trackmate.detection.DetectorKeys as DetectorKeys
import fiji.plugin.trackmate.detection.DogDetectorFactory as
    ↪ DogDetectorFactory
import fiji.plugin.trackmate.tracking.sparselap.SparseLAPTrackerFactory as
    ↪ SparseLAPTrackerFactory
import fiji.plugin.trackmate.tracking.LAPUtils as LAPUtils
import fiji.plugin.trackmate.visualization.hyperstack.HyperStackDisplayer
    ↪ as HyperStackDisplayer
import fiji.plugin.trackmate.features.FeatureFilter as FeatureFilter
import fiji.plugin.trackmate.features.FeatureAnalyzer as FeatureAnalyzer
import fiji.plugin.trackmate.features.spot.
    ↪ SpotContrastAndSNRAnalyzerFactory as
    ↪ SpotContrastAndSNRAnalyzerFactory
import fiji.plugin.trackmate.action.ExportStatsToIJAction as
    ↪ ExportStatsToIJAction
import fiji.plugin.trackmate.io.TmXmlReader as TmXmlReader
import fiji.plugin.trackmate.action.ExportTracksToXML as ExportTracksToXML
import fiji.plugin.trackmate.io.TmXmlWriter as TmXmlWriter
import fiji.plugin.trackmate.features.ModelFeatureUpdater as
    ↪ ModelFeatureUpdater
import fiji.plugin.trackmate.features.SpotFeatureCalculator as
    ↪ SpotFeatureCalculator
import fiji.plugin.trackmate.features.spot.SpotContrastAndSNRAnalyzer as
    ↪ SpotContrastAndSNRAnalyzer
import fiji.plugin.trackmate.features.spot.SpotIntensityAnalyzerFactory as
    ↪ SpotIntensityAnalyzerFactory
import fiji.plugin.trackmate.features.track.TrackSpeedStatisticsAnalyzer as
    ↪  TrackSpeedStatisticsAnalyzer
import fiji.plugin.trackmate.util.TMUtils as TMUtils
import fiji.plugin.trackmate.features.track.TrackBranchingAnalyzer as
    ↪ TrackBranchingAnalyzer
```

```
import fiji.plugin.trackmate.features.track.TrackDurationAnalyzer as
    ↪ TrackDurationAnalyzer
import sys

#-------------------------
# Get currently selected stack
#-------------------------
imp = WindowManager.getCurrentImage()
stack= getArgument()


#-------------------------
# Instantiate model object
#-------------------------
model = Model()

# Set logger
model.setLogger(Logger.IJ_LOGGER)

#-------------------------
# Prepare settings object
#-------------------------
settings = Settings()
settings.setFrom(imp)

#-------------------------
# CONFIGURE DETECTOR
# Set paramiters for particle detection
#-------------------------
settings.detectorFactory = DogDetectorFactory()
settings.detectorSettings = {
DetectorKeys.KEY_DO_SUBPIXEL_LOCALIZATION : True,
DetectorKeys.KEY_RADIUS : 2.0,
DetectorKeys.KEY_TARGET_CHANNEL : 1,
DetectorKeys.KEY_THRESHOLD : 5.0,
DetectorKeys.KEY_DO_MEDIAN_FILTERING : False,
}

# Configure spot filters - Filter on quality

filter1 = FeatureFilter('QUALITY', 1, True)
settings.addSpotFilter(filter1)


# Configure track filters - Filter on number of spots.

filter2 = FeatureFilter('NUMBER_SPOTS', 4, True)
```

```
settings.addTrackFilter(filter2)

#-------------------------
# Configure tracker
#-------------------------
settings.trackerFactory = SparseLAPTrackerFactory()
settings.trackerSettings = LAPUtils.getDefaultLAPSettingsMap()
settings.trackerSettings['LINKING_MAX_DISTANCE'] = 4.0
settings.trackerSettings['GAP_CLOSING_MAX_DISTANCE']=2.0
settings.trackerSettings['MAX_FRAME_GAP']= 3

settings.initialSpotFilterValue = 1


#-------------------------
# Instantiate trackmate
#-------------------------
trackmate = TrackMate(model, settings)


#------------
# Execute all
#------------
ok = trackmate.checkInput()
if not ok:
sys.exit(str(trackmate.getErrorMessage()))

ok = trackmate.process()
if not ok:
sys.exit(str(trackmate.getErrorMessage()))


#----------------
# Prepare output *.dat file
#----------------

output = (stack+'.txt')
out_file = open(output, "w")
out_file.write(str(0.001) + ' ' + str(0.001) + '\n')


#----------------
# Display results
#----------------
model.getLogger().log('Found ' + str(model.getTrackModel().nTracks(True)) +
    ↪  ' tracks.')
```

```
selectionModel = SelectionModel(model)
displayer =  HyperStackDisplayer(model, selectionModel, imp)
displayer.render()
displayer.refresh()

# The feature model, that stores edge and track features.
fm = model.getFeatureModel()
output = ''
for id in model.getTrackModel().trackIDs(True):

# Fetch the track feature from the feature model.
velocity = fm.getTrackFeature(id, 'TRACK_MEAN_SPEED')
ns = fm.getTrackFeature(id, 'NUMBER_SPOTS')
td = fm.getTrackFeature(id, 'TRACK_DURATION')

# conversion from pixel/frame to mm/s
vscaled = (velocity*0.6983)


#----------------
# Write results
#----------------

out_file.write(str(ns) + ' ' + str(vscaled) + '\n')
out_file.close()
```

Bibliography

[1] A. J. Liu and S. R. Nagel, "Nonlinear dynamics: Jamming is not just cool any more", *Nature*, vol. 396, no. 6706, pp. 21–22, 1998.

[2] A. A. Diaz and L. Trujillo, "Complex Fluids, Soft Matter and the Jamming Transition Problem", in *Computational and Experimental Fluid Mechanics with Applications to Physics, Engineering and the Environment.* Springer, 2014, pp. 211–233.

[3] H. M. Princen and A. D. Kiss, "Rheology of foams and highly concentrated emulsions", *J. Colloid Interface Sci.*, vol. 112, no. 2, pp. 427–437, 1986.

[4] N. D. Denkov, S. Tcholakova, K. Golemanov, K. P. Ananthpadmanabhan, and A. Lips, "The role of surfactant type and bubble surface mobility in foam rheology", *Soft Matter*, vol. 5, no. 18, pp. 3389–3408, 2009.

[5] J. Goyon, A. Colin, G. Ovarlez, A. Ajdari, and L. Bocquet, "How does a soft glassy material flow: finite size effects, non local rheology, and flow cooperativity", *Soft Matter*, vol. 6, pp. 2668–2678, 2010.

[6] T. G. Mason, "New fundamental concepts in emulsion rheology [Review]", *Current Opinion in Colloid & Interface Science*, vol. 4, no. 3, pp. 231–238, 1999.

[7] D. Bonn, M. M. Denn, L. Berthier, T. Divoux, and S. Manneville, "Yield stress materials in soft condensed matter", *Reviews of Modern Physics*, vol. 89, no. 3, pp. 1–44, 2017.

[8] P. Coussot, "Yield stress fluid flows: A review of experimental data", *Journal of Non-Newtonian Fluid Mechanics*, vol. 211, pp. 31–49, 2014.

[9] Q. D. Nguyen and D. V. Boger, "Measuring the Flow Properties of Yield Stress Fluids", *Annual Review of Fluid Mechanics*, vol. 24, no. 1, pp. 47–88, 1992.

[10] G. Picard, A. Ajdari, F. b. ç. Lequeux, and L. Bocquet, "Slow flows of yield stress fluids: Complex spatiotemporal behavior within a simple elastoplastic model", *Phys. Rev. E*, vol. 71, no. 1, p. 10501, 2005.

[11] J. Goyon, A. Colin, G. Ovarlez, A. Ajdari, and L. Bocquet, "Spatial cooperativity in soft glassy flows", *Nature*, vol. 454, no. 7200, pp. 84–87, 2008.

[12] R. Benzi, M. Sbragaglia, M. Bernaschi, S. Succi, and F. Toschi, "Cooperativity flows and shear-bandings: a statistical field theory approach", *Soft Matter*, vol. 12, no. 2, pp. 514–530, 2016.

[13] M. L. Falk and J. S. Langer, "Dynamics of viscoplastic deformation in amorphous solids", *Phys. Rev. E*, vol. 57, no. 6, pp. 7192–7205, 1998.

[14] P. Sollich, "Soft glassy rheology", *Molecular Gels: Materials with Self-Assembled Fibrillar Networks*, pp. 161–192, 2006.

[15] P. Jop, V. Mansard, P. Chaudhuri, L. Bocquet, and A. Colin, "Microscale Rheology of a Soft Glassy Material Close to Yielding", *Phys. Rev. Lett.*, vol. 108, no. 14, p. 148301, 2012.

[16] A. Nicolas and J.-L. Barrat, "Spatial Cooperativity in Microchannel Flows of Soft Jammed Materials: A Mesoscopic Approach", *Phys. Rev. Lett.*, vol. 110, no. 13, p. 138304, 2013.

[17] B. Dollet and C. Bocher, "Flow of foam through a convergent channel", *European Physical Journal E*, vol. 38, no. 11, pp. 1–11, 2015.

[18] M. Zhang, J. Wu, L. Wang, K. Xiao, and W. Wen, "A simple method for fabricating multi-layer PDMS structures for 3D microfluidic chips", *Lab on a Chip*, vol. 10, no. 9, p. 1199, 2010.

[19] V. Mansard, L. Bocquet, and A. Colin, "Boundary conditions for soft glassy flows: slippage and surface fluidization", *Soft Matter*, vol. 10, no. 36, pp. 6984–6989, 2014.

[20] J. Paredes, N. Shahidzadeh, and D. Bonn, "Wall slip and fluidity in emulsion flow", *Phys. Rev. E*, vol. 92, no. 4, p. 42313, 2015.

[21] A. Scagliarini, M. Lulli, M. Sbragaglia, and M. Bernaschi, "Fluidisation and plastic activity in a model soft-glassy material flowing in micro-channels with rough walls", *EPL (Europhysics Letters)*, vol. 114, no. 6, p. 64003, 2016.

[22] R. G. Larson, *The structure and rheology of complex fluids (topics in chemical engineering)*. Oxford University Press, 1999, vol. 86.

[23] C. W. Macosko and R. G. Larson, *Rheology: principles, measurements, and applications*. Vch New York, 1994.

[24] J. M. Krishnan, A. P. Deshpande, and P. B. S. Kumar, *Rheology of Complex Fluids*. New York, NY: Springer New York, 2010.

[25] H. Bruus, *Theoretical microfluidics*. Oxford University Press, 2008.

[26] O. s. of Rheology and nomenclature of The Society, "Official symbols and nomenclature of The Society of Rheology", *Journal of Rheology*, vol. 57, no. 4, pp. 1047–1055, 2013.

[27] H. A. Barnes, "Shear-Thickening ("Dilatancy") in Suspensions of Nonaggregating Solid Particles Dispersed in Newtonian Liquids", *Journal of Rheology*, vol. 33, no. 2, pp. 329–366, 1989.

[28] Q. D. Nguyen and D. V. Boger, "Thixotropic behaviour of concentrated bauxite residue suspensions", *Rheologica Acta*, vol. 24, no. 4, pp. 427–437, 1985.

[29] I. Steg and D. Katz, "Rheopexy in some polar fluids and in their concentrated solutions in slightly polar solvents", *Journal of Applied Polymer Science*, vol. 9, no. 9, pp. 3177–3193, 1965.

[30] P. J. Carreau, D. De Kee, and R. J. Chhabra, "Rheology of Polymeric Systems, Hanser", *Gardner, New York*, 1997.

[31] R. P. Chhabra, *Bubbles, drops, and particles in non-Newtonian fluids.* CRC press, 2006.

[32] G. V. Barbosa-Canovas and A. Ibarz, *Unit operations in food engineering.* CRC press, 2002.

[33] G. W. Govier and K. Aziz, "The Flow of Complex Mixtures in Pipe. Robert E", 1977.

[34] M. M. Cross, "Rheology of non-Newtonian fluids: a new flow equation for pseudoplastic systems." *J. Colloid Interface Sci.*, vol. 20, pp. 417–437, 1965.

[35] A. B. Metzner and M. Whitlock, "Flow behavior of concentrated (dilatant) suspensions", *Transactions of the Society of Rheology*, vol. 2, no. 1, pp. 239–254, 1958.

[36] R. Hoffman, "Discontinuous and dilatant viscosity behavior in concentrated suspensions. II. Theory and experimental tests", *Journal of Colloid and Interface Science*, vol. 46, no. 3, pp. 491–506, 1974.

[37] N. J. Wagner and J. F. Brady, "Shear thickening in colloidal dispersions", *Physics Today*, vol. 62, no. 10, pp. 27–32, 2009.

[38] J. F. Brady and G. Bossis, "The rheology of concentrated suspensions of spheres in simple shear flow by numerical simulation", *Journal of Fluid Mechanics*, vol. 155, p. 105, 1985.

[39] A. A. Catherall, J. R. Melrose, and R. C. Ball, "Shear thickening and order–disorder effects in concentrated colloids at high shear rates", *Journal of Rheology*, vol. 44, no. 1, p. 1, 1999.

[40] R. Mari, R. Seto, J. F. Morris, and M. M. Denn, "Shear thickening, frictionless and frictional rheologies in non-Brownian suspensions", *Journal of Rheology*, vol. 58, no. 6, pp. 1693–1724, 2014.

[41] R. Mari, R. Seto, J. F. Morris, and M. M. Denn, "Nonmonotonic flow curves of shear thickening suspensions", *Physical Review E*, vol. 91, no. 5, p. 052302, 2015.

[42] J. Comtet, G. Chatté, A. Niguès, L. Bocquet, A. Siria, and A. Colin, "Pairwise frictional profile between particles determines discontinuous shear thickening transition in non-colloidal suspensions", *Nature Communications*, vol. 8, p. 15633, 2017.

[43] H. A. Barnes, "The yield stress—a review or '$\pi\alpha\nu\tau\alpha$ $\rho\epsilon\iota$'—everything flows?" *Journal of Non-Newtonian Fluid Mechanics*, vol. 81, no. 1-2, pp. 133–178, 1999.

[44] R. B. Bird, G. C. Dai, and B. J. Yarusso, "The rheology and flow of viscoplastic materials", *Reviews in Chemical Engineering*, vol. 1, no. 1, pp. 1–70, 1983.

[45] H. A. Barnes, J. F. Hutton, and K. Walters, "Linear viscoelasticity", *An introduction to rheology*, vol. 3, pp. 37–54, 1989.

[46] R. P. Chhabra and J. F. Richardson, "Non-Newtonian Flow and Applied Rheology", *Engineering Applications*, p. 14, 2008.

[47] K. Dullaert and J. Mewis, "A structural kinetics model for thixotropy", *Journal of non-newtonian fluid mechanics*, vol. 139, no. 1-2, pp. 21–30, 2006.

[48] W. W. Graessley, *Polymeric liquids and networks.* Garland Science, 2003.

[49] C. D. Han, *Rheology and processing of polymeric materials: Volume 1: Polymer Rheology.* Oxford University Press on Demand, 2007, vol. 1.

[50] P. K. Kundu, I. M. Cohen, and D. R. Dowling, *Fluid mechanics.* Elsevier Science, 2010.

[51] G. M. Whitesides, "The origins and the future of microfluidics", *Nature*, vol. 442, no. 7101, pp. 368–373, 2006.

[52] T. M. Squires and S. R. Quake, "Microfluidics: Fluid physics at the nanoliter scale", *Reviews of Modern Physics*, vol. 77, no. 3, pp. 977–1026, 2005.

[53] P. Tabeling, *Introduction to microfluidics.* Oxford University Press, 2005.

[54] C. Neto, V. Craig, and D. Williams, "Evidence of shear-dependent boundary slip in newtonian liquids", *The European Physical Journal E*, vol. 12, no. S1, pp. 71–74, 2003.

[55] G. K. Batchelor, *An introduction to fluid dynamics.* Cambridge university press, 2000.

[56] C. Neto, D. R. Evans, E. Bonaccurso, H. J. Butt, and V. S. Craig, "Boundary slip in Newtonian liquids: A review of experimental studies", *Reports on Progress in Physics*, vol. 68, no. 12, pp. 2859–2897, 2005.

[57] R. I. Tanner, *Engineering rheology.* OUP Oxford, 2000, vol. 52.

[58] N. Churaev, V. Sobolev, and A. Somov, "Slippage of liquids over lyophobic solid surfaces", *Journal of Colloid and Interface Science*, vol. 97, no. 2, pp. 574–581, 1984.

[59] V. S. J. Craig, C. Neto, and D. R. M. Williams, "Shear-Dependent Boundary Slip in an Aqueous Newtonian Liquid", *Physical Review Letters*, vol. 87, no. 5, p. 054504, 2001.

[60] R. Pit, H. Hervet, and L. Léger, "Direct Experimental Evidence of Slip in Hexadecane: Solid Interfaces", *Physical Review Letters*, vol. 85, no. 5, pp. 980–983, 2000.

[61] K. B. Migler, H. Hervet, and L. Leger, "Slip transition of a polymer melt under shear stress", *Physical Review Letters*, vol. 70, no. 3, pp. 287–290, 1993.

[62] O. I. Vinogradova, "Slippage of water over hydrophobic surfaces", *International Journal of Mineral Processing*, vol. 56, no. 1-4, pp. 31–60, 1999.

[63] S. Granick, Y. Zhu, and H. Lee, "Slippery questions about complex fluids flowing past solids", *Nature Materials*, vol. 2, no. 4, pp. 221–227, 2003.

[64] W. Schowalter, "The behavior of complex fluids at solid boundaries", *Journal of Non-Newtonian Fluid Mechanics*, vol. 29, pp. 25–36, 1988.

[65] H. Hervet and L. Léger, "Flow with slip at the wall: from simple to complex fluids Écoulements avec glissement à la paroi: des fluides simples aux fluides complexes", *Advances in Polymer Science*, vol. 4, pp. 241–249, 2003.

[66] T. Schmatko, H. Hervet, and L. Leger, "Friction and Slip at Simple Fluid-Solid Interfaces: The Roles of the Molecular Shape and the Solid-Liquid Interaction", *Physical Review Letters*, vol. 94, no. 24, p. 244501, 2005.

[67] C. Tropea, A. L. Yarin, and J. F. Foss, *Springer handbook of experimental fluid mechanics*. Springer Science+Business Media, 2007.

[68] D. C. Tretheway and C. D. Meinhart, "A generating mechanism for apparent fluid slip in hydrophobic microchannels", *Physics of Fluids*, vol. 16, no. 5, pp. 1509–1515, 2004.

[69] J. Franco, C. Gallegos, and H. Barnes, "On slip effects in steady-state flow measurements of oil-in-water food emulsions", *Journal of Food Engineering*, vol. 36, no. 1, pp. 89–102, 1998.

[70] M. Sánchez, C. Valencia, J. Franco, and C. Gallegos, "Wall Slip Phenomena in Oil-in-Water Emulsions: Effect of Some Structural Parameters", *Journal of Colloid and Interface Science*, vol. 241, no. 1, pp. 226–232, 2001.

[71] J. W. G. Tyrrell and P. Attard, "Images of Nanobubbles on Hydrophobic Surfaces and Their Interactions", *Physical Review Letters*, vol. 87, no. 17, p. 176104, 2001.

[72] S. Luk, R. Mutharasan, and D. Apelian, "Experimental observations of wall slip: tube and packed bed flow", *Industrial & engineering chemistry research*, vol. 26, no. 8, pp. 1609–1616, 1987.

[73] D. C. Tretheway and C. D. Meinhart, "Effects of Absolute Pressure on Fluid Slip in a Hydrophobic Microchannel", in *Fluids Engineering*, vol. 2003. ASME, 2003, pp. 561–564.

[74] W. B. Black and M. D. Graham, "Wall-Slip and Polymer-Melt Flow Instability", *Physical Review Letters*, vol. 77, no. 5, pp. 956–959, 1996.

[75] Y. Cohen and A. B. Metzner, "Apparent Slip Flow of Polymer Solutions", *Journal of Rheology*, vol. 29, no. 1, pp. 67–102, 1985.

[76] P. G. de Gennes, "Wetting: statics and dynamics", *Reviews of Modern Physics*, vol. 57, no. 3, pp. 827–863, 1985.

[77] P. Ballesta, R. Besseling, L. Isa, G. Petekidis, and W. C. K. Poon, "Slip and Flow of Hard-Sphere Colloidal Glasses", *Physical Review Letters*, vol. 101, no. 25, p. 258301, 2008.

[78] S. G. Hatzikiriakos and J. M. Dealy, "Wall slip of molten high density polyethylene. I. Sliding plate rheometer studies", *Journal of Rheology*, vol. 35, no. 4, pp. 497–523, 1991.

[79] W. Kozicki, C. Hsu, and C. Tiu, "Non-Newtonian flow through packed beds and porous media", *Chemical Engineering Science*, vol. 22, no. 4, pp. 487–502, 1967.

[80] H. A. Barnes, "A review of the slip (wall depletion) of polymer solutions, emulsions and particle suspensions in viscometers: its cause, character, and cure", *Journal of Non-Newtonian Fluid Mechanics*, vol. 56, no. 3, pp. 221–251, 1995.

[81] L. Chen, Y. Duan, C. Zhao, and L. Yang, "Rheological behavior and wall slip of concentrated coal water slurry in pipe flows", *Chemical Engineering and Processing: Process Intensification*, vol. 48, no. 7, pp. 1241–1248, 2009.

[82] D. M. Kalyon, P. Yaras, B. Aral, and U. Yilmazer, "Rheological behavior of a concentrated suspension: A solid rocket fuel simulant", *Journal of Rheology*, vol. 37, no. 1, pp. 35–53, 1993.

[83] A. Lindner, P. Coussot, and D. Bonn, "Viscous Fingering in a Yield Stress Fluid", *Physical Review Letters*, vol. 85, no. 2, pp. 314–317, 2000.

[84] H. Princen, "Rheology of foams and highly concentrated emulsions. II. experimental study of the yield stress and wall effects for concentrated oil-in-water emulsions", *Journal of Colloid and Interface Science*, vol. 105, no. 1, pp. 150–171, 1985.

[85] L. Bécu, P. Grondin, A. Colin, and S. Manneville, "How does a concentrated emulsion flow?: Yielding, local rheology, and wall slip", *Colloids and Surfaces A: Physicochemical and Engineering Aspects*, vol. 263, no. 1-3, pp. 146–152, 2005.

[86] S. P. Meeker, R. T. Bonnecaze, and M. Cloitre, "Slip and Flow in Soft Particle Pastes", *Physical Review Letters*, vol. 92, no. 19, p. 198302, 2004.

[87] S. P. Meeker, R. T. Bonnecaze, and M. Cloitre, "Slip and flow in pastes of soft particles: Direct observation and rheology", *Journal of Rheology*, vol. 48, no. 6, pp. 1295–1320, 2004.

[88] T. Young, "An Essay on the Cohesion of Fluids", *Philosophical Transactions of the Royal Society of London*, vol. 95, no. 0, pp. 65–87, 1805.

[89] S. Varagnolo, D. Ferraro, P. Fantinel, M. Pierno, G. Mistura, G. Amati, L. Biferale, and M. Sbragaglia, "Stick-Slip Sliding of Water Drops on Chemically Heterogeneous Surfaces", *Physical Review Letters*, vol. 111, no. 6, p. 066101, 2013.

[90] C. Semprebon, S. Varagnolo, D. Filippi, L. Perlini, M. Pierno, M. Brinkmann, and G. Mistura, "Deviation of sliding drops at a chemical step", *Soft Matter*, 2016.

[91] P. G. de Gennes, F. Brochard Wyart, and D. Quéré, "Capillarity and Gravity", in *Capillarity and Wetting Phenomena*. New York, NY: Springer New York, 2004, pp. 33–67.

[92] R. N. Wenzel, "Resistance of solid surfaces to wetting by water", *Industrial & Engineering Chemistry*, vol. 28, no. 8, pp. 988–994, 1936.

[93] A. B. D. Cassie and S. Baxter, "Wettability of porous surfaces", *Transactions of the Faraday Society*, vol. 40, no. 0, p. 546, 1944.

[94] D. Quéré, "Surface chemistry: Fakir droplets", *Nature Materials*, vol. 1, no. 1, pp. 14–15, 2002.

[95] A. J. Liu and S. R. Nagel, "Jamming is not just cool any more", *Nature*, vol. 396, no. 6706, pp. 21–22, 1998.

[96] M. J. Rosen and J. T. Kunjappu, *Surfactants and interfacial phenomena*. Wiley, 2012.

[97] W. D. Bancroft, "The Theory of Emulsification, V", *The Journal of Physical Chemistry*, vol. 17, no. 6, pp. 501–519, 1912.

[98] P. K. Kilpatrick, "Water-in-Crude Oil Emulsion Stabilization: Review and Unanswered Questions", *Energy & Fuels*, vol. 26, no. 7, pp. 4017–4026, 2012.

[99] S. L. Kokal, "Crude Oil Emulsions: A State-Of-The-Art Review", *SPE Production & Facilities*, vol. 20, no. 01, pp. 5–13, 2005.

[100] H. A. Barnes, "Rheology of emulsions — a review", *Colloids and Surfaces A: Physicochemical and Engineering Aspects*, vol. 91, pp. 89–95, 1994.

[101] J. Sjoblom, *Emulsions and emulsion stability: Surfactant science series/61*. CRC Press, 2005.

[102] H. Karbstein and H. Schubert, "Developments in the continuous mechanical production of oil-in-water macro-emulsions", *Chemical Engineering and Processing: Process Intensification*, vol. 34, no. 3, pp. 205–211, 1995.

[103] J. Floury, A. Desrumaux, and J. Lardières, "Effect of high-pressure homogenization on droplet size distributions and rheological properties of model oil-in-water emulsions", *Innovative Food Science & Emerging Technologies*, vol. 1, no. 2, pp. 127–134, 2000.

[104] H. S. Ribeiro, J. J. M. Janssen, I. Kobayashi, and M. Nakajima, "Membrane Emulsification for Food Applications", in *Membrane Technology*. Weinheim, Germany: Wiley-VCH Verlag GmbH & Co. KGaA, 2010, pp. 129–166.

[105] I. Kobayashi, Y. Wada, K. Uemura, and M. Nakajima, "Microchannel emulsification for mass production of uniform fine droplets: integration of microchannel arrays on a chip", *Microfluidics and Nanofluidics*, vol. 8, no. 2, pp. 255–262, 2010.

[106] T. Thorsen, R. W. Roberts, F. H. Arnold, and S. R. Quake, "Dynamic Pattern Formation in a Vesicle-Generating Microfluidic Device", *Physical Review Letters*, vol. 86, no. 18, pp. 4163–4166, 2001.

[107] A. Ofner, D. G. Moore, P. A. Rühs, P. Schwendimann, M. Eggersdorfer, E. Amstad, D. A. Weitz, and A. R. Studart, "High-Throughput Step Emulsification for the Production of Functional Materials Using a Glass Microfluidic Device", *Macromolecular Chemistry and Physics*, vol. 218, no. 2, p. 1600472, 2017.

[108] N. Khalid, I. Kobayashi, M. A. Neves, K. Uemura, and M. Nakajima, "Microchannel emulsification: A promising technique towards encapsulation of functional compounds", *Critical Reviews in Food Science and Nutrition*, pp. 1–22, 2017.

[109] H. Princen, "Rheology of foams and highly concentrated emulsions: I. Elastic properties and yield stress of a cylindrical model system", *Journal of Colloid and Interface Science*, vol. 91, no. 1, pp. 160–175, 1983.

[110] P. Hébraud, F. Lequeux, J. P. Munch, and D. J. Pine, "Yielding and Rearrangements in Disordered Emulsions", *Physical Review Letters*, vol. 78, no. 24, pp. 4657–4660, 1997.

[111] T. Mason, J. Bibette, and D. Weitz, "Yielding and Flow of Monodisperse Emulsions", *Journal of Colloid and Interface Science*, vol. 179, no. 2, pp. 439–448, 1996.

[112] P. Schall, I. Cohen, D. A. Weitz, and F. Spaepen, "Visualization of Dislocation Dynamics in Colloidal Crystals", *Science*, vol. 305, no. 5692, pp. 1944–1948, 2004.

[113] L. Bécu, S. Manneville, and A. Colin, "Yielding and Flow in Adhesive and Nonadhesive Concentrated Emulsions", *Physical Review Letters*, vol. 96, no. 13, p. 138302, 2006.

[114] A. Ragouilliaux, G. Ovarlez, N. Shahidzadeh-Bonn, B. Herzhaft, T. Palermo, and P. Coussot, "Transition from a simple yield-stress fluid to a thixotropic material", *Physical Review E*, vol. 76, no. 5, p. 051408, 2007.

[115] R. Besseling, L. Isa, P. Ballesta, G. Petekidis, M. E. Cates, and W. C. K. Poon, "Shear Banding and Flow-Concentration Coupling in Colloidal Glasses", *Physical Review Letters*, vol. 105, no. 26, p. 268301, 2010.

[116] P. Coussot, J. S. Raynaud, F. Bertrand, P. Moucheront, J. P. Guilbaud, H. T. Huynh, S. Jarny, and D. Lesueur, "Coexistence of Liquid and Solid Phases in Flowing Soft-Glassy Materials", *Physical Review Letters*, vol. 88, no. 21, p. 218301, 2002.

[117] J.-B. Salmon, A. Colin, S. Manneville, and F. Molino, "Velocity Profiles in Shear-Banding Wormlike Micelles", *Physical Review Letters*, vol. 90, no. 22, p. 228303, 2003.

[118] S. A. Rogers, D. Vlassopoulos, and P. T. Callaghan, "Aging, Yielding, and Shear Banding in Soft Colloidal Glasses", *Physical Review Letters*, vol. 100, no. 12, p. 128304, 2008.

[119] B. M. Erwin, D. Vlassopoulos, and M. Cloitre, "Rheological fingerprinting of an aging soft colloidal glass", *Journal of Rheology*, vol. 54, no. 4, pp. 915–939, 2010.

[120] G. Katgert, B. P. Tighe, M. E. Möbius, and M. van Hecke, "Couette flow of two-dimensional foams", *EPL (Europhysics Letters)*, vol. 90, no. 5, p. 54002, 2010.

[121] B. Geraud, L. Bocquet, and C. Barentin, "Confined flows of a polymer microgel", *Eur. Phys. J. E Soft Matter*, vol. 36, no. 3, p. 30, 2013.

[122] M. Sbragaglia, R. Benzi, M. Bernaschi, and S. Succi, "The emergence of supramolecular forces from lattice kinetic models of non-ideal fluids: applications to the rheology of soft glassy materials", *Soft Matter*, vol. 8, no. 41, pp. 10 773–10 782, 2012.

[123] L. Bocquet, A. Colin, and A. Ajdari, "Kinetic Theory of Plastic Flow in Soft Glassy Materials", *Phys. Rev. Lett.*, vol. 103, no. 3, p. 36001, 2009.

[124] A. Nicolas and J.-L. Barrat, "A mesoscopic model for the rheology of soft amorphous solids, with application to microchannel flows", *Faraday Discuss.*, vol. 167, no. 0, pp. 567–600, 2013.

[125] M. Bouzid, A. Izzet, M. Trulsson, E. Clément, P. Claudin, and B. Andreotti, "Non-local rheology in dense granular flows", *Eur. Phys. J. E Soft Matter*, vol. 38, no. 11, pp. 1–15, 2015.

[126] V. Mansard, A. Colin, P. Chaudhuri, and L. Bocquet, "A molecular dynamics study of non-local effects in the flow of soft jammed particles", *Soft Matter*, vol. 9, no. 31, pp. 7489–7500, 2013.

[127] R. Benzi, M. Bernaschi, M. Sbragaglia, and S. Succi, "Herschel-Bulkley rheology from lattice kinetic theory of soft glassy materials", *EPL (Europhysics Letters)*, vol. 91, no. 1, p. 14003, 2010.

[128] J. R. Seth, C. Locatelli-Champagne, F. Monti, R. T. Bonnecaze, and M. Cloitre, "How do soft particle glasses yield and flow near solid surfaces?" *Soft Matter*, vol. 8, no. 1, pp. 140–148, 2012.

[129] C. Monthus and J.-P. Bouchaud, "Models of traps and glass phenomenology", *Journal of Physics A: Mathematical and General*, vol. 29, no. 14, pp. 3847–3869, 1996.

[130] P. Sollich, F. Lequeux, P. Hébraud, and M. E. Cates, "Rheology of soft glassy materials", *Physical Review Letters*, vol. 78, no. 10, pp. 2020–2023, 1997.

[131] P. Sollich, "Rheological constitutive equation for a model of soft glassy materials", *Phys. Rev. E*, vol. 58, no. 1, pp. 738–759, 1998.

[132] E. R. Weeks, J. C. Crocker, A. C. Levitt, A. Schofield, D. A. Weitz, P. N. Pusey, A. B. Schofield, M. E. Cates, M. Fuchs, and W. C. K. Poon, "Three-Dimensional Direct Imaging of Structural Relaxation Near the Colloidal Glass Transition", *Science*, vol. 287, no. 5453, pp. 627–631, 2000.

[133] L. Derzsi, D. Filippi, G. Mistura, M. Pierno, M. Lulli, M. Sbragaglia, M. Bernaschi, and P. Garstecki, "Fluidization and wall slip of soft-glassy materials by controlled surface roughness", *Physical Review E*, 2016.

[134] M. J. Madou, *Fundamentals of microfabrication and nanotechnology.* CRC Press, 2012.

[135] N. P. Mahalik, *Micromanufacturing and Nanotechnology.* Berlin/Heidelberg: Springer-Verlag, 2006.

[136] C. W. Tsao and D. L. DeVoe, "Bonding of thermoplastic polymer microfluidics", *Microfluidics and Nanofluidics*, vol. 6, no. 1, pp. 1–16, 2009.

[137] M. Vaezi, H. Seitz, and S. Yang, "A review on 3D micro-additive manufacturing technologies", *The International Journal of Advanced Manufacturing Technology*, vol. 67, no. 5-8, pp. 1721–1754, 2013.

[138] Y. Xia and G. M. Whitesides, "Soft lithography", *Angewandte Chemie International Edition*, vol. 37, no. 5, pp. 550–575, 1998.

[139] L. Alting, F. Kimura, H. N. Hansen, and G. Bissacco, "Micro engineering", *CIRP Annals-Manufacturing Technology*, vol. 52, no. 2, pp. 635–657, 2003.

[140] G. L. Benavides, D. P. Adams, and P. Yang, "Meso-machining capabilities", *Sandia National Laboratories, Albuquerque, New Mexico*, vol. 87185, 2001.

[141] J. M. Bustillo, R. T. Howe, and R. S. Muller, "Surface micromachining for microelectromechanical systems", *Proceedings of the IEEE*, vol. 86, no. 8, pp. 1552–1574, 1998.

[142] A. Kummrow, J. Theisen, M. Frankowski, A. Tuchscheerer, H. Yildirim, K. Brattke, M. Schmidt, and J. Neukammer, "Microfluidic structures for flow cytometric analysis of hydrodynamically focussed blood cells fabricated by ultraprecision micromachining", *Lab on a Chip*, vol. 9, no. 7, pp. 972–981, 2009.

[143] M. E. Wilson, N. Kota, Y. Kim, Y. Wang, D. B. Stolz, P. R. LeDuc, and O. B. Ozdoganlar, "Fabrication of circular microfluidic channels by combining mechanical micromilling and soft lithography", *Lab on a Chip*, vol. 11, no. 8, pp. 1550–1555, 2011.

[144] X. Liu, R. E. DeVor, S. G. Kapoor, and K. F. Ehmann, "The mechanics of machining at the microscale: assessment of the current state of the science", *Journal of manufacturing science and engineering*, vol. 126, no. 4, pp. 666–678, 2004.

[145] C. Mack, *Fundamental Principles of Optical Lithography.* John Wiley \& Sons, 2007.

[146] A. G. Emslie, F. T. Bonner, and L. G. Peck, "Flow of a viscous liquid on a rotating disk", *Journal of Applied Physics*, vol. 29, no. 5, pp. 858–862, 1958.

[147] A. Mata, A. J. Fleischman, and S. Roy, "Fabrication of multi-layer SU-8 microstructures", *Journal of Micromechanics and Microengineering*, vol. 16, no. 2, pp. 276–284, 2006.

[148] S. Choi and J.-K. Park, "Two-step photolithography to fabricate multilevel microchannels", *Biomicrofluidics*, vol. 4, no. 4, p. 046503, 2010.

[149] M. Christophersen and B. F. Phlips, "Gray-tone lithography using an optical diffuser and a contact aligner", *Applied Physics Letters*, vol. 92, no. 19, pp. 1–4, 2008.

[150] M. A. Unger, H. P. Chou, T. Thorsen, A. Scherer, and S. R. Quake, "Monolithic microfabricated valves and pumps by multilayer soft lithography", *Science*, vol. 288, no. 5463, pp. 113–116, 2000.

[151] R. Martinez-Duarte and M. Madou, "SU-8 Photolithography and Its Impact on Microfluidics", *Microfluidics and Nanofluidics Handbook*, no. 2006, pp. 231–268, 2011.

[152] S. R. Quake and A. Scherer, "From micro- to nanofabrication with soft materials." *Science (New York, N.Y.)*, vol. 290, no. 5496, pp. 1536–40, 2000.

[153] M. Klanjšek Gunde, N. Hauptman, M. MačEk, and M. Kunaver, "The influence of hard-baking temperature applied for SU8 sensor layer on the sensitivity of capacitive chemical sensor", *Applied Physics A: Materials Science and Processing*, vol. 95, no. 3, pp. 673–680, 2009.

[154] S. Keller, G. Blagoi, M. Lillemose, D. Haefliger, and A. Boisen, "Processing of thin SU-8 films", *Journal of Micromechanics and Microengineering*, vol. 18, no. 12, 2008.

[155] C. H. Lin, G. B. Lee, B. W. Chang, and G. L. Chang, "A new fabrication process for ultra-thick microfluidic microstructures utilizing SU-8 photoresist", *Journal of Micromechanics and Microengineering*, vol. 12, no. 5, pp. 590–597, 2002.

[156] P. R. Kanikella, S. Mine, and P. R. Kanikella, "Process development and applications of a dry film photoresist", Ph.D. dissertation, Uiversity of Missouri-Rolla, 2007.

[157] H. Lorenz, L. Paratte, R. Luthier, N. F. de Rooij, and P. Renaud, "Low-cost technology for multilayer electroplated parts using laminated dry film resist", *Sensors and Actuators A: Physical*, vol. 53, no. 1-3, pp. 364–368, 1996.

[158] I. Chartier, J. Sudor, Y. Fouillet, N. Sarrut, C. Bory, and A. Gruss, "Fabrication of a hybrid plastic-silicon microfluidic device for high-throughput genotyping", in *Microfluidics, BioMEMS, and Medical Microsystems*, H. Becker and P. Woias, Eds., vol. 4982. International Society for Optics and Photonics, 2003, p. 208.

[159] S. Schlautmann, H. Wensink, R. Schasfoort, M. Elwenspoek, and A. van den Berg, "Powder-blasting technology as an alternative tool for microfabrication of capillary electrophoresis chips with integrated conductivity sensors", *Journal of Micromechanics and Microengineering*, vol. 11, no. 4, pp. 386–389, 2001.

[160] P. Vulto, N. Glade, L. Altomare, J. Bablet, L. D. Tin, G. Medoro, I. Chartier, N. Manaresi, M. Tartagni, and R. Guerrieri, "Microfluidic channel fabrication in dry film resist for production and prototyping of hybrid chips", *Lab on a Chip*, vol. 5, no. 2, p. 158, 2005.

[161] "ISO 14644-1:2015 - Cleanrooms and associated controlled environments – Part 1: Classification of air cleanliness by particle concentration."

[162] R. J. Adrian, "Particle-imaging techniques for experimental fluid mechanics", *Annu. Rev. Fluid Mech.*, vol. 23, no. 1, pp. 261–304, 1991.

[163] D. Sinton, "Microscale flow visualization", *Microfluidics and Nanofluidics*, vol. 1, no. 1, pp. 2–21, 2004.

[164] J.-T. Lin and Y.-H. Pao, "Wakes in stratified fluids", *Annual Review of Fluid Mechanics*, vol. 11, no. 1, pp. 317–338, 1979.

[165] H. Richard and M. Raffel, "Principle and applications of the background oriented schlieren (BOS) method", *Measurement Science and Technology*, vol. 12, no. 9, pp. 1576–1585, 2001.

[166] W. Merzkirch, "Generalized Analysis of Shearing Interferometers as Applied for Gas Dynamic Studies", *Appl. Opt.*, vol. 13, no. 2, pp. 409–413, 1974.

[167] W. Merzkirch, *Fluid Mechanics of Flow Metering.* Springer, 2005.

[168] W. Merzkirch, *Techniques of Flow Visualization.* AGARD, 2013, vol. 53.

[169] J. Stasiek, "Thermochromic liquid crystals and true colour image processing in heat transfer and fluid-flow research", *Heat and Mass Transfer*, vol. 33, no. 1, pp. 27–39, 1997.

[170] F. Durst, A. Melling, and J. Whitelaw, "Principles and practice of laser-Doppler anemometry", *NASA STI/Recon Technical Report A*, vol. 76, 1976.

[171] T. Dracos, "Particle Tracking Velocimetry", in *Three-Dimensional Velocity and Vorticity Measuring and Image Analysis Techniques.* Springer Netherlands, 1996, pp. 155–160.

[172] S. Fu, P.-h. Biwolé, and C. Mathis, "A Comparative Study of Particle Image Velocimetry (PIV) and Particle Tracking Velocimetry (PTV) for Airflow Measurement", *International Journal of Mechanical and Mechatronics Engineering A*, vol. 9, no. 1, pp. 40–45, 2015.

[173] J. G. Santiago, S. T. Wereley, C. D. Meinhart, D. J. Beebe, and R. J. Adrian, "A particle image velocimetry system for microfluidics", *Experiments in Fluids*, vol. 25, no. 4, pp. 316–319, 1998.

[174] S. Inoué and K. R. Spring, *Video microscopy : the fundamentals.* Plenum Press, 1997.

[175] K. Ito, "Gaussian filter for nonlinear filtering problems", in *Proceedings of the 39th IEEE Conference on Decision and Control (Cat. No.00CH37187)*, vol. 2. IEEE, 2000, pp. 1218–1223.

[176] J.-Y. Y. Tinevez, N. Perry, J. Schindelin, G. M. Hoopes, G. D. Reynolds, E. Laplantine, S. Y. Bednarek, S. L. Shorte, and K. W. Eliceiri, "TrackMate: An open and extensible platform for single-particle tracking", *Methods*, vol. 115, pp. 80–90, 2016.

[177] R. G. Brown and P. Y. C. Hwang, *Introduction to random signals and applied Kalman filtering: with MATLAB exercises.* John Wiley, 2012.

[178] Y. Liu and P. H. Daum, "Relationship of refractive index to mass density and self-consistency of mixing rules for multicomponent mixtures like ambient aerosols", *Journal of Aerosol Science*, vol. 39, no. 11, pp. 974–986, 2008.

[179] J. Schindelin, I. Arganda-Carreras, E. Frise, V. Kaynig, M. Longair, T. Pietzsch, S. Preibisch, C. Rueden, S. Saalfeld, B. Schmid, and Others, "Fiji: an open-source platform for biological-image analysis", *Nat. Methods*, vol. 9, no. 7, pp. 676–682, 2012.

[180] K. N. Nordstrom, E. Verneuil, P. E. Arratia, A. Basu, Z. Zhang, A. G. Yodh, J. P. Gollub, and D. J. Durian, "Microfluidic Rheology of Soft Colloids above and below Jamming", *Physical Review Letters*, vol. 105, no. 17, p. 175701, 2010.

[181] S. Succi, *The lattice Boltzmann equation for Fluid Dynamics and Beyond.* Oxford University Press, 2001.

[182] L. Derzsi, D. Filippi, G. Mistura, M. Pierno, M. Lulli, M. Sbragaglia, M. Bernaschi, and P. Garstecki, "Fluidization and wall slip of soft glassy materials by controlled surface roughness", *Physical Review E*, vol. 95, no. 5, p. 52602, 2017.

[183] M. Bernaschi, M. Lulli, and M. Sbragaglia, "GPU Based Detection of Topological Changes in Voronoi Diagrams", *ArXiv e-prints*, 2016.

[184] B. Delaunay, "Sur la sphère vide. A la mémoire de Georges Voronoi", *Bulletin de l'Academie des Sciences de l'URSS,Classe des sciences mathematiques et naturelles*, vol. 6, pp. 443–514, 1934.

[185] B. Dollet, A. Scagliarini, and M. Sbragaglia, "Two-dimensional plastic flow of foams and emulsions in a channel: experiments and lattice Boltzmann simulations", *J. Fluid Mech.*, vol. 766, pp. 556–589, 2015.

[186] A. Scagliarini, M. Sbragaglia, and M. Bernaschi, "Mesoscopic Simulation Study of Wall Roughness Effects in Micro-channel Flows of Dense Emulsions", *J. Stat. Phys.*, vol. 161, no. 6, pp. 1482–1495, 2015.

[187] J. Davies, D. Maynes, B. W. Webb, and B. Woolford, "Laminar flow in a microchannel with superhydrophobic walls exhibiting transverse ribs", *Physics of Fluids*, vol. 18, no. 8, 2006.

[188] T. Sochi, "Slip at fluid-solid interface", *Polymer Reviews*, vol. 51, no. 4, pp. 309–340, 2011.

[189] O. I. Vinogradova and A. V. Belyaev, "Wetting, roughness and flow boundary conditions", *Journal of Physics Condensed Matter*, vol. 23, no. 18, 2011.

[190] M. H. Farias, C. S. Castro, D. A. Garcia, and J. S. Henrique, "Surface roughness influences on the behaviour of flow inside microchannels", *Journal of Physics: Conference Series*, vol. 975, no. 1, p. 12078, 2018.